Deformation Mechanics and Microstructure Evolution of Material Removal at Small Length-Scale

by

Shan Gong

B.Eng. in Welding Science and Technology, Harbin Institute of Technology, 2011

M.Eng. in Material Processing Technology, Harbin Institute of Technology, 2013

Submitted to the Graduate Faculty of
Swanson School of Engineering in partial fulfillment
of the requirements for the degree of

Doctor of Philosophy

University of Pittsburgh
2020

UNIVERSITY OF PITTSBURGH

SWANSON SCHOOL OF ENGINEERING

This dissertation was presented

by

Shan Gong

It was defended on

December 6, 2019

and approved by

M. Ravi Shankar, Ph.D., Professor, Department of Industrial Engineering

Bopaya Bidanda, Ph.D., Ernest E. Roth Professor, Department of Industrial Engineering

Youngjae Chun, Ph.D., Associate Professor, Department of Industrial Engineering

Jörg M.K. Wiezorek, Ph.D., Professor, Department of Mechanical Engineering and Material Science

Dissertation Director: M. Ravi Shankar, Ph.D., Professor, Department of Industrial Engineering

Deformation Mechanics and Microstructure Evolution of Material Removal at Small Length-Scale

Shan Gong, PhD

University of Pittsburgh, 2020

Deformation mechanics and microstructure evolution of material removal at the micrometer length-scale were studied via performing plane strain machining inside a scanning electron microscope. In Cu, deformation mechanics was characterized by performing digital image correlation on secondary electron images of deformation zone. Corresponding microstructure evolutions were examined by orientation imaging microscopy using electron backscattered diffraction. While the deformation geometry and rate are identical, resultant microstructure in deformed chips spans the entire gamut from conventional ultrafine-grained structure to complete lack of refinement among different crystal orientations due to variation in dislocation evolution, i.e. orientation-dependent deformation anisotropy. Subsequent examination of machining surface revealed topographical defects along some grain boundaries. It is hypothesized that rampant ductile fracture occurs due to elevated dislocation densities in the vicinity of grain boundary, which is imprinted on the freshly generated surface as revealed by *in situ* experiments. This phenomenon essentially limits the precision of diamond turning-based processes in nanometrically-smooth roughness profiles.

In Mg AZ31, we demonstrated that refining one characteristic dimension of the deformation geometry to the 100nm-scale triggers a brittle-to-ductile transition at ambient temperatures. The other two dimensions can be substantially larger or even macroscopic. The ability to accommodate shear strains greater than 200% in this configuration is independent of the orientation of the crystals with respect to the loading direction. Refining the characteristic dimension enables accommodation of large plastic strains via multi-slip by reducing the mismatch in critical resolved shear stress of available slip systems, while engendering the characteristically dramatic microstructure refinement. In pure magnesium, the deformed chip features much larger grain sizes compared with AZ31 due to rampant dynamic recrystallization in the absence of solute dragging effect. These observations imply that achieving the combination of low-density, high strength and formability in bulk Mg (alloys) can be accomplished by designing microstructure and composites in fewer than 3 dimensions without requiring precise control over crystal orientations.

Keywords: Severe plastic deformation, Size effect, Deformation microstructure, Anisotropy, Electron microscopy.

Table of Contents

List of Tables

List of Figures

Preface

I would like to take this opportunity to express my deep appreciation to my advisor, Prof. M. Ravi Shankar, for his guidance and support through my whole study here at Pitt. His passion for research, creative thinking and focus on details have taught me so much and helped me to develop my own philosophy on research. His patience and encouragement walked me through the challenging journey of PhD study. I am also grateful to Prof. Jörg M.K. Wiezorek for advising on many challenges with great knowledge and inspiration, especially in transmission electron microscopy. I also deeply appreciate Prof. Bopaya Bidanda and Prof. Youngjae Chun for their warm support and critical insights in my dissertation.

I am grateful for the generous support from II-VI Foundation through Block Gift Program. I would also wish to thank Richard H. Hopkins and John Spitznagel for discussions and encouragement during my PhD study.

I want thank my lab mates, student colleagues, and all the friends I made and people I met who helped me during my study at Pitt, and made my stay at Pitt a unique experience and precious memory in my life.

Finally, My special thanks go to my family for their endless support and encouragement through my entire life and study. They are always my strongest confidence.

1.0 Introduction

The enormous demands for fabricating components with either miniaturized complex geometries or precise control of critical dimensions have catalyzed the increasing applications of micro-scale plastic deformation. Over the last two decades, there have been vast majority of experimental and computational studies on uniaxial deformation on micron and sub-micron crystals, which unambiguously show that the mechanical properties including yield strength, ultimate tensile strength, ductility, etc. highly depend on external sample size. Unfortunately, these studies have mainly focused on the exploration in the small strain regimes. Although these findings have significantly improved our understandings regarding to fundamental deformation mechanisms including dislocation dynamics, interactions with interfaces (like grain boundary, sample surface, etc.) and also promoted efforts in corresponding simulation works, there is still a gap towards to real manufacturing practice which routinely involves severe plastic deformation. Furthermore, the prevalent application of polycrystalline materials presents another level of complexity. On one hand, the variation in crystal orientations can potentially lead to different plastic responses; on the other hand, the internal microstructural characteristics including the grain sizes, and grain boundaries will also alter the deformation locally. Since both intrinsic (microstructural) and extrinsic (sample/deformation size) dimensions have huge effects on material deformation, it is critical to develop an understanding of their effect on the plastic deformation.

The focus of this research is predominantly to delineate the mechanics of deformation and corresponding microstructure evolution during imposing severe plastic deformation at the micrometer length-scales by varying the extrinsic parameter (characteristic length-scale of deformation geometry) and its interaction with intrinsic parameter (bulk grain orientation and grain boundary characteristics). Here the deformation configuration utilized is plane strain machining with preset depth of cut set at the micrometer length-scale. Two metallic material systems were used in this experimental study: Oxygen Free High Conductivity (OFHC) Cu with face-cubic centered structure and pure magnesium and Mg AZ31 with hexagonal close packed structure.

Plain strain machining on Cu samples at the micrometer length-scale is performed *in situ* inside a scanning electron microscope. Deformation mechanics is characterized by performing Digital Image Correlation (DIC) on secondary electron images of deformation zone from different bulk grains. Corresponding microstructure evolutions are examined by orientation imaging microscopy using electron backscattered diffraction, which is overlaid with aforementioned deformation mechanics to characterize the orientation-dependent anisotropic response despite of identical machining conditions. It is shown that while the deformation geometry and rate are identical resultant microstructure in deformed chips spans the entire gamut from conventional ultra-fine grained structure to complete lack of refinement due to the anisotropy in dislocation accumulation. Subsequently, examination of machining surface reveals topographical defects along grain boundaries, which is attributed to the ductile tearing in the vicinity of grain boundaries due to deformation anisotropy.

The utility of magnesium alloys in engineering applications is limited by their poor formability and manufacturability. The response of the hexagonal crystal lattice in Mg to plastic deformation is highly anisotropic, which results in the localization of plastic strains and an inability to achieve homogeneous shape change. We demonstrate that refining one characteristic dimension of the deformation geometry to the 100nm-scale triggers a brittle-to-ductile transition in Mg at ambient temperatures. The other two dimensions can be substantially larger or even macroscopic. The ability of Mg to accommodate shear strains greater than 200% in this configuration is independent of the orientation of the crystals with respect to the loading direction. This implies that achieving the combination of low-density, high strength and formability in bulk Mg alloys can be accomplished by designing microstructures and composites in fewer than 3D without requiring precise control over the crystal structure or orientation.

The thesis is organized in five primary sections. The first section is literature review which aims to provide a brief introduction of plastic deformation in metals, including mechanical behavior and microstructure evolution. Additionally, the mechanics of machining based severe plastic deformation is also briefly reviewed. The second section presents a detailed description of the experimental equipments and developed techniques in the course of this research work. The third section discuses the orientation-dependent anisotropy during severe plastic deformation in plain strain machining of Cu at the micrometer length-scales. The fourth section discusses the size-related deformation behavior of Mg AZ31 and pure magnesium, i.e. brittle-to-ductile transition. The fifth section describes the main conclusions and some potential future directions from current research.

2.0 Literature Review

With accelerating trends towards miniaturization, micro-manufacturing processes become a critical requirement for various applications in industry. Despite of kinematical similarities with conventional macro-manufacturing, reducing the size of deformation can cause fundamental changes in deformation behavior. At the micrometer length-scales, characteristic dimensions of crystals in metals become comparable with the dimension of external deformation. Thus, micro-manufacturing normally involve individual crystals or a few ones at a given incremental time. Correspondingly, the anisotropy depending on crystal orientation can lead to anomalies in plastic response such as mechanical properties, microstructural attributes, etc. This chapter aims at briefly reviewing basics of plastic deformation in metals and the size-related deformation behaviors and then providing an introduction to machining mechanics.

2.1 Plastic Deformation in Metals

The onset of plastic flow takes place through the operation of dislocation sources and the movement of dislocations over large distances[45]. The mode of dislocation motion includes slip (a conservative motion with respect to the crystal volume) and climb (a non-conservative motion). Due to geometric properties, edge dislocations can move by slip and climb, while screw dislocations move via slip and cross-slip. Depending on the crystallographic structures, dislocation motions occur along close-packed atomic directions on planes with densest atomic packing for most scenarios. The combinations of slip planes and directions form the slip systems. As dislocations move through a lattice, they encounter lattice frictional stress, which was calculated by Peierls and Nabarro[47, 54] as

$$\tau_{\mathrm{f}} = G \exp\left[-\frac{2\pi a}{(1-\nu)\, b}\right] \tag{2.1}$$

where G is the shear modulus, a is the inter-planar width, b is the interatomic spacing and ν is the Poisson's ratio. Apparently, this lattice frictional stress τ_{f} depends on the slip systems. Interactions among dislocations in motion can alter their topology introducing jogs, which results in a reduction in dislocation velocity. Obstacles in motion path like immobile dislocations, grain boundaries, surfaces, can lead to generation of multiple dislocations, i.e. dislocation multiplication. A multiplication mechanism commonly seen, the Frank-Read source, is shown in Figure 1.

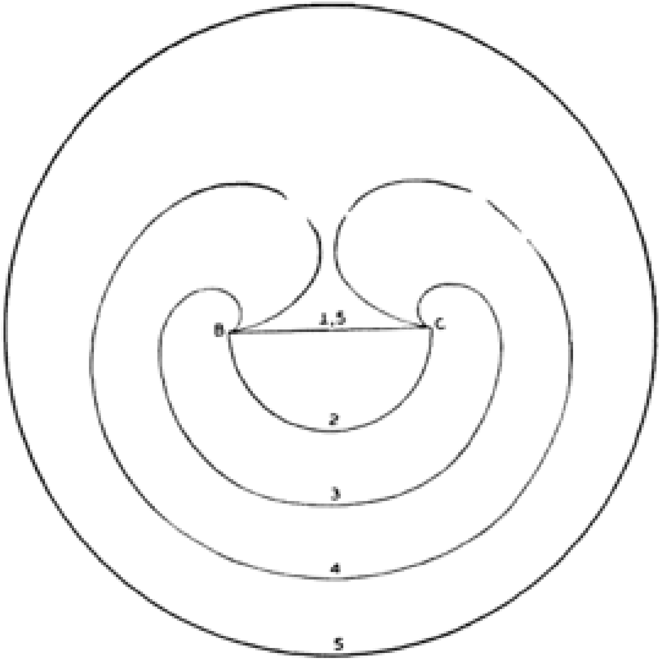

Figure 1: Frank–Read source: multiplication of moving dislocations[25].

The concentration of dislocations in the crystalline material is defined by the dislocation density $\rho = L_{\mathrm{dislocation}}/V_{\mathrm{material}}$, where $L_{\mathrm{dislocation}}$ is the total length of dislocation lines in the material, and V_{material} is the volume of the bulk material being considered. Upon progressive imposition of plastic deformation, dislocation densities are increased to accommodate the strain, for example, from $\sim 10^{13} - 10^{14}\mathrm{m}^{-2}$ in fully annealed metals to $\sim 10^{16}\mathrm{m}^{-2}$ in heavily deformed ones[48].

2.2 Stages of plastic deformation

Plastic deformation of crystalline metals is accommodated via dislocation multiplication, annihilation, rearrangement, and (possible) twinning[16, 48]. Motion of dislocations is confined to slip systems, of which mobility and glide are fundamentally determined by the lattice structure and in turn, determines the mechanical response. Figure 2 shows schematic stress-strain curve of a typical face-centered cubic single crystal oriented for single slip. This stress-strain curve can generally be divided into four stages based on characteristics of strain hardening rates. Stage I features a relatively low work-hardening rate after initial yielding, due to the so-called "easy-glide" which is associated with dislocation motions on single active slip systems. The activated slip system has the highest resolved shear stress on the corresponding slip plane (larger than its corresponding critical resolved shear stress τ_{CRSS}). The stress fields interaction from dislocation motions on parallel slip planes gives rise to the initial work-hardening, although negligible. The transition from Stage I to Stage II starts from the onset of multiple slips, which inevitably lead to strong dislocation interactions. Dislocation tangles are formed during progressive imposition of plastic strain resulting in an increase in flow stress. This region features a linear hardening rate, with a nearly constant coefficient ($\sim G/300$) independent of temperature and strain rate[17]. In Stage II, the behavior of different crystal orientations demonstrates largest difference. Stage III, characterized by a reduced work-hardening rate compared to that in Stage II, features the formation of dislocation cells, which refer to typically equiaxed volumes surrounded by tangled boundaries (dislocation walls), and is very sensitive to temperature and strain rate. In the work-hardening curve, Stage IV has a linear hardening rate (much smaller than that in Stage II). Furthermore, this hardening rate is linearly dependent on the flow stress. In this stage, excessive strain level considerably enlarges the surface and interface areas (e.g., grain boundaries).

In face-centered cubic metals, there are 12 independent slip systems available. A slip system is activated when the applied stress τ is larger than its corresponding critical resolved shear stress τ_{CRSS}. The resolved stress components on each slip system are determined by the alignment of crystal lattice with respect to external loading. As for plastic deformation

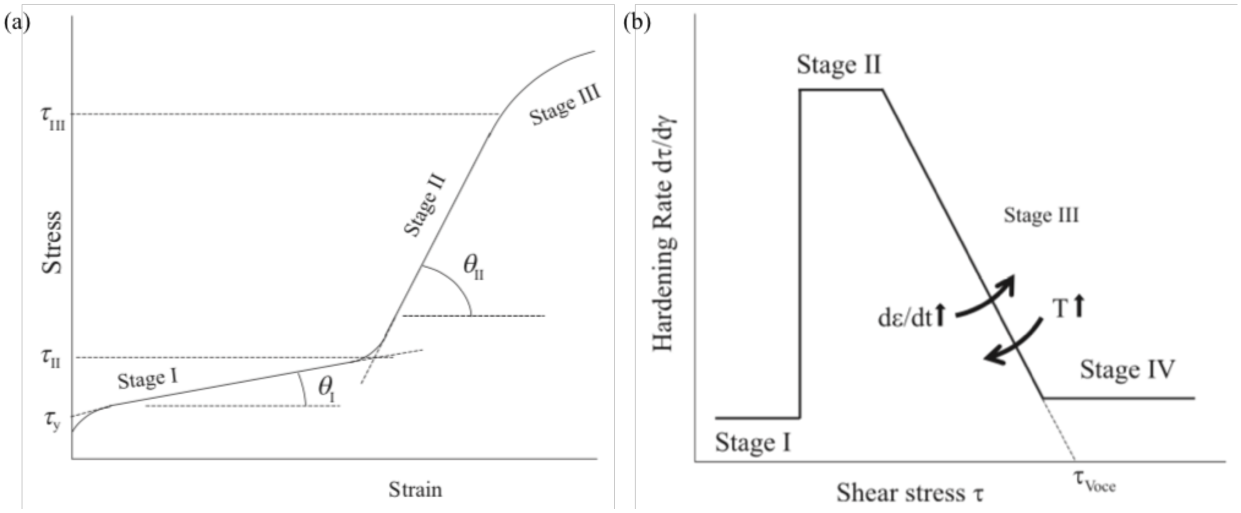

Figure 2: (a) Schematic stress-strain curves for fcc single crystal oriented for single slip in uniaxial tensile deformation, which shows stages of deformation. (b) Hardening rate versus flow stress showing all four stages of work hardening[59].

with low to moderate strain values (Stage I and II), only a limited number of slip systems are involved which can be well predicted by Schmid Factor analysis. The stress-strain curves of different crystal orientations with respect to same external loading shows characteristic divergence[20], i.e., anisotropy. As strain increases into severe plastic deformation (Stage III and IV) involving prolific cross-slip, plastic response does not necessarily homogenize. It has been recognized that the evolution of dislocations is dependent on the crystal orientation in fcc metals[38]. This underpins the evolution of the hardening rate that is perceived in the flow stress and the evolution of the microstructure with increasing levels of strain. For example, the evolution of dislocation cell structures (including cell sizes and/or misorientation across neighbors) during Stage III were found to be orientation-dependent[12, 33].

However, the deformation of hexagonal close-packed single crystal metals (e.g., Mg) is considerably complicated compared with that of FCC ones. The hexagonal close-packed structure results in large anisotropy in critical resolved shear stresses of basal slip systems and non-basal slip systems[58]. For example, crystallographically distinct slip systems involving $\vec{a}$ dislocation feature numerically different critical resolved shear stresses τ_{CRSS}, which follows

$\tau^{\vec{a}}_{CRSS}$ (basal) $\ll \tau^{\vec{a}}_{CRSS}$ (prismatic) $< \tau^{\vec{a}}_{CRSS}$ (pyramidal). This hierarchy of τ_{CRSS} exerts more extreme effects of loading axis orientation. Thus, the mechanical behavior (stress-strain curve) of hcp single crystals is highly orientation-dependent. Furthermore, the occurrence of deformation twinning complicates the situation as it offers an addition pathway for general plasticity of multi-axial strains. The reorientation induced by twinning can strongly modify the crystal orientation (or texture) as deformation continues, and thus significantly alter the hardening effects observed in aforementioned stress-strain curves[21].

2.3 Microstructural Features

During deformation, the original microstructure is subdivided over a wide range of length scales. In this section we will briefly review microstructure features in severe plastic deformation based on length scales as shown in Figure 3.

- **Dislocations:** plastic deformation is accommodated by dislocations, thus the deformed states essentially differs from annealed states from the dislocation density and arrangements. As shown earlier, the moving dislocation interaction with obstacles resulting in multiplication of dislocations. Newly created mobile dislocation can be trapped by existing dislocations (e.g., tangles) or incorporated into substructures. Dislocations stored in this way are termed as statistically stored dislocations (SSDs). If any gradient of plastic strain is present, geometrically necessary dislocations (GNDs) are generated. Plastic strain gradients may appear due to geometry of the bulk (such as existence of cracks), deformation configuration (such as bending), or bulk microstructure (such as existence of secondary phases, grain boundaries). Geometrically necessary dislocations are stored to account for deformation compatibility[6, 26, 28]. Figure 4 depicts the accumulation of geometrically necessary dislocations to accommodate geometrical constraints of the crystal lattice. These geometrically necessary dislocations would act as obstacles for statistically stored dislocations as plastic deformation proceeds.
- **Cells and sub-boundaries:** the dislocation densities increase with strain at the initial stage of deformation, and the majority exist in cellular substructures (but there is also a

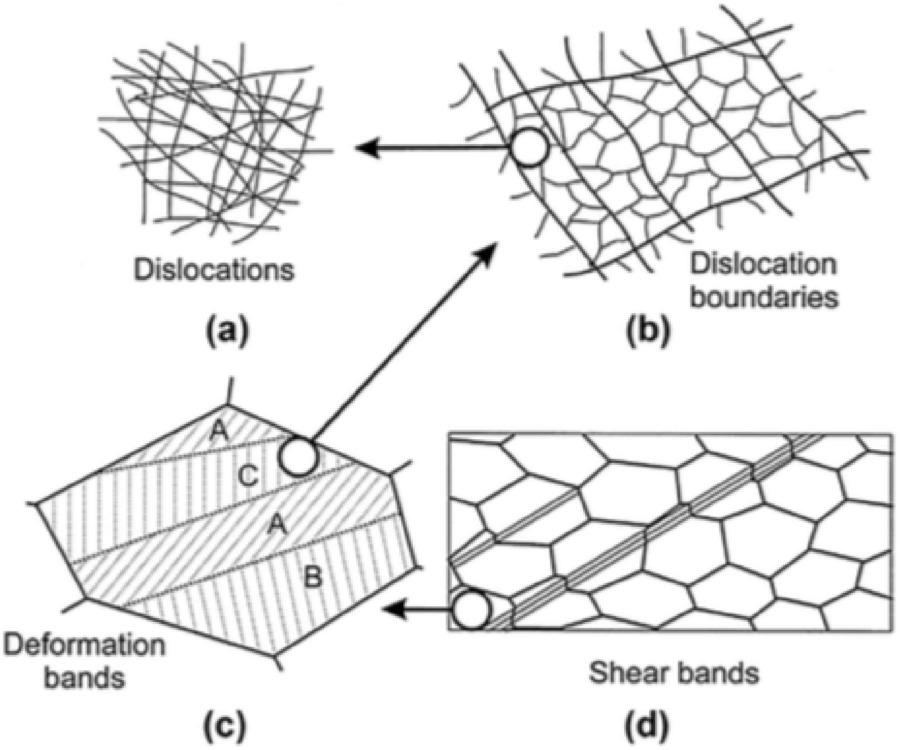

Figure 3: Microstructure over different length scales in deformed materials: (a) dislocations(nanometer scale); (b) dislocation boundaries(micron-sized); (c) deformation and transition bands within a grain (with characteristic width of several to a few tens of micron); (d) shear band (spanning several grains or even entire specimen)[59].

chance of diffuse arrangements of dislocations). With increasing strains, dense dislocation walls (DDWs) are formed surrounding those micron-sized dislocation cells (the smallest volume elements in deformed microstructure) which gradually evolve into cell blocks. In comparison to common cell walls, their misorientations are essentially much higher which can be categorized into sub-boundaries.

- **Deformation bands:** In coarse-grained samples, the localized stresses within individual grains could be inhomogeneous due to neighboring grains or intrinsic plastic instability. Thus, deformation bands (with characteristic width of several to a few tens of micrometer) form due to activation of different slip systems or due to different strain level on the same slip systems. Consequently, individual grains may subdivide into regions with different orientation by deformation bands.
- **Shear bands:** shear bands result from plastic instability, and can pass through multiple grains or even the entire specimen.

Based on their origins, dislocation boundaries can be grouped into two categories: incidental dislocation boundaries (IDBs) which consist of statistically stored dislocations such as DDWs; and geometrically necessary boundaries (GNBs) which is associated with heterogeneous strain/stress states across boundaries, such as boundaries with deformation bands, microshear bands.

2.4 Size Effect in Plastic Deformation

The plastic deformation behavior is fundamentally determined by dislocation activities, which are size-dependent. The size effect on mechanical behavior in plastic deformation can be categorized into two types:

- Intrinsic size refers to those arising from microstructural lengths scale associated with bulk material such as grain size, dislocation density, etc.
- Extrinsic size is associated with the dimensions of the sample involved in deformation.

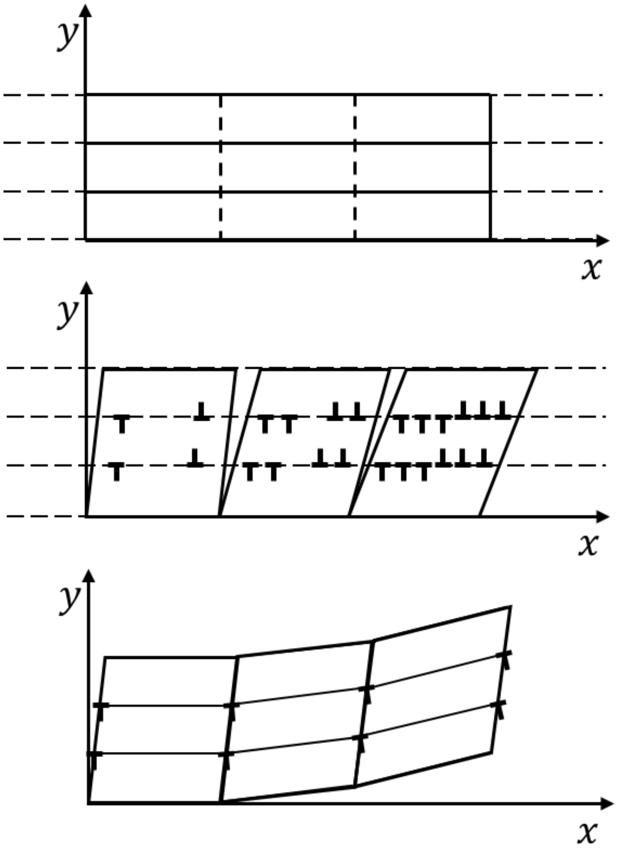

Figure 4: Schematic showing geometrically-necessary edge dislocations accumulate to accommodate geometrical constraints[24]. In the x_1 direction, the slip gradient results in the storage of geometrically necessary dislocations.

Dislocation movement is initiated by applied stresses (higher than τ_{CRSS}) and continues through a crystalline lattice until an interface is reached. In the case of single crystal, dislocation will eventually leave the bulk and create steps on the bulk surface. As for polycrystalline materials, grains boundaries act as such interfaces, while the large mismatch between two adjacent crystal lattices imposes repulsive stresses and impede further dislocation propagation. Thus, dislocations start to pile up and also apply repulsive stresses against grain boundaries. On reaching a critical value, dislocations can move across the grain boundary and the deformation continues into adjacent grain to further accommodate the macroscopic strain. Reducing grain size leads to less dislocation pile-ups and necessarily reduces the resulting repulsive stresses, so higher external stresses are needed for dislocation transition across grain boundaries. The classical Hall-Petch relation describes this characteristic "smaller is stronger" trend in polycrystalline material down to grain sizes of $\sim$ 40nm[30]

$$\sigma = \sigma_0 + kd^{-1/2} \tag{2.2}$$

where σ is the yield strength of the bulk, k is a material constant and d is the average grain size.

As for the region of grain size below $\sim$ 40nm, dislocation activities are quite limited so alternative plastic deformation mechanisms (like grain boundary sliding[64, 74]), which gives rise to the so-called "inverse" Hall-Petch relation (as shown in Figure 5).

With advances in fabrication processes for precise geometry control down to sub-micron regime, an additional size effect has been discovered: the material strength increases with decreasing sample dimensions. One example is shown in Figure 6 where pure Ni micropillars with different diameters are tested using uniaxial compression. It can be clearly seen that the yield strength increases with decreasing diameters of micropillars and also large strain bursts are observed in smaller samples. The following equation describes the general relation between yield strength and sample dimensions[73]:

$$\frac{\sigma}{G} \propto \left(\frac{D}{b}\right)^n \tag{2.3}$$

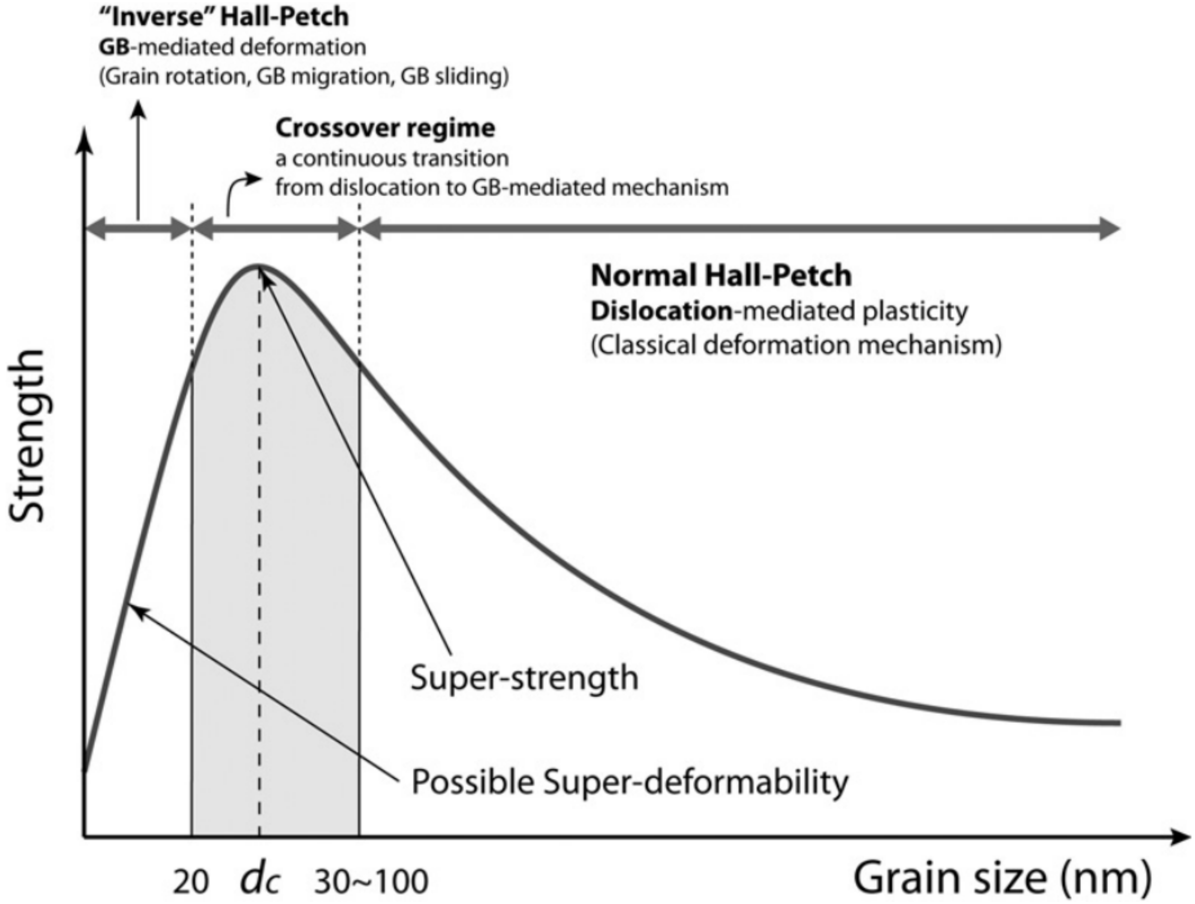

Figure 5: Strength versus grain size: from Hall-Petch relation to "inverse" Hall-Petch relation[27].

where σ is the yield strength, G the shear modulus, D the diameter of the micropillar, and b the Burgers vector. In such confined volumes, the active dislocation sources are quite limited. New dislocations ought to be nucleated from the micropillar surface and they (including pre-existing dislocations) tend to escape from the volume of micropillar. The observed strain bursts are attributed to the inherently discrete plastic flow[18]. Dislocation source truncation mechanism has been proposed for the rationalization of size effect by considering the stochastic of dislocation source lengths in finite sample volume[52]. The critical resolved shear stress for a dislocation source is calculated as [52]:

$$\tau_{\mathrm{CRSS}} = \alpha \frac{Gb}{L} + \beta G b \sqrt{\rho_{\mathrm{tot}}} + \tau_0 \tag{2.4}$$

where α and β are constants, L the effective source length, G the shear modulus, b the Burgers vector, τ_0 the stress required to overcome lattice friction and ρ_{tot} the total dislocation density. The effective source length L is positively related with sample dimension D (diameter of a cylinder), i.e. $L \sim kD$ for a given Burgers vector b. From the equation above, reducing sample dimension decreases L and thus increases τ_{CRSS}.

2.5 Dynamic recrystallization

Recrystallization refers to the change from deformed microstructure to generation of new grains during annealing, which is also termed as static recrystallization (SRX)[59]. New grains are generated via distinguishable stages of nucleation and subsequent grain growth and this process is often termed as discontinuous static dynamic recrystallization (DSRX) as shown in Figure 7. At the early stage of annealing, static recovery (SRV) results in recrystallization nuclei and the stored energy associated with dislocations and substructures drives the following growth of new grains, where the misorientation of boundaries gradually increases and low-angle boundaries evolve into high-angle boundaries[22]. Meanwhile, the aforementioned recrystallization can also happen homogeneously over the entire deformed microstructure, i.e. continuous static recrystallization (CSRX)[22].

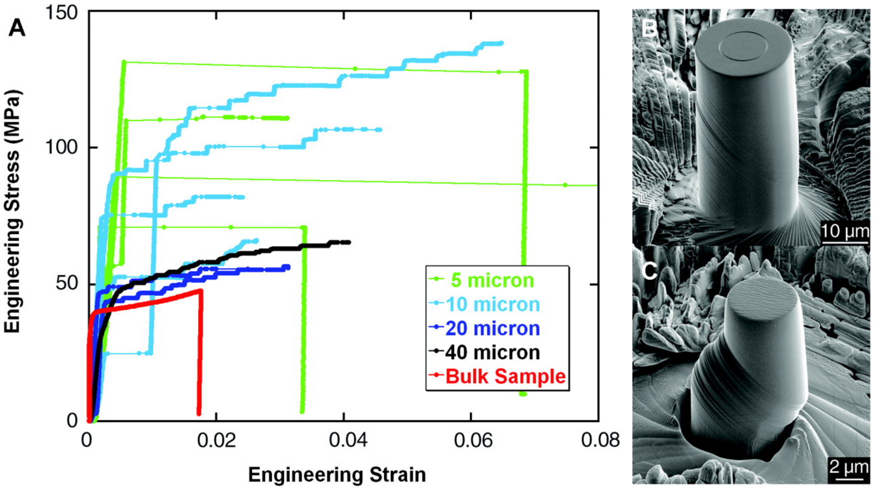

Figure 6: (a) Stress-strain curves for pure Ni micropillars with different diameters under uniaxial compression. SEM images of micropillars undergone ∼ 4% strain (b) and ∼ 19% strain (c).[73]

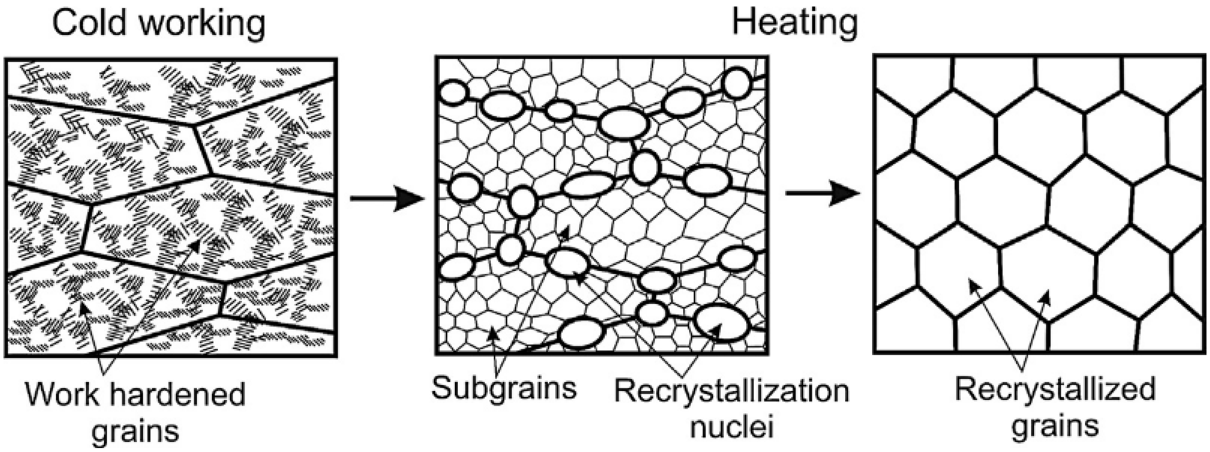

Figure 7: Schematic representation of the discontinuous static recrystallization (dSRX)[61].

Recrystallization can also occur during deformation process, which is referred to as dynamic recrystallization (DRX). In the case of hot deformation (i.e. the temperature is above about $0.5T_m$), recrystallization nuclei develop at the initial straining stage (i.e. nucleation stage) and grains grow through consumption of dislocations, which is analogous to DSRX. Thus, this dynamic process is referred to as discontinuous dynamic recrystallization (DDRX). In contrast to CDRX, dislocation substructures are still present even after full recrystallization. Continuous dynamic recrystallization (CDRX) occurs during plastic deformation but in a totally different way. The dislocation activities during deformation process result in progressive formations of sub-boundaries including IDBs (incidental dislocation boundaries) and GNBs (geometrically necessary boundaries). With further imposition of plastic strain, these subgrain boundaries evolve to high angle grain boundaries.

2.5.1 Continuous Dynamic Recrystallization in Severe Plastic Deformation

In crystalline metals, severe plastic deformation typically results in ultrafine-grained (UFG) microstructures. Upon the initial straining, dislocation sub-boundaries forms featuring low misorientations. The dislocations densities within cell interior and also sub-boundaries increases with continuous straining. As a result, low angle boundaries (LABs) gradually evolve into HABs, which is the core of CDRX.

Another version of CDRX occurs in severe cold rolling process, i.e. geometric dynamic recrystallization. With directional straining, pancake-shaped grains form with elongation along the rolling direction. The space between HABs decreases with increasing strains, while the minimum cell size remains independent of strain levels. As these two lengths approach, the pancake-shaped grains subdivide through pinch-off of serrations, resulting in microstructure with mixed LABs and HABs. These HABs are generally categorized into GNBs.

The grain refinement in severe plastic deformation results from gradual reorientation of cell/subgrains. Continuation of plastic deformation leads to multiplication of dislocations. The increase in dislocation density within cell interior volume increases the boundary misorientation, which accompanies the boundary sliding. In such a way, dislocation sub-boundaries

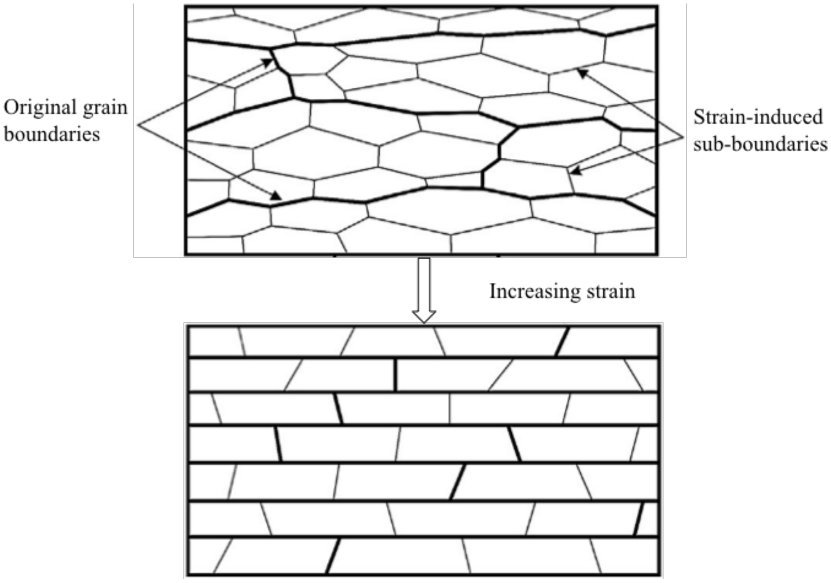

Figure 8: Geometric dynamic recrystallization. With increasing strain, the space between HABs becomes closer to the subgrain size. Grain subdivision occurs through pinch-off serration[59].

(with low misorientation) evolve with strain and eventually transform into HABs associated with large strains. In case of inhomogeneous straining, the crystallographic curvature is accommodated by GNBs. The corresponding increase in dislocation densities lead to the additional formation of strain-induced boundaries. When deforming polycrystalline metals, new grains develop mainly in the vicinity of grain boundaries due to the locally distorted strain state. Additionally, these boundaries can also form in accordance with high strain gradients.

2.5.2 Effect of Solutes on Dynamic Recrystallization

The addition of alloying elements to pure metal typically result in retarded recrystallization due to solute drag effect. For example, in Mg AZ31, the presence of aluminum solutes would reduce the dislocation mobility due to its interaction with dislocations and/or a potential drop in stacking fault energy. Thus, dynamic recovery (DRV) would be hindered[42]. The effect of aluminum solutes on dislocation movements can be weakened with increasing strain rates and stresses due to break-away of dislocations from solutes atmosphere[67]. Meanwhile, the segregation of zinc solutes at grain boundaries would greatly affects the mobility of grain boundaries as it changes the apparent activation energy for boundary migration[43].

2.6 Machining Process

Machining is a highly coupled physical and mechanical process where a wedge shaped tool is advanced relatively against a metal workpiece as shown in Figure 9. The volume of material being cut in machining is defined by the preset depth of cut a_0. A certain amount of strain is imposed via simple shear as it passes through the primary shear zone. As the chip proceeds up the face of the cutting tool, no further plastic flow is assumed. The amount of shear in secondary shear zone is generally very small compared with that in primary shear zone and thus ignored. The roughness of back of a chip is mainly raised by the inhomogeneous strain. Other parameters involved include rake angle α and velocity of tool advancement V (also in Figure 9).

When the chip width w_c (also the width of workpiece) is much larger than preset depth of cut a_0, plane strain conditions are assumed in the primary shear zone. In this configuration, shear angle ϕ can be calculated as (based on conservation of volume)

$$\tan\phi = \frac{\frac{a_0}{a_c}\cos\alpha}{1 - \frac{a_0}{a_c}\sin\alpha} \tag{2.5}$$

The shear angle ϕ is a function of thermo-mechanical conditions in the deformation zone and the bulk material properties. The effective shear strain imposed on the material as traversing through deformation zone can be estimated as[65]

$$\varepsilon_{\text{eff}} = \frac{\cos\alpha}{\sqrt{3}\sin\phi\cos(\phi - \alpha)} \tag{2.6}$$

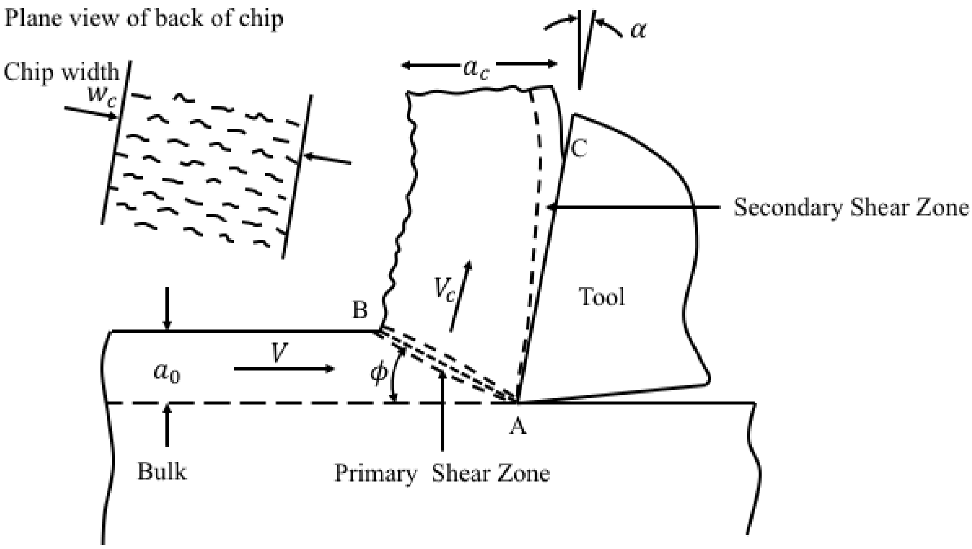

Figure 9: Schematic of orthogonal steady state machining process[65].

When machining ductile materials like Cu[1, 2, 66], high strain values ($\gg 1$) can be achieved, i.e., severe plastic deformation (SPD). As shown in Figure 9, bulk materials undergo progressive plastic deformation through the deformation zone into the chip, which inevitably introduces spatial strain gradient fields from pristine bulk to deformed chips. Clearly this strain gradient field increases with decreasing thickness of deformation zone and thus with decreasing depth of cut a_0. Given that the characteristic sizes of deformed microstructure become comparable with preset depth of cut a_0, anomalies in microstructure evolution can arise like in Refs.[9, 10].

2.7 Material Systems

2.7.1 Copper

Copper has a face centered cubic (FCC) structure (as shown in Figure 10), with lattice parameter $a = 0.3615$nm. The plane with densest atomic packing is $\{111\}$ family and the

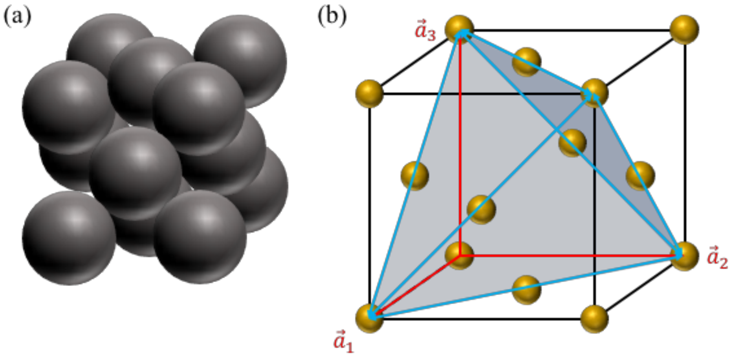

Figure 10: Crystal lattice of Cu face centered cubic (FCC) structure: (a) atom stacking; (b) ball-stick model with three-axis coordinate system $(\vec{a}_1, \vec{a}_2, \vec{a}_3)$ with slip systems indicated.

close-packed atomic direction is $\langle 110 \rangle$ family. There are 12 independent slip systems in such FCC structure as shown in Figure 10(b).

2.7.2 Magnesium

Magnesium has a hexagonal close-packed (HCP) structure (as shown in Figure 11), with lattice parameters $a = 0.3209$nm and $c = 0.5211$nm, where the ratio $c/a = 1.624$, is very close to that of the ideal HCP lattice (with $c/a = 1.633$). The plane with densest atomic packing is (0001) and the close-packed atomic direction is $\langle 2\bar{1}\bar{1}0 \rangle$, which defines the easiest slip system, basal slip system involving the slip of $\vec{a}-$type dislocation with Burgers vector $b = \frac{1}{3}\{11\bar{2}0\}$. Earlier studies on plastic deformation behavior of magnesium single crystals concluded that there are only two independent basal slip systems (although the total number is three)[31]. These two slip systems are not enough for general ductility based on Taylor criterion [72] (where at least five independent slip systems are required), and also cannot accommodate any strain along $\vec{c}$-axis. In order for arbitrary shape change, non-basal slips are required. All possible slip systems in HCP metals are summarized in Table 1 and shown in Figure 12[53, 80].

All possible slip systems in HCP metals are summarized in Table 1 and shown in Figure 12[53, 80]. At ambient temperature, the critical resolved shear stress $\tau_{\text{CRSS}}^{\text{non-basal}}$ for non-basal

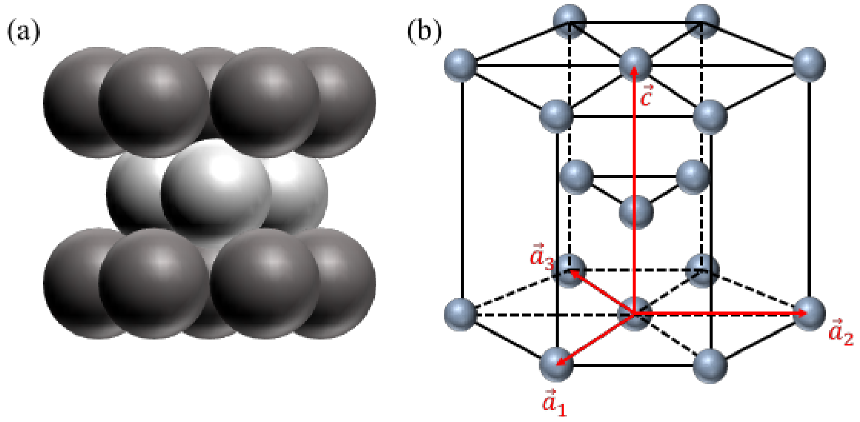

Figure 11: Crystal lattice of Mg hexagonal close-packed (HCP) structure: (a) atom stacking; (b) ball-stick model with four-axis coordinate system ($\vec{a}_1, \vec{a}_2, \vec{a}_3, \vec{c}$).

slip is ~ 100 higher than that of basal slip $\tau_{\text{CRSS}}^{\text{nonbasal}}$[34, 39]. With increasing temperature the ratio $\tau_{\text{CRSS}}^{\text{nonbasal}}/\tau_{\text{CRSS}}^{\text{basal}}$ due to the fact that $\tau_{\text{CRSS}}^{\text{nonbasal}}$ decreases rapidly while $\tau_{\text{CRSS}}^{\text{basal}}$ is not quite sensitive to temperature. Thus, multiple slip systems can be readily activated at elevated temperature which accounts for improved ductility.

In crystals with low symmetry (like the case of HCP magnesium), twinning offers more options for plastic deformation. Deformation twinning forms during plastic deformation (by shear similar to slip), where cooperative motion of atoms are involved resulting in new structure with mirror symmetry[16, 37]. Figure 13(a) shows a schematic of twinning event. The invariant plane in this shear is denoted by K_1, and the direction of shear in K_1 is η_1; the second undistorted plane is K_2; the plane of shear S is the one perpendicular to both K_1 and K_2; and the intersection of S and K_2 is η_2[11].

Deformation twinning leads to an abrupt grain reorientation compared to the gradual reorientation in dislocation slips, and the deformation via twinning is more heterogeneous compared with dislocation slips. Also, the amount of strain accommodated by twinning is directly related to the volume fraction of twinning crystal, and also quite limited. Meanwhile, deformation twinning is a polar mechanism, meaning the shear is directional (the simple shear are not equivalent in forwards and backwards directions). Although being an important

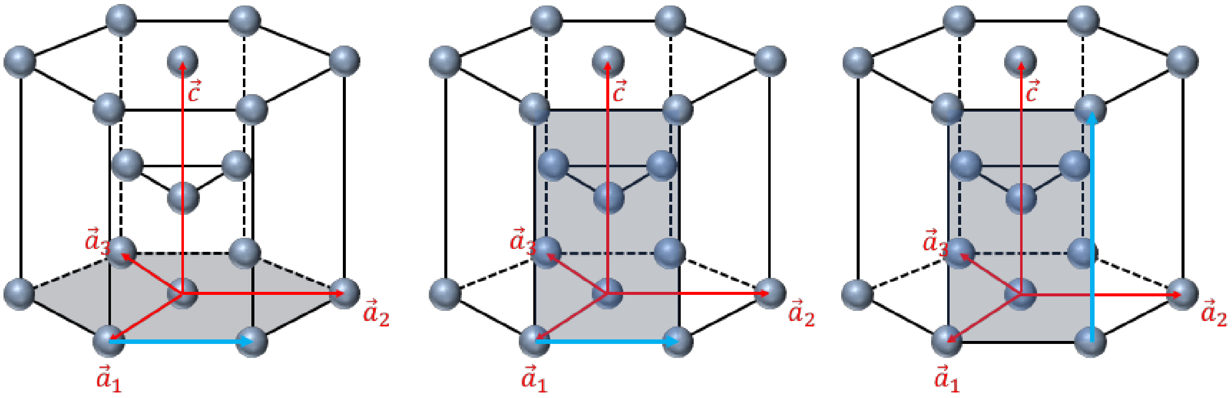

Basal Slip: $\{0001\}\langle 11\bar{2}0\rangle$

1st order Prismatic Slip: $\{10\bar{1}0\}\langle 11\bar{2}0\rangle$

1st order Prismatic Slip: $\{10\bar{1}0\}\langle 0001\rangle$

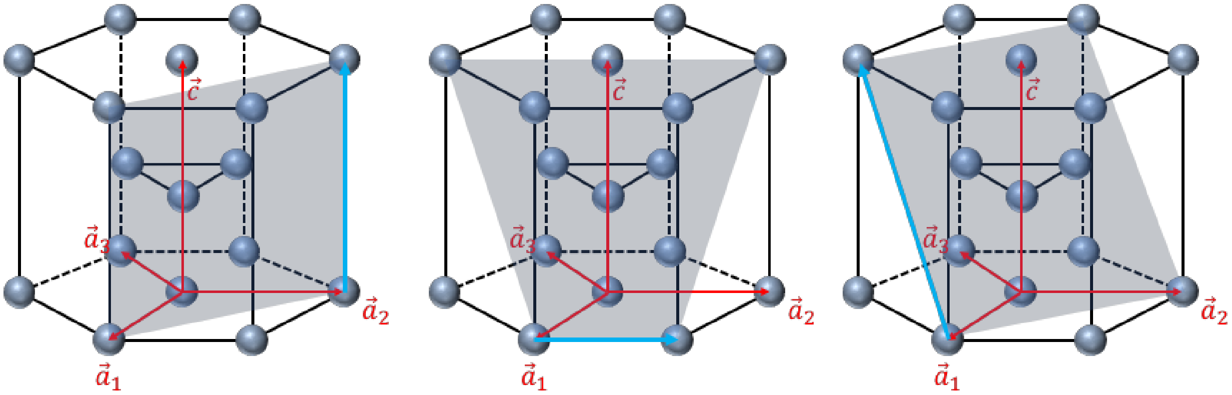

2nd order Prismatic Slip: $\{11\bar{2}0\}\langle 0001\rangle$

1st order Pyramidal Slip: $\{10\bar{1}1\}\langle 11\bar{2}0\rangle$

2nd order Pyramidal Slip: $\{11\bar{2}2\}\langle 11\bar{2}3\rangle$

Figure 12: Slip systems in magnesium.

Table 1: Available slip systems in HCP metals[53, 80]

Slip system	Slip direction	Slip plane	Burgers vector type	Number of slip system
Basal	$\langle 11\bar{2}0\rangle$	Basal plane: $\{0001\}$	$\vec{a}$	3(Independent: 2)
Prismatic	$\langle 11\bar{2}0\rangle$	1^{st}order prismatic $\{10\bar{1}0\}$	$\vec{a}$	3(Independent: 2)
	$\langle 0001\rangle$	1^{st}order prismatic $\{10\bar{1}0\}$	$\vec{c}$	3(Independent: 2)
	$\langle 0001\rangle$	2^{nd}order prismatic $\{11\bar{2}0\}$	$\vec{c}$	3(Independent: 2)
Pyramidal	$\langle 11\bar{2}0\rangle$	1^{st}order pyramidal $\{10\bar{1}1\}$	$\vec{a}$	6(Independent: 4)
	$\langle 11\bar{2}3\rangle$	2^{nd}order pyramidal $\{11\bar{2}2\}$	$\vec{c}+\vec{a}$	3(Independent: 2)

option for plastic deformation in HCP metals, the deformation twinning could lead to large internal stress (even rapid failure) in the absence of stress relaxation. The axial ratio c/a has an important effect on the possible operations twinning systems under various stresses conditions. For example, in the range of $1.5 < c/a < 1.9$, the $\{11\bar{2}1\}$ is tension twin while $\{11\bar{2}2\}$ and $\{10\bar{1}1\}$ are compression twins[79]. In magnesium, the most common twinning systems are $\{10\bar{1}1\}\langle 10\bar{2}\bar{2}\rangle$ and $\{10\bar{1}2\}\langle\bar{1}011\rangle$ (Figure 13(b)).

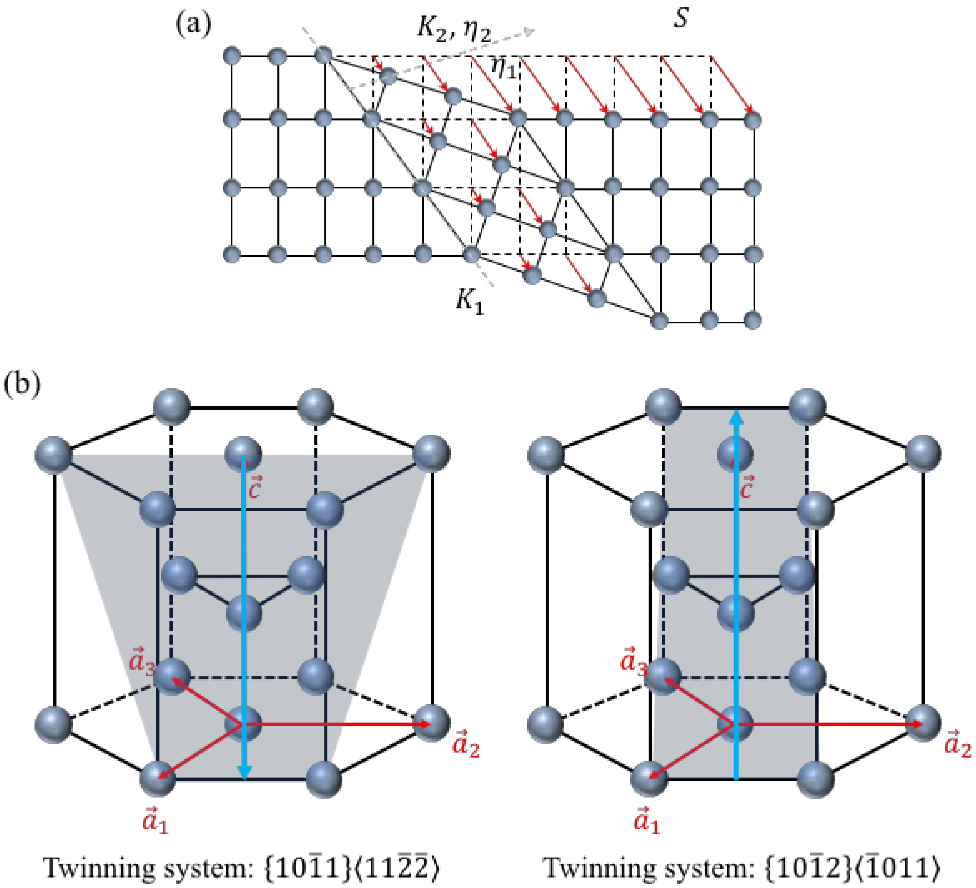

Figure 13: (a) Schematic of twinning. (b) The most common deformation twinning systems in magnesium $\{10\bar{1}1\}$ $\langle 10\bar{2}\bar{2}\rangle$ and $\{10\bar{1}2\}$ $\langle \bar{1}011\rangle$.

3.0 Experimental Techniques

Several experimental techniques are involved in the investigation of the deformation mechanics and microstructure evolution during plain strain machining at the micro/nano-scale. In this chapter, these experimental instruments, operational procedures and techniques of data analysis in this research work are explained in details.

3.1 Customized Stage to Perform *in situ* Machining

A customized sub-stage (as shown in Figure 14) was developed to perform *in situ* micro/nano-machining inside the vacuum chamber of a Thermo Scientific$^{\text{TM}}$ Apreo Scanning Electron Microscopy (SEM). In this configuration, motions along two perpendicular axes (labeled as x-axis and y-axis in the sketch) are provided by two mechanical actuators (with Part No.: BG1501A-75H/R0, from Nippon Bearing Co.) which are assembled on an L shape stainless steell frame. These actuators are driven by two steps motors (with Part No.: CRK513PAP-H100 from Oriental Motors U.S.A. Corp.) through a rack-and-pinion gear set. A commercially available single crystalline diamond cutting tool with edge of radius < 25nm (from Technodiamant) is advanced relatively against the bulk material (a thin square sheet with rough dimensions of 10mm$\times$10mm$\times$0.3mm). The depth of cut is preset by the x-axis motion which goes as small as $\sim$ 100nm and the machining velocity is controlled by y-axis motion with a range from 100μm/s to several mm/s. This plane strain machining configuration on this sub-stage exposes the "stationary" deformation zone directly to the electron beam which allows for detailed characterization of deformation behavior utilizing high-magnification secondary electron imaging during *in situ* micro/nano-machining experiments, such as continuous material flow through the narrow deformation zone, chip morphology and so on.

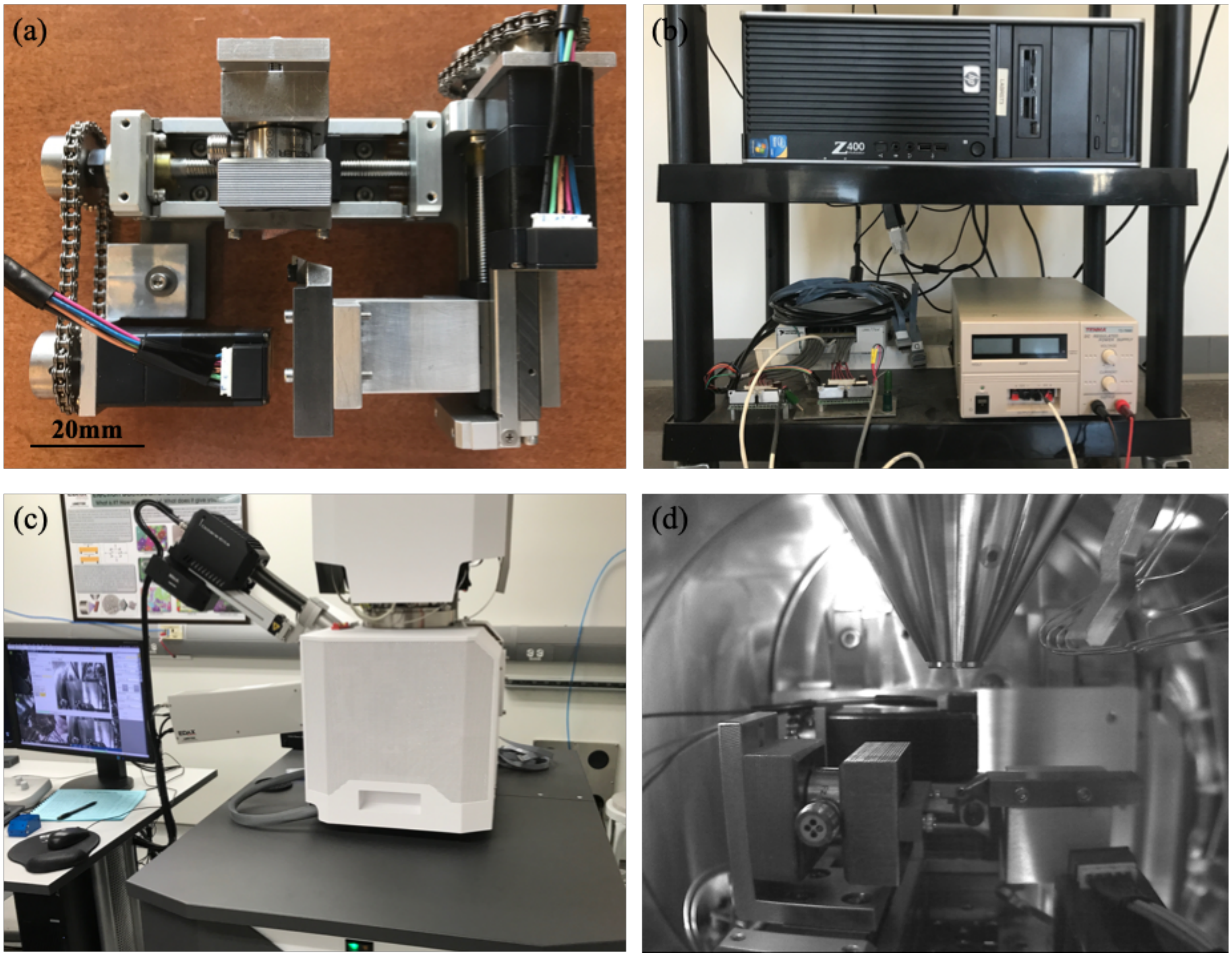

Figure 14: (a) Customized substage for performing machining inside vacuum chamber of scanning electron microscope. (b) Supportive system for machining stage. (c) Thermo Scientific$^{\text{TM}}$ Apreo SEM with feed through component for power controlling signals during *in situ* experiments. (d) Image of machining stage inside the chamber of SEM.

3.2 Sample preparation via focused ion beam

Given the length scales of deformation (micrometer or sub-micrometer), especially in magnesium, TEM characterization is necessary to reveal the microstructure evolution. Considering the size of deformed chips from machining, it is almost impossible to do TEM sample preparation via conventional methods. Focused Ion Beam (FIB) provides the right method to produce TEM-ready sample directly out of tiny volumes, which will also assist in the need of site-specific characterization.

3.2.1 Cross section of deformed chips

Figure 15 illustrates the full process to prepare a cross section sample from a freshly machined Mg AZ31 chip using Thermo Scientific$^{\text{TM}}$ Scios$^{\text{TM}}$ DualBeam$^{\text{TM}}$ with Focused Ion Beam(FIB)/Scanning Electron Microscope. After 2μm-thick Pt deposition on the backside of Mg AZ31 chip for protection, the cross section can be safely extracted. Then the probe is rotated by 180° and the sample is welded to the PELCO$^{®}$ FIB Lift-out TEM grid. After milling the probe free from sample, rotate the stage by 180°. Once again, attach the sample to the probe and rotate the probe by 180° and then weld the sample to the side of one narrow post on FIB grid.

Proper thinning using ion milling is required to get the cross section sample transparent when exposed to electron beam inside the TEM. An accelerating voltage of 30kV for ion source is used initially to rapidly reduce the thickness down to $\sim$ 150nm. Then fine polishing using accelerating voltage of 5kV and 2kV helps to further reduce the thickness and more importantly to reduce the damage (Pt contamination, amorphous layer, etc.) on both sides which are induced by high-energy ion beam.

To further remove the FIB-induced damage layer, milling process by Ar ion source is also performed using Fischione Model 1040 NanoMill$^{®}$ TEM specimen preparation system. An accelerating voltage 500V, and beam current 135pA, are used to do milling on both the front side at 15° and back side at $-10°$ for 10mins to further reduce the damage layer and to prevent Pt re-deposition from sample preparation process.

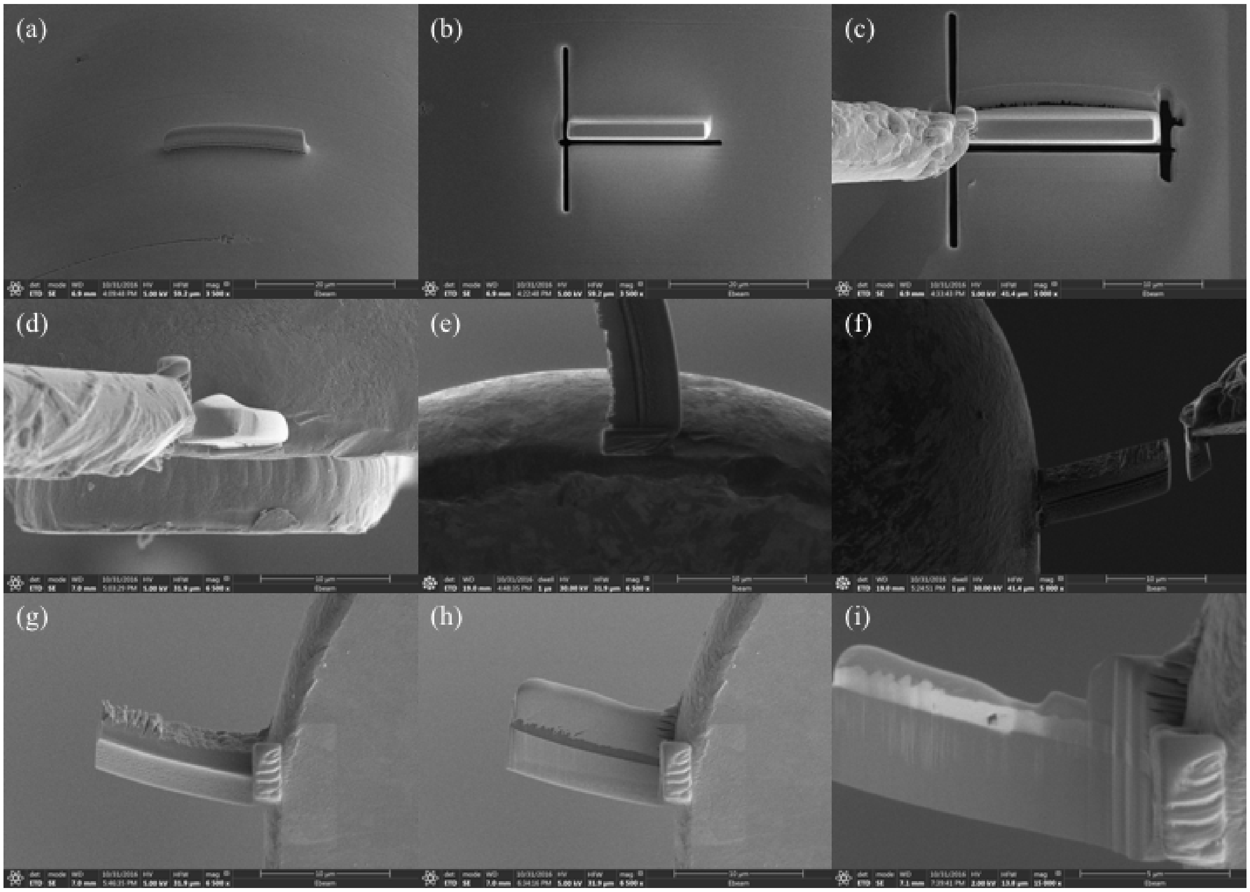

Figure 15: Full process to extract a cross section from Mg AZ31 chip using FIB: (a) Pt deposition at 52°-tilted position; (b) Ion mill to partially relieve the cross section from the bulk chip; (c) Attach the cross section sample to the sharp probe and lifting it out from the bulk chip; (d) Rotate the probe 180° and transferring the cross section sample to the top of one narrow post of FIB copper grid; (e) Mill the cross section sample off after 180° rotation of the FIB grid; (f) Reattach the cross section sample to the side part of FIB copper grid; (g) Cut the sample free from sharp probe; (h) Pt deposition on the top surface at 52°-tilted position; (i) Thin the sample down to proper thickness using ion milling.

3.2.2 Samples of partially detached chips

When performing machining experiments inside SEM vacuum chamber, the diamond cutting tool can be stopped at a fixed distance from its last stopping position, leaving a series of chips attached to the bulk material. These partially detached samples contain full trajectory from bulk samples into fully deformed materials. In order to reveal the corresponding microstructure evolution, the following method has been developed to extract specimen with partially detached chips, as shown in Figure 16.

3.3 Orientation Imaging Microscopy via TEM

The electron beam interacts strongly with atoms in the crystalline metals. The diffracted beam is also in perfect Bragg condition to be re-diffracted back to the same set of crystal planes, and this process can continue again and again. Therefore, this dynamical scattering increases with increasing sample thickness. Furthermore, the dynamical diffraction could result in extra diffraction spots which jeopardizes interpretations of crystal orientation. Utilization of precession will eliminate these extra spots, leaving only high-quality kinematical diffraction. In precession diffraction, the electron beam is deflected using the DF scan coils to form a circular hollow cone, i.e., at a selected angle with respect to the centered electron optic axis and de-scanned again below the sample onto the plane of the DP, as shown in Figure 17(a). The net effect from this double conical beam-rocking system is equivalent to diffraction from a fixed electron beam parallel to the optic axis. In precession, the diffraction conditions from selected area could be averaged out and the diffraction spots correspond to merely a two-beam condition with reduced dynamical diffraction.

When a convergent beam is shined on a sample, the generated electron diffraction (CBED) spot pattern is determined by the underlying crystal structure. Utilization of precession electron diffraction generates a quasi-kinematical diffraction pattern with broader range of reflections, which improves the quality as input to determine the crystal structure of the sample. The underlying crystal information can be inferred by comparing this actual

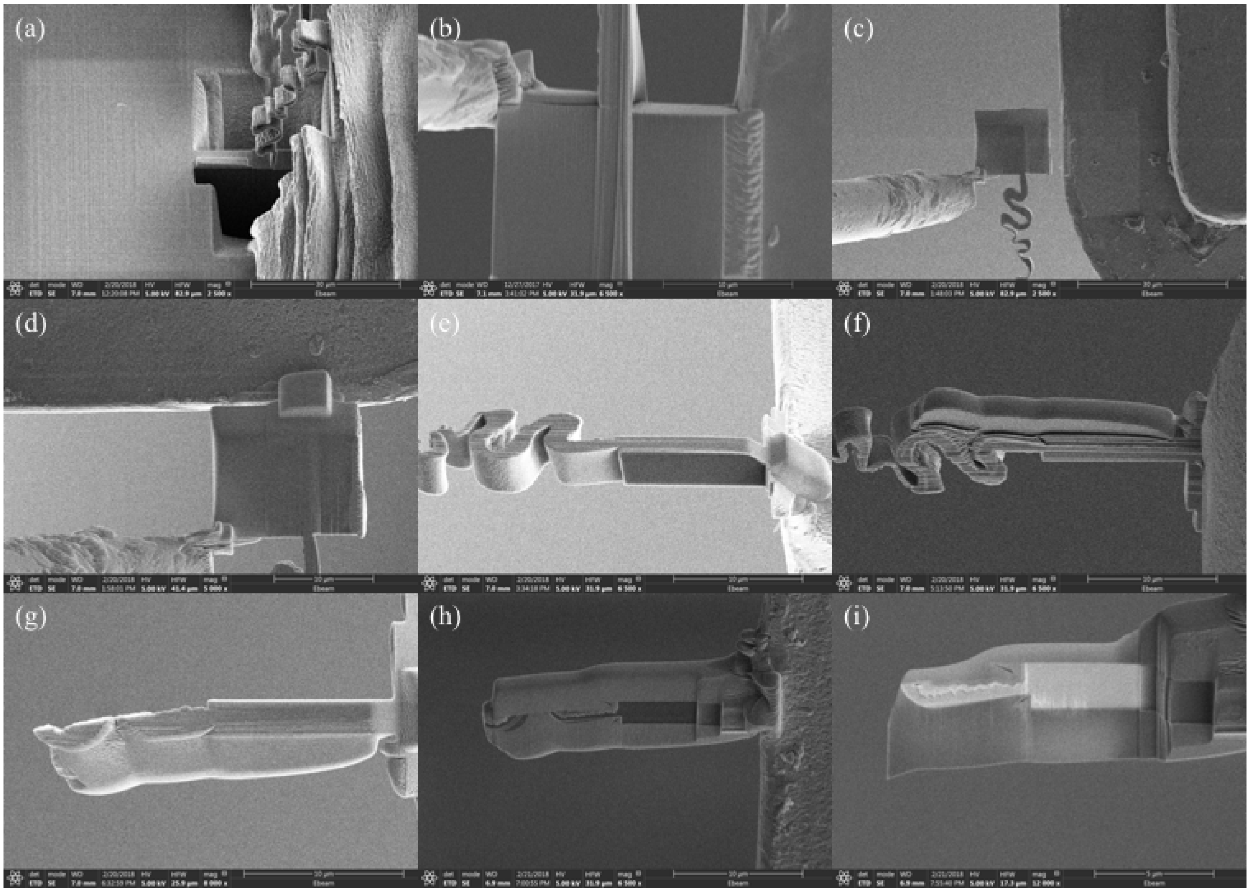

Figure 16: Full process to extract a sample of partially detached chip using FIB: (a) Ion milling to isolate a partially detach chip; (b) Attach the partially detached sample to one narrow post of Lift-out grid; (c) Put the grid on the horizontal position and detached the sample from the grid; (d) Rotate the stage by 90° and re-attach the sample to the grid; (e) Get rid of unnecessary parts of the bulk grain; (f) Put the grid pack in vertical position and deposit Pt protection layer; (g) Revert the sample by 180°; (h) Deposit Pt protection layer; (i) Thin the sample down to proper thickness using ion milling.

pattern with simulated standard ED templates via cross-correlation matching techniques. The above procedure is repeated over a selected area to generate corresponding orientation map. The orientation imaging microscopy is performed using ASTAR from NanoMEGAS in a FEI Tecnai G2 F20 200kV field emission TEM. The electron beam is scanned with beam precession in an Scanning Transmission Electron Microscope (STEM) mode. A series of ED spot patterns from the sample area of interest are recorded using high speed CCD camera which is placed in front of TEM fluorescent screen. The orientation and/or phase mapping of a sample area can be generated by sequential index of individual ED spot pattern.

Orientation imaging microscopy of the FIB samples is performed using NanoMEGAS hardware and ASTAR$^{\text{TM}}$ on a FEI Tecnai G2 F20 200kV field emission TEM. The electron beam is scanned with beam precession in Scanning Transmission Electron Microscope (STEM) mode. A series of ED spot patterns from the sample area of interest are recorded using high speed CCD camera which is placed in front of TEM fluorescent screen. The orientation and/or phase mapping of a sample area can be generated by sequential index of individual ED spot pattern, as shown in Figure 17.

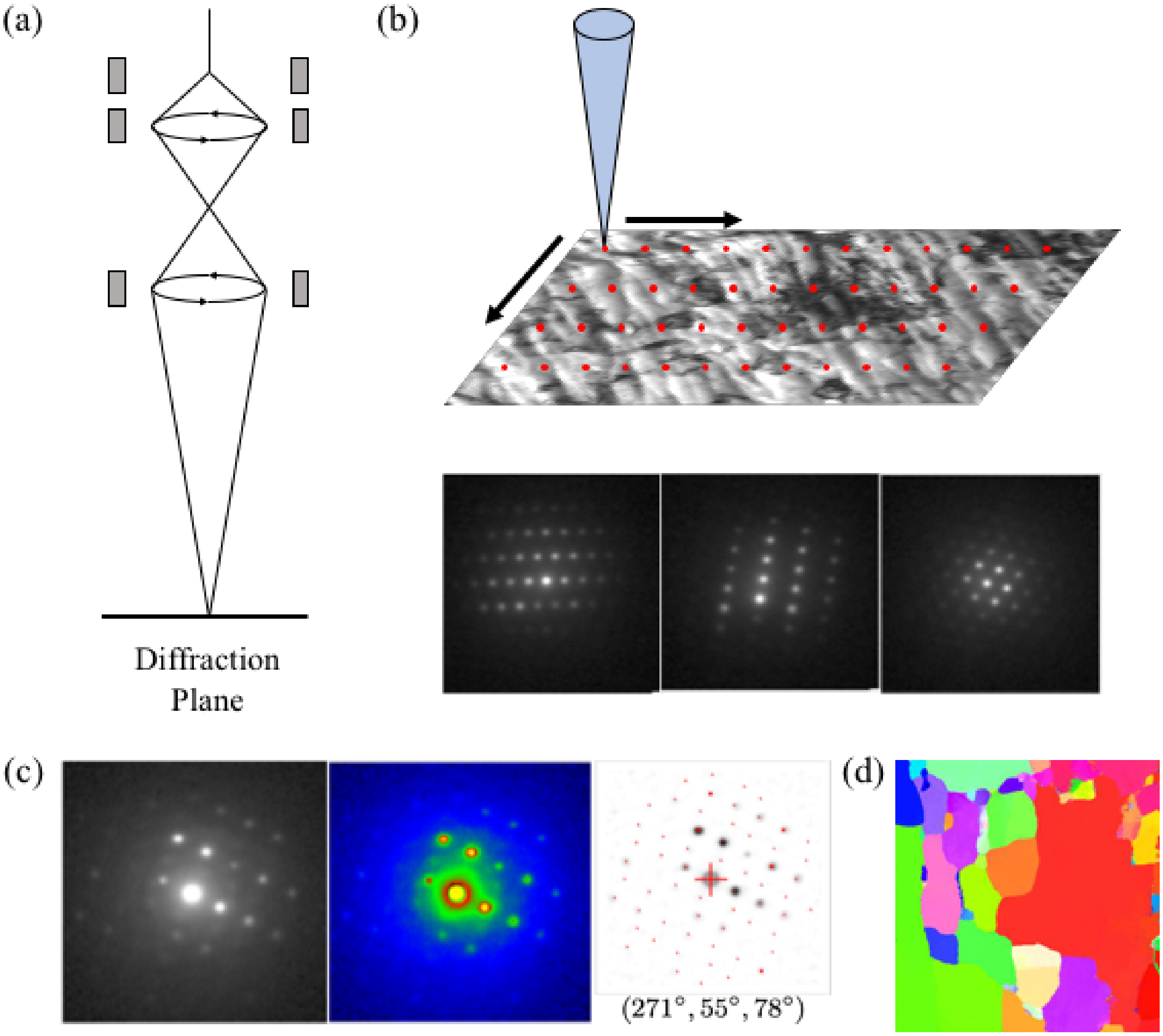

Figure 17: Schematic illustration of orientation indexing microscopy using ASTAR^{TM} system on a TEM. (a) A schematic diagram for precession electron diffraction (PED). (b) Sequential acquisition of CBED patterns from sample area in STEM mode. (c) Orientation indexing via cross-correlation matching with standard patterns. (d) Resultant orientation map after indexing.

4.0 Deformation Anisotropy in Micromachining of Copper

(*Contents from this chapter were used in other publications, proceedings and project reports.*)

In this chapter, we examine the orientation-dependent anisotropy during severe plastic deformation in plain strain machining of Cu at the micrometer length-scale. Deformation mechanics is characterized by performing Digital Image Correlation (DIC) on a sequential secondary electron images of deformation zone from different bulk grains which are obtained during *in situ* machining experiments. Corresponding microstructure evolutions are examined by Orientation Imaging Microscopy (OIM) using Electron Backscattered Diffraction (EBSD), which is overlaid with aforementioned deformation mechanics to characterize the orientation-dependent anisotropic response despite of identical deformed conditions (imposed by combination of machining parameters). In conjunction with anisotropic intra-granular deformation, inter-granular heterogeneity induced by grain boundaries (GBs) are also measured. The combined efforts hold consequences for modulating mechanical properties via novel microstructural design. Meanwhile, the topographical integrity of machining surface is inherited from the modification of the deformation zone and subsequent microstructure evolution due to various alignments of bulk orientation with respect to single-crystal diamond machining tool. This characterization would be directly relevant to controlling the surface integrity which is inherently a function of underlying bulk microstructure, i.e. microstructure engineering for enhanced machinability.

4.1 Experiment setup

Figure 18a shows a schematic representation of micromachining experiments (the corresponding sub-stage with mounted Cu workpiece is shown in Figure 18b), and the deformation zone sits in the area ahead of diamond cutting tool tip, where the characteristic length-scale, i.e., thickness of deformation zone t_D of the deformation volume can be varied from the nanometer length-scale to the macroscopic length-scale depending on the choices of preset depth of cut a_0. As for machining experiments explored here, machining velocity V was kept at a constant value of 150μm/s and preset depth of cut a_0 was varied from $1\mu m$ to $5\mu m$. The rationality of these choices is explained later.

Bulk material examined here, Oxygen-Free High Conductivity (OFHC) copper sheet (with purity $\sim$ 99.99%) was annealed at 700°C for 2hours and then cooled down in the air to release dislocations (and/or potential substructures left from previous plastic deformation in manufacturing process). The copper sheet was then cut into pieces of 10mm×10mm by diamond saw. To reveal the microstructure of the bulk copper, the workpiece was mounted with epoxy and then polished following standard metallographic preparation procedure (through 9μm, 6μm, 3μm and 1μm) down to a final step with 0.04μm colloidal silica suspension on Struers Tegramin 25. Although the resultant mirror-like surface directly out of mechanical polishing typically yields orientation imaging microscopy (OIM) with high quality via electron backscatter diffraction (EBSD), it lacks sufficient contrast (in absence of surface asperities) for identification of individual grains from secondary electron (SE) imaging during *in situ* experiments. Thus, freshly polished surface was etched by mixture of acetic and nitric acid (with volume ratio 1:1) for around 10 to 20 seconds. Due to anisotropic corrosion resistance, this etching exerts a controlled effect on surface profile which provides a unique signature to identify each grain being cut by single-crystal diamond tool during *in situ* experiments with reference to corresponding crystal orientation map from EBSD as shown in Figure 18c. Subsequently, the mounted sample was immersed in acetone to dissolve the epoxy so the Cu workpiece can be removed without damage.

From Figure 18c, the average grain size of bulk Cu is about $\sim 100\mu$m. When comparing to the preset depth of cut a_0 (typically $\leq 5\mu$m) explored in this work, this deformation configuration samples only a small fraction of a single grain in a given increment of time as shown in the SE image of Figure 18c when viewing along $y-$axis in Figure 18a but multiple grains simultaneously along $z-$axis given thickness of workpiece. So the material response to severe plastic deformation can be evaluated on a grain scale. Meanwhile, over the time domain of whole machining process, grain boundaries are encountered inevitably as in Figure 18d.

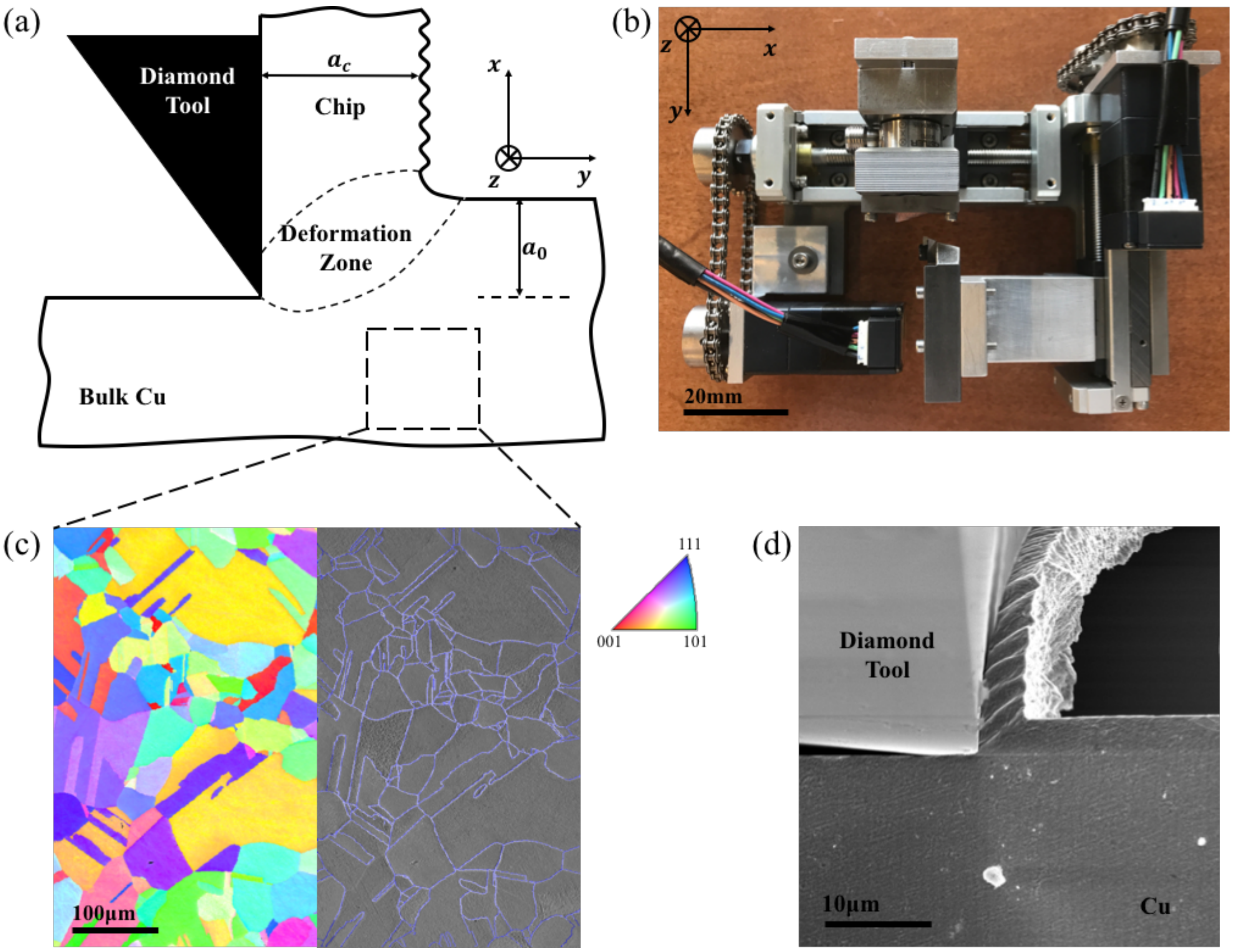

Figure 18: (a) A schematic representation of plane strain machining used to impose large shear deformation. (b) Customized sub-stage to perform *in situ* micromachining experiment inside the vacuum chamber of SEM. (c) Secondary electron image and corresponding crystal orientation map of a randomly selected area of bulk Cu used where individual grains and grain boundaries (overlaid) can be readily identified. Refer *inset* to the right for color code. (d) Secondary electron images captured during machining process.

4.2 Deformation mechanics

The speed of relative diamond tool advancement, V was kept at 150μm/s and preset depth of cut a_0 was varied from 1μm to 5μm. Thickness of workpiece w (along z-direction in Figure 18a) is $\geq 100\mu$m, and choosing $a_0 \ll w$ essentially ensures plane-strain condition[65]. Thus, individual grains are deformed one by another along the machining direction ($y-$axis in Figure 18a) while several grains are machined simultaneously along the workpiece thickness direction ($z-$axis in Figure 18a). The rake angle α in Figure 18a was kept at a constant value of 0°. Thus, the corresponding effective strain imposed on the deformed chip can be calculated via[65]:

$$\varepsilon_{\text{eff}} = \frac{\cos\alpha}{\sqrt{3}\sin\varphi\cos(\varphi-\alpha)} = \frac{1}{\sqrt{3}\sin\varphi\cos\varphi} \tag{4.1}$$

where the shear angle φ (the angle between the ideal shear plane and $y - z$ plane in Figure 18a) is determined by the ratio of preset depth of cut a_0 and chip thickness a_c, $\tan\varphi = a_0/a_c$. At the micrometer length-scale, the ratio a_0/a_c is primarily dominated by grain orientation being deformed for given machining condition, i.e. orientation-dependent plastic flow. Figure 19 shows the variation of calculated effective strain values imposed on grains of different orientations with respect to diamond tool advancement. While the machining conditions are identical ($a_0 = 1$ or 2μm and $V = 150\mu$m/s here), the plastic strain is characteristically divergent as a function of the bulk grain orientation.

Meanwhile, as mentioned earlier in Chapter 3, the open-form deformation configuration allows for direct observation using SE imaging during *in situ* machining experiments inside the vacuum chamber of SEM. Figure 20 shows the SE images of deformation zone recorded during machining of annealed Cu with identical micromachining conditions (preset depth of cut $a_0 = 3\mu$m and velocity $V = 150\mu$m/s), but for four different grains of which orientations are illustrated by the *inset* lattice unit cells with respect to machining direction. It can clearly be seen that the material flow from bulk grain through deformation zone to deformed chips changes from one grain to another, i.e. orientation-dependent plastic flow and so do the resultant thickness of deformed chips despite of the characteristic simple shear.

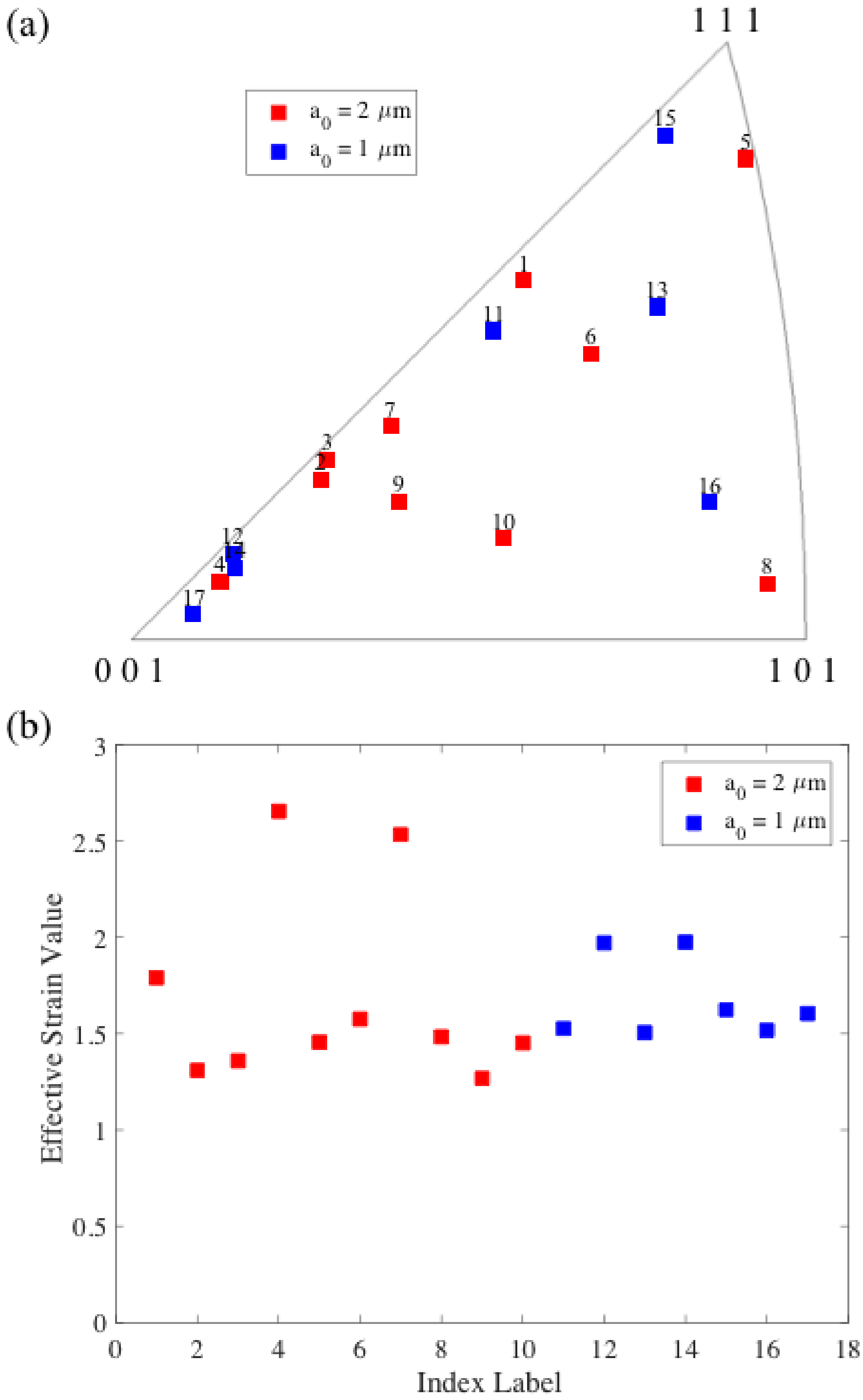

Figure 19: (a) The inverse pole figure showing the orientations of bulk grain. (b) The calculated effective strain values corresponding to grains in (a) using Eq.4.1.

Note that the characteristic sinuous flow in machining copper at the meso-scale can be modified via modulating the free surface of workpiece before machining, such as an inclusion of prehardening layer as shown in Ref.[78] which results in dramatical change of chip morphology. As for experiments in this chapter, the following strategy has been utilized to avoid the aforementioned effect: before every actual cut with preset depth of cut a_0 (the one used for data collection and analysis of deformation mechanics and microstructure evolution), at least one cleaning cut with $\leq 1/2a_0$ is executed (typically $a_0 = 0.5\mu$m is chosen for cleaning cut).

The quantitative analysis of material flow through the deformation zone was performed via digital image correlation (DIC) on sequential second electron images[9, 10, 44]. Given plan-strain deformation condition in this machining configuration, this examination only focuses on strains in the $x - y$ plane (refer to Figure 18a). As pointed earlier, a sequence of SE images of the "stationary" deformation zone (with respect to electron beam) can be recorded for designated grain orientations during *in situ* micromachining experiments. The asperities on the surface resulting from aforementioned chemical etching offers spatial contrast for feature tracking in image correlation algorithms to characterize the displacement field in the deformation zone. Subsequently, the two-dimensional discrete cross correlation for consecutive image pairs captured is:

$$\Phi_i\left(m,n\right) = \sum_{i=1}^{p}\sum_{j=1}^{q} f_i\left(x,y\right) \times f_{i+1}\left(x+m, y+n\right) \tag{4.2}$$

where $f\left(x,y\right)$ is the intensity at selected position (x,y) in the image with dimension $p \times q$ after normalization. For a given point $\mathbf{P} = (x,y)$ in ith image, its corresponding position $\hat{\mathbf{P}} = (x+m^\star, y+n^\star)$ in the $(i+1)$th image is estimated by calculating the maximum value in cross correlation function $\Phi_i\left(m,n\right)$.

The resultant displacement field $\mathbf{D}$ can be constructed via running the above calculations for designated grids on selected areas in each consecutive pair of SE image sequence, which contains two components, one due to workpiece movement (rigid body motion) $\mathbf{D}_m = \begin{bmatrix} u_m \\ v_m \end{bmatrix}$ and the other related to shear deformation $\mathbf{D}_p = \begin{bmatrix} u_p \\ v_p \end{bmatrix}$. (Here u and

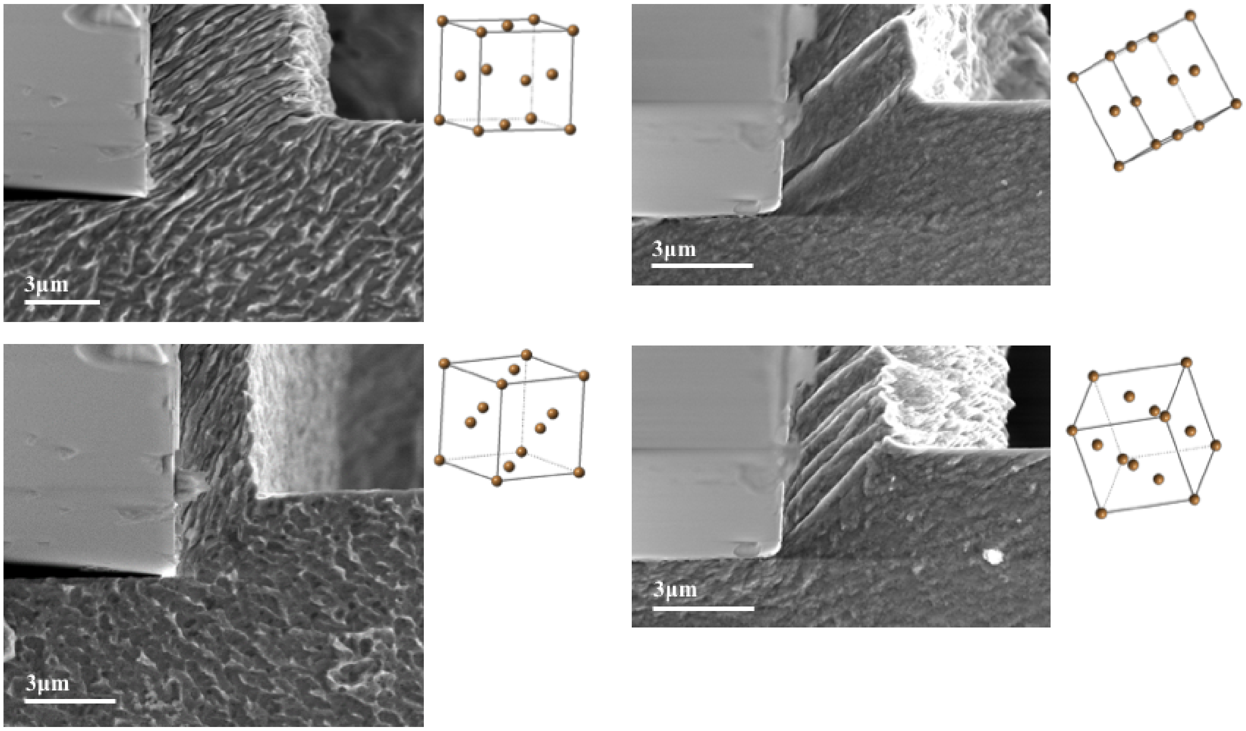

Figure 20: Secondary electron images captured during machining process with preset depth of cut $a_0 = 3\mu$m and cutting velocity $V = 150\mu$m/s with *inset* illustrating crystal lattice with respect to the direction of tool advancing respectively.

v are displacement functions in x and y directions as shown in Figure 18a, respectively.) Subsequently, the corresponding strain rate tensor is given by taking spatial and temporal differentiation of the displacement field:

$$\frac{\partial \mathbf{D}_p}{\partial s \partial t} = \begin{bmatrix} \frac{\partial^2 u_p}{\partial x \partial t} & \frac{1}{2}\left(\frac{\partial^2 u_p}{\partial y \partial t} + \frac{\partial^2 v_p}{\partial x \partial t}\right) \\ \frac{1}{2}\left(\frac{\partial^2 u_p}{\partial y \partial t} + \frac{\partial^2 v_p}{\partial x \partial t}\right) & \frac{\partial^2 v_p}{\partial y \partial t} \end{bmatrix} \tag{4.3}$$

In this work, the effective strain rate tensor was calculated by taking the square root of inner product

$$\dot{\varepsilon_p} = \sqrt{\frac{2}{3}\left\langle \frac{\partial \mathbf{D}_p}{\partial s \partial t}, \frac{\partial \mathbf{D}_p}{\partial s \partial t} \right\rangle} \tag{4.4}$$

This orientation-dependent deformation heterogeneity is also reflected in the strain rate fields. Figure 21 shows the characterization of material flow through deformation zone during *in situ* machining experiments. Figure 21a and c show sequences of SE images of two grains captured during machining with $a_0 = 3\mu$m and $V = 150\mu$m/s where the grain orientations with respect to tool direction are illustrated by the *inset*. The highly localized strain rate fields coincide with the assumption that severe plastic deformation is imposed in highly confined zone. Despite of great similarity between these two strain-rate fields, obvious distinction can still be made in terms of strain field geometry. It should be emphasized here that this distinction purely results from the grain orientation variation and its wide prevalence will be shown in the following content. In the configuration of plain strain machining, the bulk material is deformed by the advancing diamond tool in an increasing manner, i.e. layer by layer sequentially through confined deformation zone as shown in Figure 22. Despite of small value of t_D when reducing preset depth of cut a_0 down to the micrometer length scale, the strain field within this tiny deformation zone is still highly inhomogeneous. Apparently, the strain increases from 0 to its maximum value when moving perpendicular to the shear plan (i.e., $-y' \rightarrow +y'$) from bulk grain (pristine state) to deformed chip (saturated state) as shown in Figure 22b. Meanwhile, the strain gradient along the shear plane (i.e., parallel to $+x'$) cannot be ignored. Consider one layer of material parallel to the ideal shear

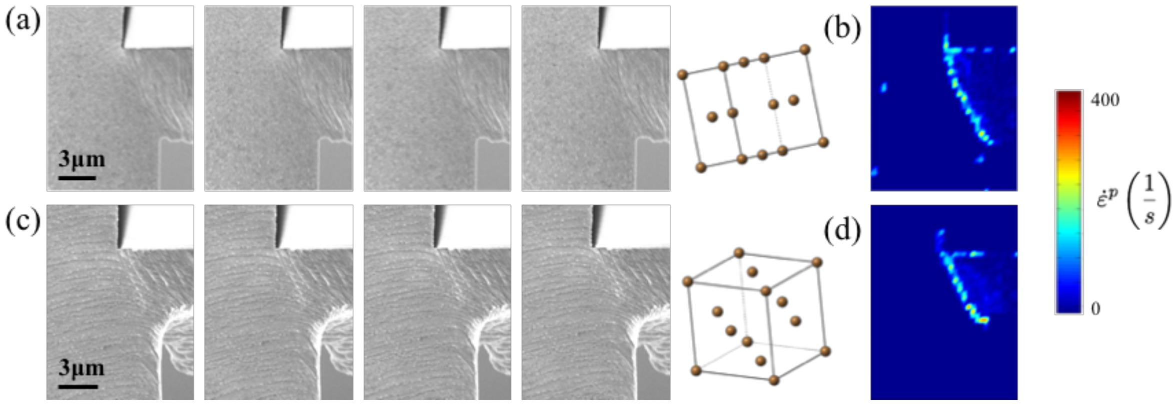

Figure 21: Sequential SE images of the deformation zone for performing DIC captured during *in situ* machining experiment with preset depth of cut $a_0 = 3\mu$m and cutting velocity $V = 150\mu$m/s of two grains (a) and (c), with *inset* illustrating crystal lattice with respect to the direction of tool advancing. (b) and (d) Strain rate field obtained from DIC corresponding to (a) and (c) respectively.

plane as in Figure 22c, the left-hand end is the free surface of the chip which can only possess a strain value of 0, while the right-hand end is strictly constrained by the diamond tool tip.

4.3 Microstructure characterization

4.3.1 Temperature rise

Most of the work expended in plastic deformation is released as heat (over 90%). The generated heat may not be fully dissipated by the workpiece especially in deformation with large strain rates. Thus, machining is a thermo-mechanical deformation process where corresponding microstructure evolution can be further altered by thermal effects. Ref.[66] examined temperature rise with different machining conditions at the large scale ($\sim 100\mu$m), which was measured by infrared camera. However, the deformation configuration in this work makes it quite difficult to perform direct thermometry over the deformation zone (given the

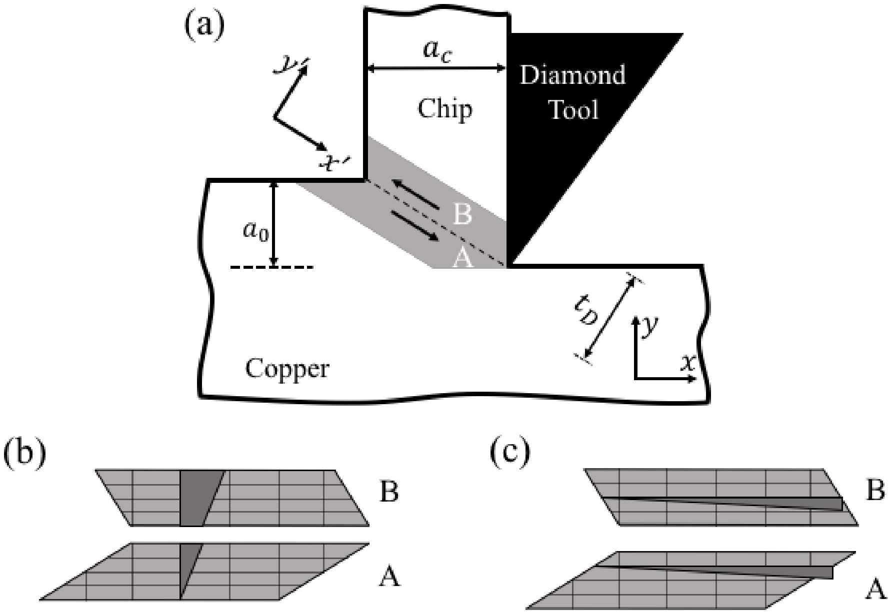

Figure 22: (a) A schematic representation of simple shear deformation during machining. An Element A is sheared in an idealized plane into element B as it forms the chip. Illustration of strain gradients both perpendicular (b) and parallel (c) to the shear plane.

spatial confinement) during *in situ* micromachining experiments, a theoretical estimate of the temperature rise would be valuable to evaluate the heat effect. As shown above, the plastic deformation concentrates in a narrow zone, which moves together with the diamond tool. Thus, heat dissipation can be modelled as a moving heat-source problem which allows for calculations using techniques akin to those in Refs. [3, 10]. Temperature increment in the deformation zone is given by

$$\rho C_p \Delta T = (1 - \beta) \cdot \tau \cdot \varepsilon \tag{4.5}$$

where $\rho = 8.96\mathrm{g/cm}^3$ and $C_p = 0.385\mathrm{J/(g \cdot K)}$ are density and specific heat capacity of Cu. The fraction of heat dissipated away into the bulk is

$$\beta = \frac{1}{\alpha} erf\sqrt{\alpha} + (1+\alpha)\, erfc\sqrt{\alpha} - \frac{e^{-\alpha}}{\sqrt{\pi}} \left(\frac{1}{2\sqrt{\alpha}} + \sqrt{\alpha} \right) \tag{4.6}$$

where

$$\alpha = \frac{1}{4} \left(V \cdot a_0 \tan\varphi \right) \cdot \kappa \tag{4.7}$$

and $\kappa = 1.11 \times 10^{-4}\mathrm{m}^2/\mathrm{s}$ is the thermal diffusivity. Following this calculation, the estimated temperature rise (only for order-of-magnitude approximation) for machining conditions explored in this work was found to be below 10K. Choices of machining parameters in this work ensure isothermal deformation.

4.3.2 Microstructure evolution across the deformation zone

Progressive material flow during micromachining results in evolutions in microstructural characteristics, which arises from purely mechanical effects. The trajectory of microstructure evolution from bulk grain to severely deformed chips across deformation zone is retained in partially detached specimens as in Figure 18a. These specimens with multiple partially detached chips were mounted using epoxy and then polished via standard metallographic preparation procedure as described earlier in Section 4.1, which are then examined by EBSD. The mechanics of microstructure evolution can be revealed in Figure 23 from machining annealed Cu with $a_0 = 2\mu$m and $V = 150\mu$m/s. Recall that the average grain size of bulk Cu is about 100μm, this sample with partially detached chip essentially contains only a small volume from intra-granular deformation within a single crystal, away from grain boundaries (whose effects will be revealed later in this chapter). In Figure 23a, the black arrow line indicates a path with increasing strain from 0 to maximum value of $\sim$ 1.4 in this case. The dislocation density in the deformation zone increases with applied strains, and subsequently, multiplication and rearrangement of dislocations result in formations of dislocation sub-structures including incidental dislocation boundaries (IDBs, from statistically trapped dislocations) and geometrically necessary boundaries (GNBs, because of strain gradients)[32]. The misorientations of these boundaries evolve with progressive strains. This is shown in Figure 23a and c, where the misorientation value (with respect to bulk grain) increased gradually in the path from bulk grain to deformed chip from this accumulating effect and a high angle boundary (HAB) was formed when approaching the territory of chip (further deformation stops once passing the deformation zone). This microstructural variation is manifested not only in the direction perpendicular to the shear plane, but also along the shear plane due to the strain gradient as shown in Figure 22c. A HAB segment developed perpendicular to shear direction within the deformation zone as shown in Figure 23a, and the misorientation map in Figure 23d suggests that this HAB comes from that adjacent regions in the deformation zone reorient progressively along the shear direction.

The aforementioned mechanism is also assisted by dynamic recrystallization (DRX) driven by increasing dislocation density, which is manifested in the region of deformed microstructure featuring dislocation-free (or low density) domains surrounded by boundaries with high misorientation angles as can been from kernel average misorientation map (KAM, Figure 23b).

Figure 23e-h show a similar case to that in Figure 23a-d, while high angle boundary segments (almost) perpendicular to shear plane were found in the deformed chip (refer to the white arrow in Figure 23e and corresponding misorientation map in Figure 23h). At macroscopic machining, the thickness of deformation zone is estimated conventionally where

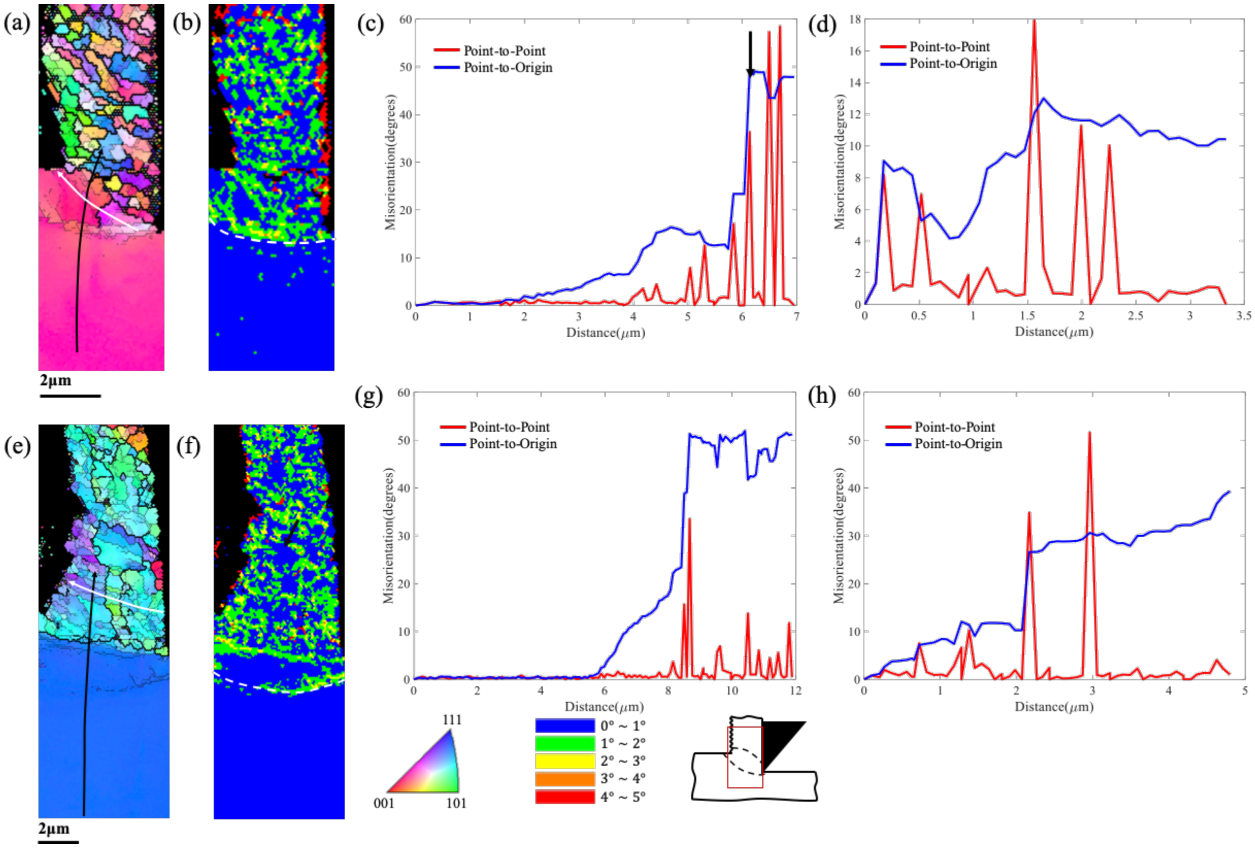

Figure 23: Crystal orientation maps (a) and (c), and corresponding kernel average misorientation maps (b) and (d) of two specimens with partially detached chips to illustrate the microstructure evolution during the micromachining. Misorientation maps (e) along the path by white arrow and (f) by black arrow calculated from the crystal orientation map (a). (g) of white arrow and (h) of black arrow correspond to (c). Machining condition: $a_0 = 3\mu$m and $V = 150\mu$m/s. In the crystal orientation map: boundaries with misorientation larger than 15° are represented by thicker lines and those with misorientation between 2° and 15° by thinner lines.

$t_D \approx a_0/(10 \sin \varphi)$[50]. However, the thickness of deformation zone in the machining at the micrometer length-scale here extends much further than that when referring to microstructural change.

4.3.3 Microstructure in deformed chips

In the configuration of plane strain machining, severe plastic deformation is imposed continuously as the material progresses from the bulk grain through deformation zone into deformed chips. Thus, accompanying the aforementioned variations in characteristics of material flow, microstructural consequences would also be expected to depend on the bulk grain orientations, i.e., orientation-dependent microstructure evolution. As shown in Figure 24, microstructure in deformed chips spans the entire gamut from complete lack of grain refinement to the generation of an ultrafine structure (characteristic in sever plastic deformation at macroscopic scale). Formation of ultrafine grained microstructures in deformed chip from some bulk orientations is observed consistent with SPD at larger length scales, while others show lack of refinement. At small length scales, both the gradients along and perpendicular to shear direction provide driving forces for microstructure evolution, resulting in the microstructural heterogeneity within deformed chips and among those from different bulk grains.

Plastic deformation of crystalline metals is accommodated via dislocation multiplication, annihilation, rearrangement[48]. Motion of dislocations is confined to slip systems, of which mobility and glide are fundamentally determined by the lattice structure and determines the plastic response in turn[76]. A slip system is activated when the applied stress τ is larger than its corresponding critical resolved shear stress τ_{CRSS}. The resolved stress components on each slip system are determined by the alignment of crystal lattice with respect to external stresses. In face-centered cubic (FCC) copper, there are 12 independent slip systems available as shown in Figure 25b. Following Taylor's criterion, at least five independent slip systems are required for arbitrary shape change[72]. Thus, not all 12 slip systems need to be operative to accommodate plastic deformation. On one hand, the resolved stress components on each slip system vary with bulk grain orientation since grain orientation determines alignments

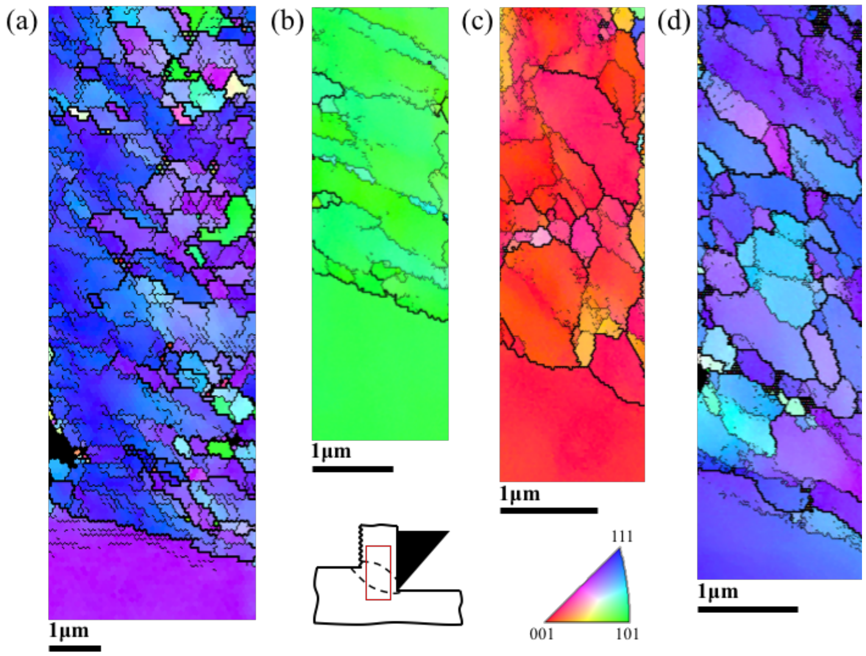

Figure 24: Crystal orientation maps obtained by EBSD of different grains. Machining condition: $a_0 = 2\mu$m for (a), $a_0 = 1\mu$m for (b)-(d) and $V = 150\mu$m/s. In the crystal orientation map: boundaries with misorientation larger than 15° are represented by thicker lines and those with misorientation between 2° and 15° by thinner lines.

of crystal lattice with respect to applied stresses. Figure 25 illustrates the slip systems with largest Schmid factor for each grain under shear direction $(\bar{1}10)$ in a typical polycrystalline Cu sample in our experiments. On the other hand, the abundance of equivalent slip systems in FCC Cu could also introduces inherent stochasticity, where various sets of slips with equivalent or similar critical resolved shear stress can lead to same strain level. The set of active slip systems during plastic deformation depends on bulk the grain orientations. Under severe plastic deformation which involves prolific cross-slip here, plastic response does not necessarily homogenize at large strains.

In Ref.[32], Hughes and Hansen performed quantitative analysis on the microstructure of pure polycrystalline nickel undergone cold rolling with reductions from 70 to 98%. It has been shown that the averaged spacing of both IDBs and GNBs decreases with increasing applied strains in Figure 26. Based on these statistical observations of dislocation structures, Basu and Shankar[10] proposed a phenomenological argument that the conventional microstructure refinement is hampered when the size of the deformation zone in micromachining (defined by preset depth of cut a_0) approaches the length scales of aforementioned dislocation structures which comes from a coupled effect of spatial confinement and high strain gradients.

These averaged statistical analysis provides quite useful scaling laws which governs the microstructure formation in severe plastic deformation. However, it diminishes the role of underlying crystal orientations, i.e. orientation-dependent anisotropy is ignored. Furthermore, Ref.[9] points out that only about a quarter of samples were found to show a lack of refinement when reducing preset depth of cut a_0 down to 1μm while cutting polycrystalline pure nickel. Our results in plane strain machining of Cu at the micrometer length-scales clearly demonstrates a microstructure evolution which is strongly orientation-dependent.

During plastic deformation, the microstructural evolution comes from storage and annihilation of dislocations. Kocks and Mecking proposed the following law modeling the evolution of dislocation density with strains[38]:

$$\frac{d\rho}{d\varepsilon} = \frac{1}{b}\left(k_1\sqrt{\rho_s} - k_2\rho_s\right) \tag{4.8}$$

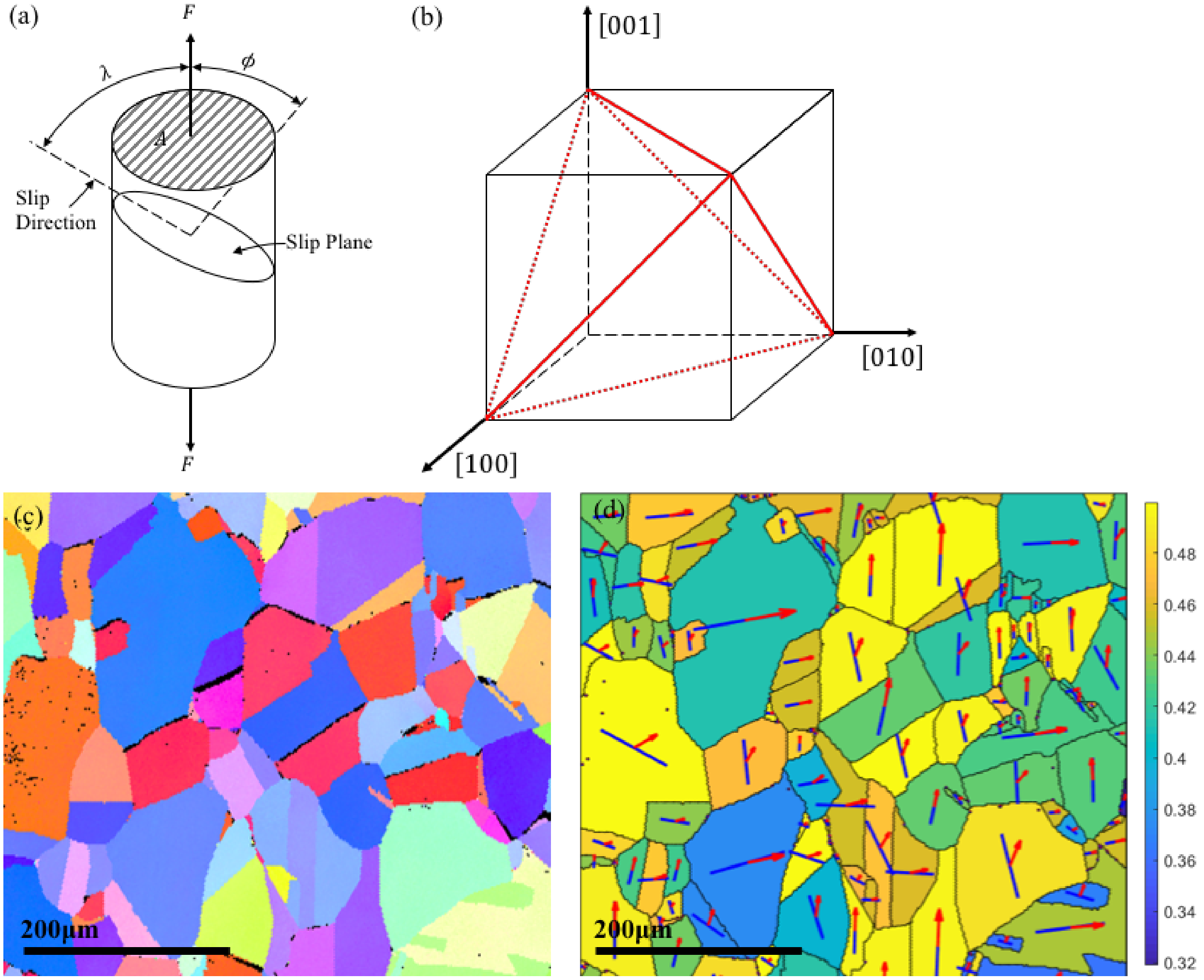

Figure 25: (a) Schematic diagram of slip plane and slip direction. (b) Thompson's Tetrahedron showing all slip planes, directions and partials in FCC structure. Triangles are slip planes: $\{111\}$; Edges are slip directions: $< 110 >$. (c) Crystal orientation map showing the microstructure of a typical copper sample in our experiment. (d) Traces of slip planes and slip directions with maximum calculated Schmid factor in each grain under shear direction $(\bar{1}10)$ corresponding to the microstructure in (c).

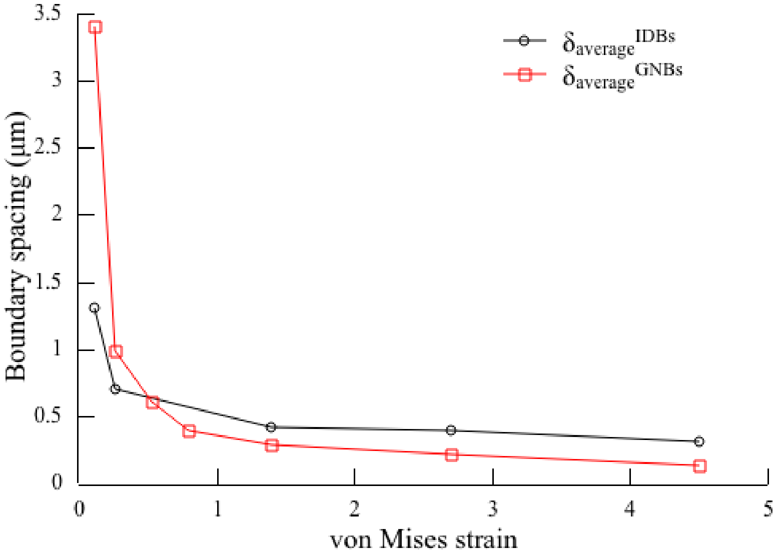

Figure 26: Variation in spacing of geometrically necessary boundaries and incidental dislocation boundaries as a function of strain in cold rolling of pure polycrystalline nickel. (Image reproduced with permission from Ref.[32].)

where the first term $k_1\sqrt{\rho_s}$ accounts for the rate at which the mobile dislocations are stored and the second term $k_2\rho_s$ represents the annihilation rate corresponding to dynamic recovery. As for the plane-strain deformation configuration applied by machining in this work, another component, strain gradient (refer to Figure 22), must also be taken into account:

$$\frac{d\rho}{d\varepsilon} = \frac{1}{b}\left(k_1\sqrt{\rho_s} - k_2\rho_s + k_3\rho_g\right) \tag{4.9}$$

where the third term $k_3\rho_g$ represents the influence of geometrically necessary dislocations (GNDs). The deformation configuration of plane-strain machining utilized in this work inevitably introduce a strain gradient ($\frac{d\varepsilon}{ds}$) in the deformation volume, the presence of which requires generation of GNDs to account for deformation compatibility. The density of GNDs, ρ_g, is proportional to the strain gradient[7]: $\rho_g \sim \frac{1}{b}\frac{d\varepsilon}{ds}$.

The onset of stage III deformation is determined by a critical stress τ_{III}, which depends on the crystal orientation at room temperature. In this stage, annihilation by cross-slip occurs when two screw dislocations of opposite signs meet each other. The rate of annihilation is defined by a critical annihilation distance y^{hkl} based on the mean free length L^{hkl} via

$$y^{\text{hkl}} = \frac{1}{\rho_s L^{\text{hkl}}} \tag{4.10}$$

and following discussions in Refs. [40] and [41],

$$y^{\text{hkl}} \tau_{\text{III}}^{\text{hkl}} \propto C\mu b \tag{4.11}$$

where C is a constant, μ is shear modulus and b is Burgers vector. So a small value of τ_{III} will yield a large critical annihilation distance, which means two screw dislocations of opposite sign can annihilate over a large distance.

The storage of dislocations results from trapping mobile dislocations by obstacles (such as existent dislocations, boundaries), so the storage rate is[40]

$$\frac{1}{bL^{\text{hkl}}} = \frac{K^{\text{hkl}}}{\sqrt{\bar{a}\rho_s}} \tag{4.12}$$

where $\sqrt{\bar{a}}$ defines the average strength of the interaction between two slip systems involved and K^{hkl} is an orientation-dependent coefficient. Furthermore, as shown in Figure 19 both the effective strain values and the extension of deformation zone vary with crystal orientation being deformed, which means that the accumulation of GNDs from embedded strain gradient is also orientation-dependent, i.e. $k_3 \rightarrow k_3^{\text{hkl}}$. Lumping all the information above, Eq.4.9 becomes

$$\frac{d\rho}{d\varepsilon} = \frac{1}{b}\left(\frac{\sqrt{\bar{a}\rho_s}}{K^{\text{hkl}}} - y^{\text{hkl}}\rho_s + k_3^{hkl}\rho_g\right) \tag{4.13}$$

which implies that the dislocation accumulation is enhanced with the embedded strain gradient in plane strain machining and depends on the crystal orientation.

The driving force for continuous dynamic recrystallization (CDRX) which is responsible for grain refinement comes from the storage of dislocation in plastic deformation. Thus, lack of refinement comes from lack in dislocation density. From Eq. 4.13, it can be seen that the increase in dislocation density $d\rho$ with respect to incremental strain $d\varepsilon$ can be suppressed if the underlying crystal has large critical annihilation distance y^{hkl}, equivalently small τ_{III}^{hkl}.

As shown in Figure 2a, τ_{III} is measured as the resolved shear stress on the primary slip plane in tension/compression test. Subsequently, the variation in τ_{III} with respect to orientation refers to the change in loading direction (crystal orientation when viewing along loading direction). However, in the current research work, the crystal orientation of underlying grain being cut is defined in the $x-y$ plane as shown in Figure 18a. Thus, before referring to literatures for the orientation-dependence of τ_{III}^{hkl}, it is necessary to perform rotation on the current orientation map to a new representation as viewing along the tool indenting direction which is equivalent to the loading direction in tension test. So the orientation representation differs from the discussion above and also the following. In previous discussion, the term "lack of refinement" is rather descriptive. A working definition for "lack of refinement" is the average grain size in deformed chips $\bar{\delta}_{15^\circ}$ is larger than 50% of preset depth of cut a_0, i.e. $\bar{\delta}_{15^\circ} \geq a_0$. This comes from the fact that the average grain size in a characteristically refined chip as shown in Figure 23a is $\sim 0.5\mu$m, about a quarter of preset depth of cut a_0 used, and this criterion doesn't have physical base.

Figure 27a summarizes the microstructure characteristics (refinement or lack of refinement) with respect to tool indenting direction in inverse pole figure. When comparing Figure 27a and b, it can be seen that the crystal orientations which feature lack of refinement after severe shear deformation correspond to the ones with low τ_{III}. A low τ_{III} means a large critical annihilation length of screw dislocations y^{hkl} which leads to rampant dynamic recovery. Furthermore, Eq.4.13 is given in a differential configuration. If taking integral on both side,

$$\rho_{\text{tot}} = \int_0^{\varepsilon} \frac{1}{b}\left(\frac{\sqrt{\bar{a}\rho_s}}{K^{\text{hkl}}} - y^{\text{hkl}}\rho_s + k_3^{hkl}\rho_g\right) d\varepsilon \tag{4.14}$$

the dislocation density will also vary with the applied strain level. Referring back in Figure 22c, a strain gradient exists along the shear direction, which also leads to a gradient in attained density of dislocations. With such variation, Figure 24a exhibits a gradient of microstructure: the right-hand side features recrystallized grains corresponding to a high strain level while the left-hand side is decorated by LABs.

The lack in dislocation density necessitates the decrease in formation of dislocation substructures and subsequently the reorientation is also suppressed across a confined deformation volume as in Figure 24b. Correspondingly, the grain boundary misorientation distribution has very little fraction of boundaries with very high misorientations as in Figure 28d. This is also manifested in Figure 24a, where insufficient reorientation results in domains surrounded by a mixture of LABs and HABs in deformed chips, resulting in a noticeable fraction of boundaries with moderate misorientations in Figure 28c. However, this effect is less pronounced at larger length scales, as the size of dislocation substructures becomes significantly smaller than the thickness of deformation zone. The increase of accumulated dislocation inevitably increases the possibility of formation of substructures as in Figure 23a, and also elevates the driving force for DRX, so the deformed chip has a characteristic ultrafine grained microstructure with a large portion of HABs as in corresponding Figure 28a. Example in Figure 24c falls in the mediate scenario where the grain boundary misorientation distributions have a mixed feature of fractures with both low and high values. Meanwhile, as pointed out earlier, the strain gradient along the shear direction cannot be ignored, i.e., strain increases from the free surface to the region close to diamond tool. This gradient is mainly responsible for the microstructural inhomogeneity along the shear direction where the left part has high density of LABs and small grains with very low orientation variation are formed in the right part of deformed chip, as shown in Figure 24a.

When deforming microcrystals, the stress-strain curve often exhibits strain bursts, i.e. jumps in the curve, due to internal dislocation avalanches which results in large scattering in mechanical responses. In Ref.[18], Csikor *et al* demonstrated the stochastic nature of dislocation avalanches, which follows a general form of $P(s) = Cs^{-\tau} \exp\left[-\left(s/s_0\right)^2\right]$, and it explains the large scattering in the response of microcrystals during mechanical loading. Although the strain bursts decrease with increasing size of deformed sample, the fundamental mechanism is still stochastic in nature (as confirmed by measurement of acoustic emission avalanches[55]). In the severe plastic deformation applied by plane strain machining which

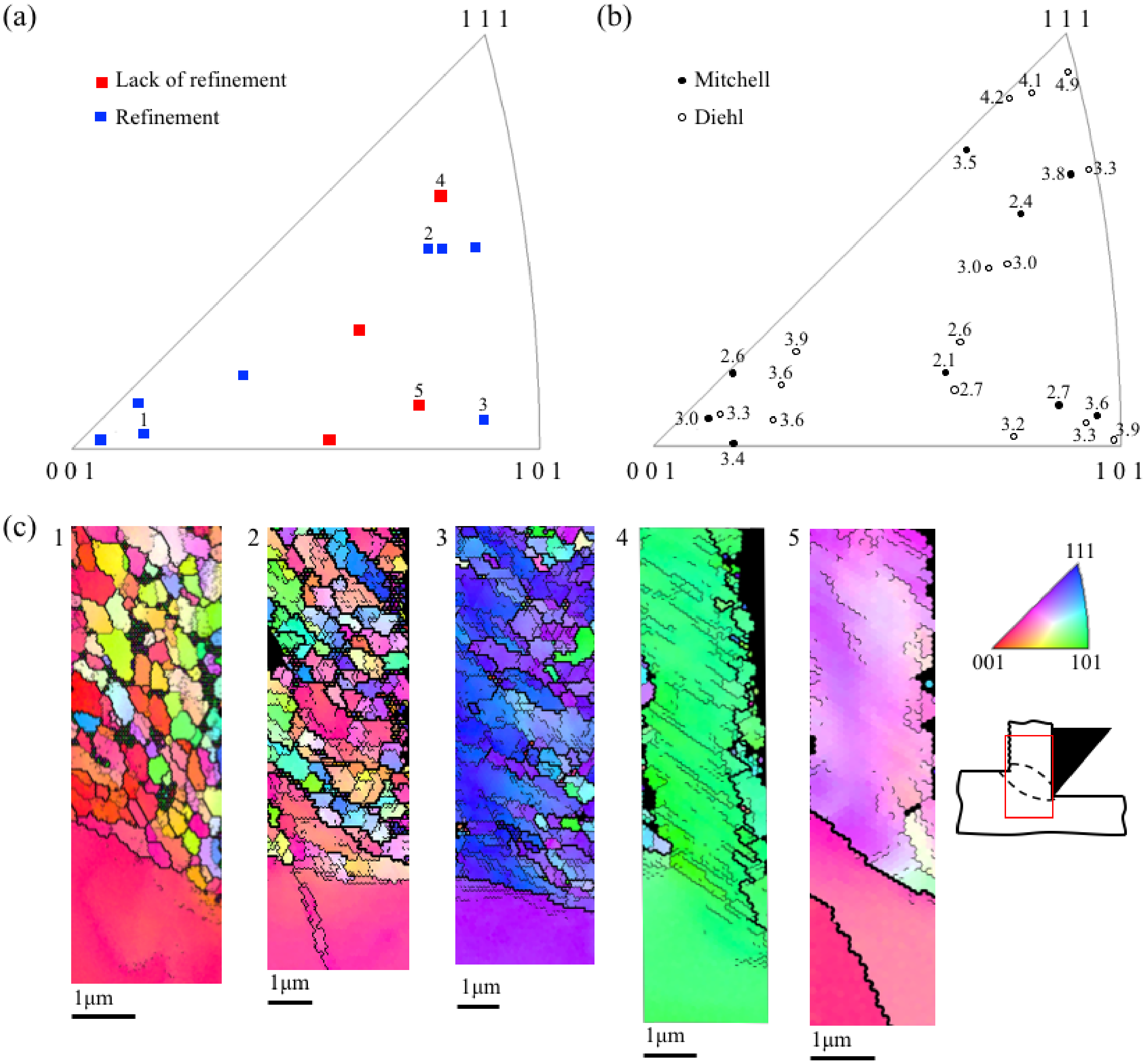

Figure 27: (a) Summary of microstructure characteristics (refinement or lack of refinement) with respect to tool indenting direction. (b) τ_{III} of Cu with respect to loading direction (after Mitchell and Diehl[45]). (c) Microstructure evolution of selected orientations as indicated in (a).

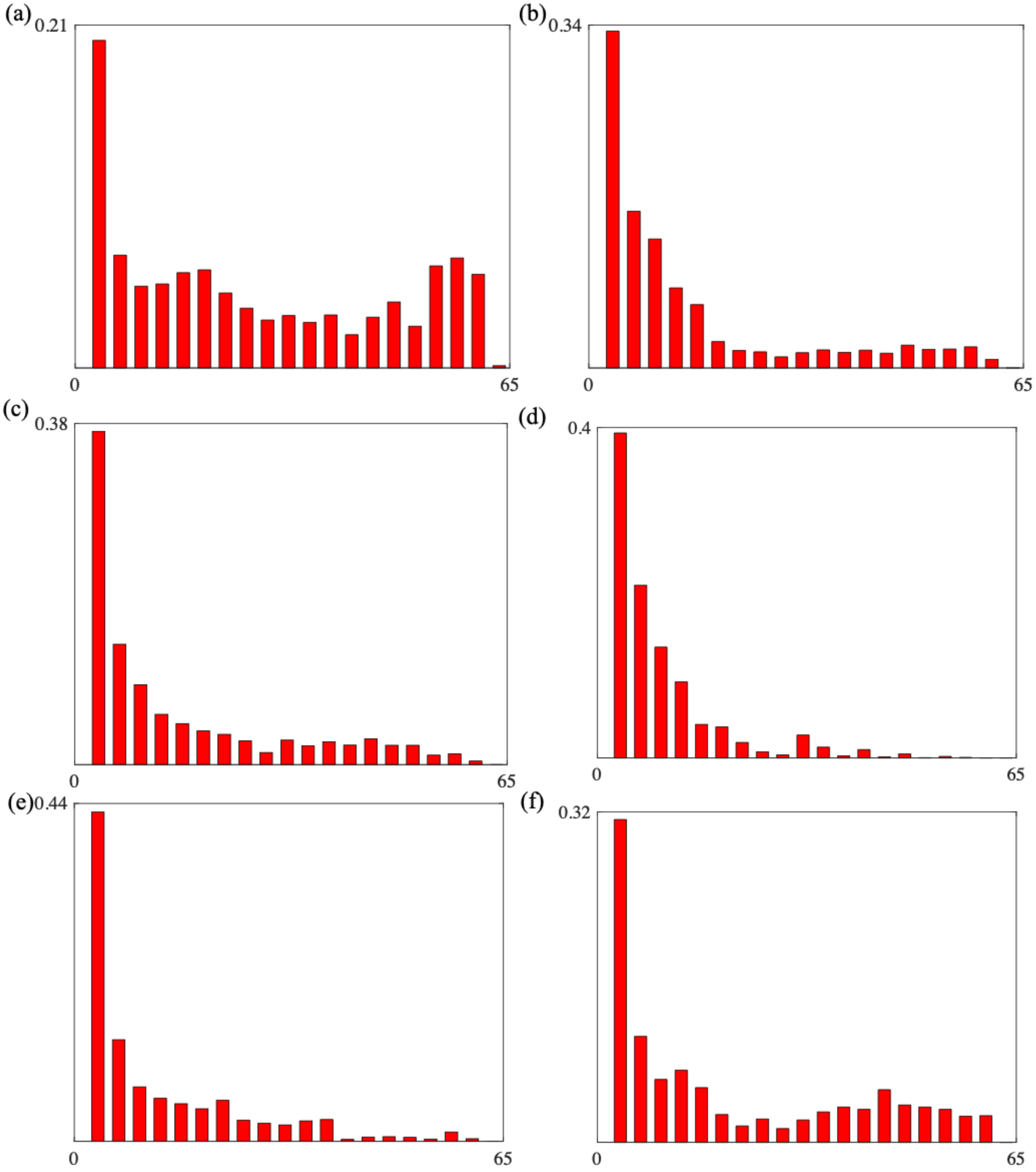

Figure 28: Grain boundary misorientation distributions obtained from chips (a) in Figure 23(a), (b) in Figure 23(b), (c) in Figure 24(a), (d) in Figure 24(b), (e) in Figure 24(c), (f) in Figure 24(d).

involves prolific cross-slip, the following question comes up: is the microstructural response deterministic or stochastic? Here, we present a brief examination to show that the microstructural response is deterministic depending on the crystal orientation being deformed. The experimental setup mentioned in Section 4.1 allows us to select the grains to be deformed at our will. Figure 29a-b shows the microstructure in deformed chips corresponding to two grains with almost identical orientation which undergone the same deformation with machining condition $a_0 = 2\mu$m and $V = 150\mu$m/s but are from two different workpieces, i.e. two runs on two bulk samples. Figure 29d-g shows the corresponding grain size distribution and grain boundary misorientation distribution, which can be seen that they didn't show any significant variation. This works also for the case of lack of refinement when comparing Figure 29g and Figure 24b.

4.4 Surface integrity from micromachining

When deforming polycrystalline bulk metals, the existing networks of grain boundaries (GBs) induce additional heterogeneity in the plastic deformation response. Since GB could potentially act as obstacles for dislocation motions, large accumulation on one and/or two sides of GB without proper dislocation transmission could introduce additional local strain heterogeneity, which prevent continuous strain propagation[71]. Meanwhile, the topographical integrity of machining surface is inherited from the modification of the deformation zone and subsequent microstructure evolution due to various alignments of bulk orientations with respect to machining tool. In this section, we will explore the effect of grain boundary on micromachining process.

4.4.1 Machining across grain boundaries

Given the polycrystalline nature of workpiece used in this work, it is inevitable to encounter grain boundaries over the mm-long distance for every single machining process despite of small depth of cut a_0, in a one-by-one manner when viewing along the cutting

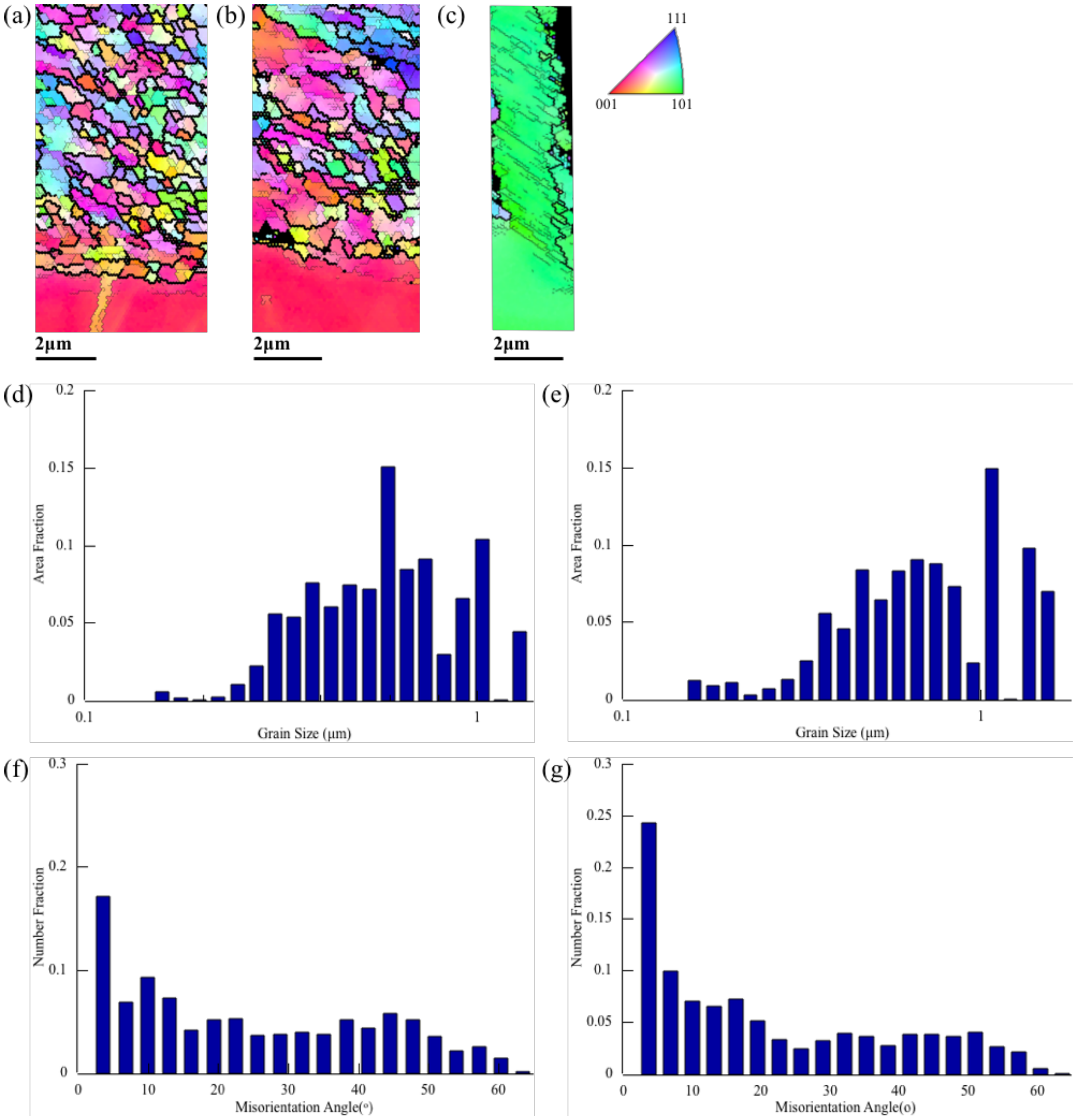

Figure 29: (a)-(c)Crystal orientation maps obtained by EBSD of different grains with machining condition: $a_0 = 2\mu$m and $V = 150\mu$m/s. Boundaries with misorientation angle larger than 15° are presented by thicker lines and those with misorientation between 2° and 15° by thinner lines. (d) Grain size distribution and (e) grain boundary misorientation distribution corresponding to (a). (f) Grain size distribution and (g) grain boundary misorientation distribution corresponding to (b).

direction, which also holds true for actual diamond turning production in industry. Meanwhile, most grains in the underlying bulk are quite large ($\sim 100\mu$m), and this fact allows us to examine the effect of grain boundary on the deformation behavior while excluding potential disturbance from neighboring boundaries. The *in situ* characterization of material flow across grain boundary is shown in Figure 30. Figure 30a shows an ideal case of deformation transition. As diamond tool approached grain boundary (illustrated by the white line in Figure 30a), the deformation in grain B was readily initiated once the deformation zone extended into B as indicated by the white arrow. Severe plastic deformation successfully passed from grain A to B without any noticeable deviation. The anisotropy in deformation behavior is shown again, which is inherently characteristic of bulk grain orientation. In this particular case, the deformed chip from grain B demonstrates a feature more akin to that of a sawtooth type chip, which is obviously different from that of grain A, a morphology from classical continuous simple shear. Refer to Figure 18c, the chip is still continuous without any cracks. More importantly, the intra-granular deformation is the same as the one in the vicinity of grain boundary. So, this vast shift in material flow doesn't necessitate a disturbance of imposition of severe plastic deformation across multiple grains.

Although the orientation-dependent plastic flow is quite prevalent in polycrystalline workpiece, the above smooth deformation transition across grain boundary is not always guaranteed. As shown in Figure 30b, the material ahead of diamond tool in grain C moved along the grain boundary. However, there was no sign of activation of shear deformation in grain D even though the diamond wedge was advanced right at the grain boundary, leading to a formation of notch in the deformed chip as shown in Figure 30b-9. At the initial stage of deforming grain D, the material ahead of diamond cutting tool moved as a hardened block instead of continuous simple shear. Meanwhile, the imposed SPD also resulted in side flow of material since there was no constraint to the side surface of workpiece, and the sideward burr formed in the process can hardly be removed via reducing the preset depth of cut a_0. Note that this side flow is not a direct result of the lack of physical constraints in the $x - y$ plane. As deformation continued further into grain D, the material flow returned back to normal shear deformation. It must be pointed out here that this deviation in deformation behavior only occurs in the immediate vicinity of selected grain boundary.

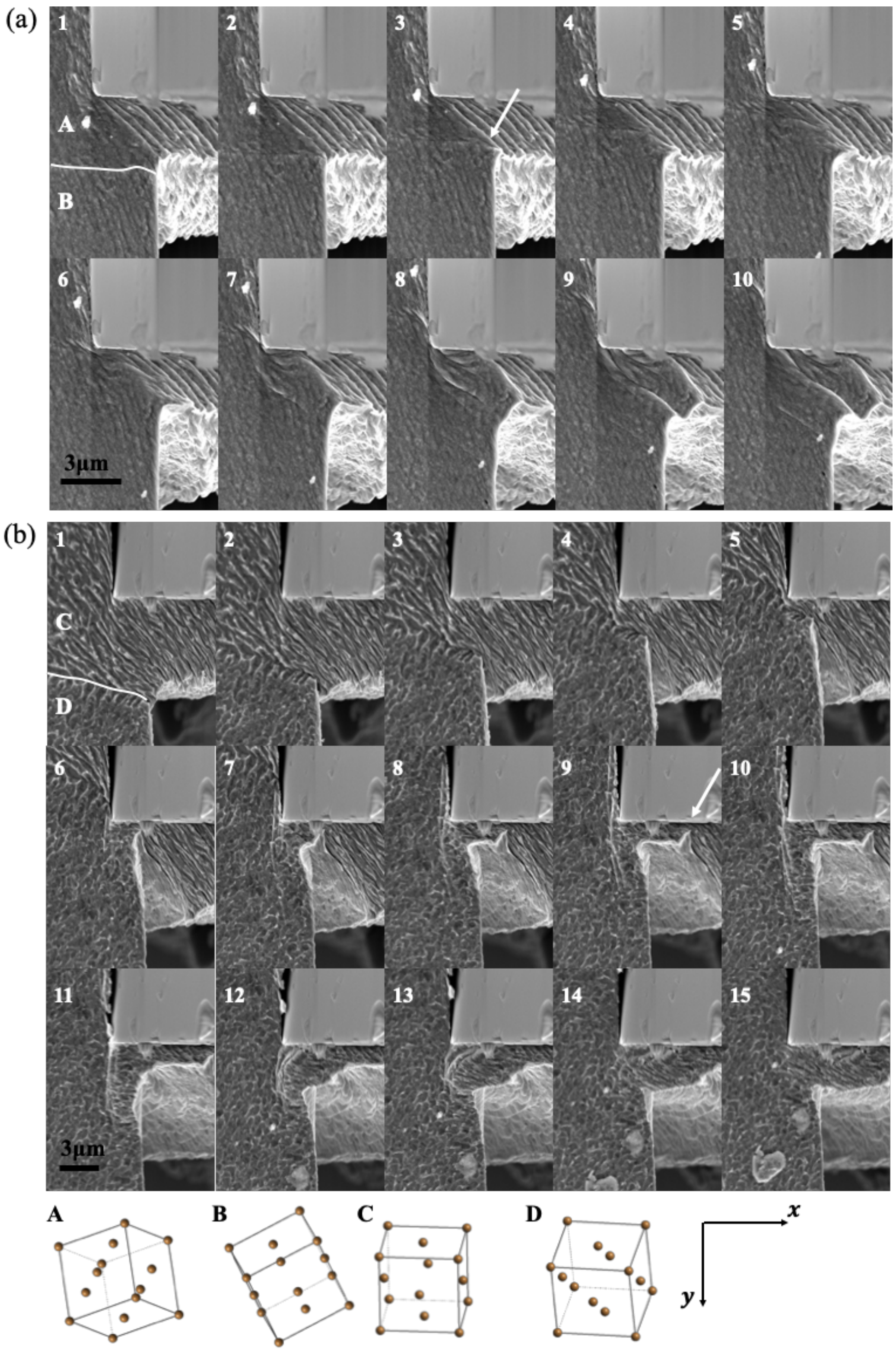

Figure 30: Sequence of SE images of the deformation zone in micromachining of annealed OFHC Cu when cutting across grain boundaries (illustrated by white line in the image) in two distinct cases (a) and (b). (*Inset*) Illustration of crystal lattice with respect to tool advancing direction. Machining condition: $a_0 = 3\mu\text{m}$ and $V = 150\mu\text{m/s}$.

During plastic deformation, grain boundaries potentially act as obstacles to dislocation motion. In the configuration imposed by plane strain machining as shown in Figure 30b, dislocations will inevitably accumulate near the grain boundary as the diamond tool approaches. Following Saada's model[60], the concentration of vacancy induced by plastic deformation due to annihilation of screw dislocation branches of the opposite signs[19] is

$$C_{\text{vacancy}} = \frac{A}{G}\int_0^{\varepsilon} \sigma d\varepsilon \qquad (4.15)$$

where A is a constant, G is the shear modulus, and ε and σ are stress and strain in the plastic deformation. Grain boundaries act as obstacles to dislocation motion in accordance to plastic deformation. In the configuration imposed by plane strain machining, dislocations will inevitably accumulate near the grain boundary as the diamond tool approaches, i.e. dislocation pile-ups. Thus, the localized dislocation pile-ups lead to an increase in vacancy concentration. Those vacancies tend to gather around deformation-induced boundaries, and such condensation results in voids formation. Subsequently, voids grow through consumption of dislocations[49]. This enhanced voids generation and coalescence result in the occurrence of ductile tearing in the vicinity of grain boundary as shown in Figure 31. Furthermore, it could result in material separating readily even far away ahead of diamond tool tip. Thus, the material to be deformed into chips will flow along the tool rake face as a "hard block" as shown in Figure 30b. Thus, the underlying material in surface would be indented by this "hard block", which causes the material side flow, or burr.

In previous experiments, we specifically choose bulk OFHC Cu containing grains with large size ($\sim 100\mu\text{m} \gg a_0$) to investigate the inherent effect of crystal orientation on deformation behavior. However, the polycrystalline nature of bulk OFHC Cu complicates the deformation process not only due to orientation-dependent anisotropy but also by the variation in grain size. On one hand, not all grains have a size much larger than a_0 as shown in Figure 18c; on the other hand, the size of grains being deformed keeps changing given that machining is a process of material removal as shown in Figure 32a. Thus, it is quite possible that the diamond cutting tool may encounter a grain with size comparable to a_0 as shown in Figure 32b. Here the deformable volume is defined by the diamond tool and grain boundary

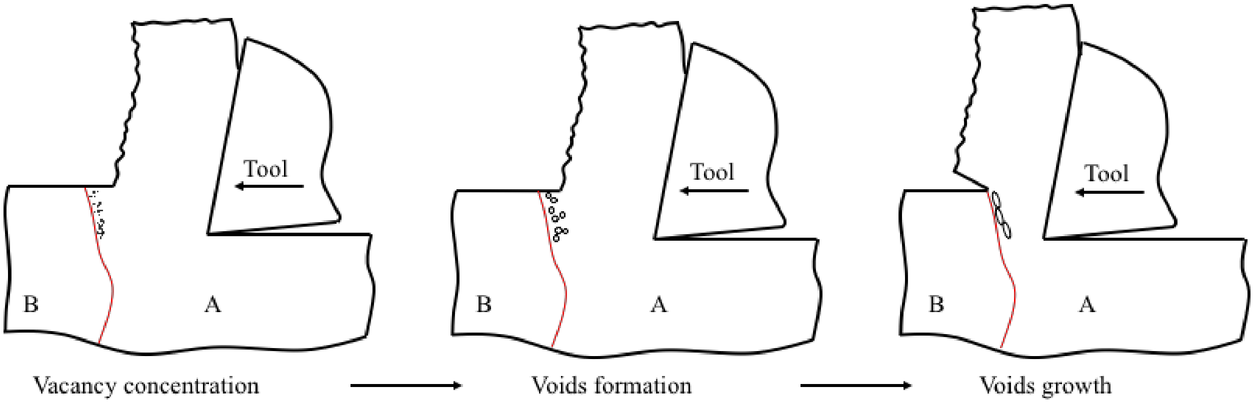

Figure 31: Illustration of ductile tearing as diamond tool approaches grain boundary.

ahead. Under such condition, the aforementioned rampant ductile tearing also occurs again in the vicinity of grain boundary.

4.4.2 Surface integrity

While bulk material is deformed by diamond cutting tool into deformed chips, fresh surface is simultaneously generated from this material removal process. The aforementioned anisotropic material response to severe plastic deformation imposed by micromachining process not only results in morphological and microstructural variation in deformed chips but also the surface integrity especially in the vicinity of grain boundary, due to the highly coupled nature of chip formation and surface generation. Our *in situ* experimental setup allows for direct one-to-one observation between deformation behavior and machining surface. (Note: grain boundaries in this section refers to general boundaries with misorientation larger than 15° if not indicated specifically.) Figure 33 shows the SEM micrographs of surface generated during machining process corresponding to Figure 30. Figure 30a demonstrates an ideal case of smooth deformation transition across grain boundary. As would be expected, the surface didn't reveal any topographical change along the grain boundary as in Figure 33a. However, this is not always the case. The grain boundary defect in Figure 33b, i.e., exceptional step-change roughness along grain boundary, resulted directly from the rampant

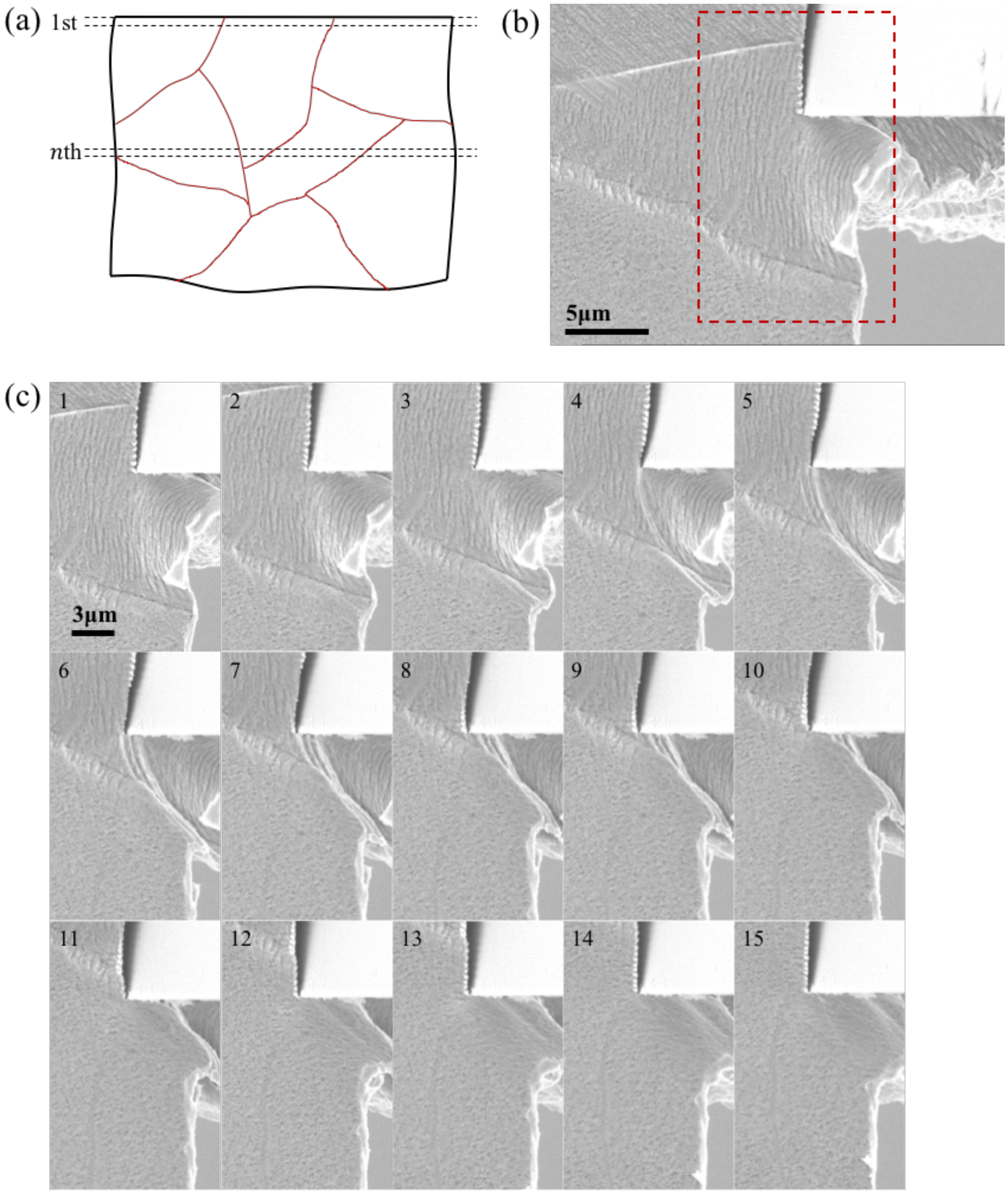

Figure 32: (a) SE image of machining a grain with comparable size to the preset depth of cut a_0. (b) Sequence of SE images of deformation zone illustrating the deviation of simple shear deformation due to reduced grain size. Machining condition: $a_0 = 3\mu$m and $V = 150\mu$m/s.

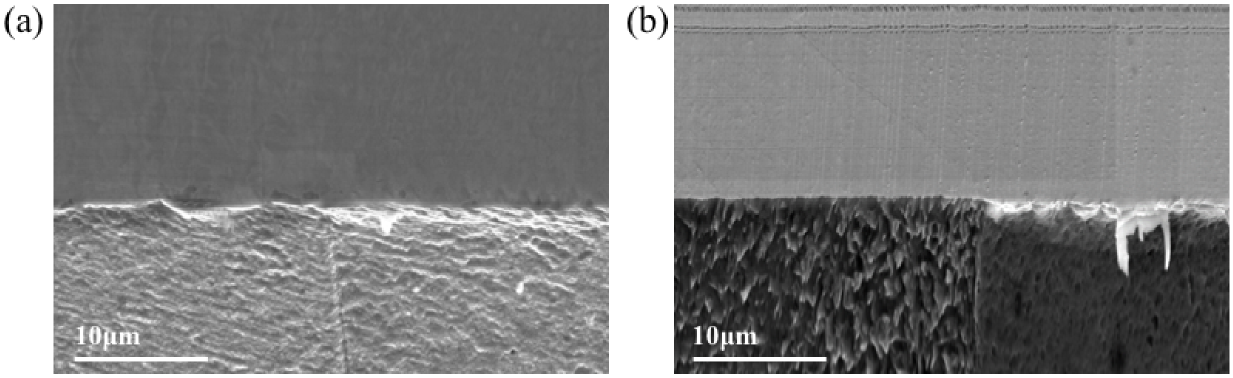

Figure 33: SE images of the surface (a) and (b) from machining identical grains as shown Figure 30(a) and (b) respectively.

ductile tearing as captured in Figure 30b. Although the aforementioned phenomena was captured near the side face (the $x-y$ plane in Figure 18 which is free of physical constraint), it must be pointed out that this grain boundary defect is definitely not related to the material side flow (as shown in Figure 30b), i.e. the formation of this topographical defect does not come from the motion of underlying grain due to compression of diamond cutting tool.

Here, we also examined the surface away from the edge area (to eliminate potential effect of side flow) under different machining conditions as shown in Figure 34. When performing *in situ* micromachining inside the vacuum chamber of SEM, it is possible to examine the microstructure of freshly generated surface via EBSD which allows for relating topographical features with underlying microstructure. As can be seen in Figure 34, the aforementioned grain boundary defect also appears in the region away from the edge, which clearly corresponds to a grain boundary as revealed in crystal orientation maps from EBSD. More importantly, although the overall intra-granular roughness of machined surface decreased with reducing a_0, the grain boundary defects persisted. Here, the interplay of the crystallographic structure with the deformation mechanics resulting in topographical defects is evident in these observations.

We examined over 50 machining samples of the defects and corresponding orientation map via EBSD with machining conditions $a_0 = 1\mu$m and $V = 150\mu$m/s and found that the

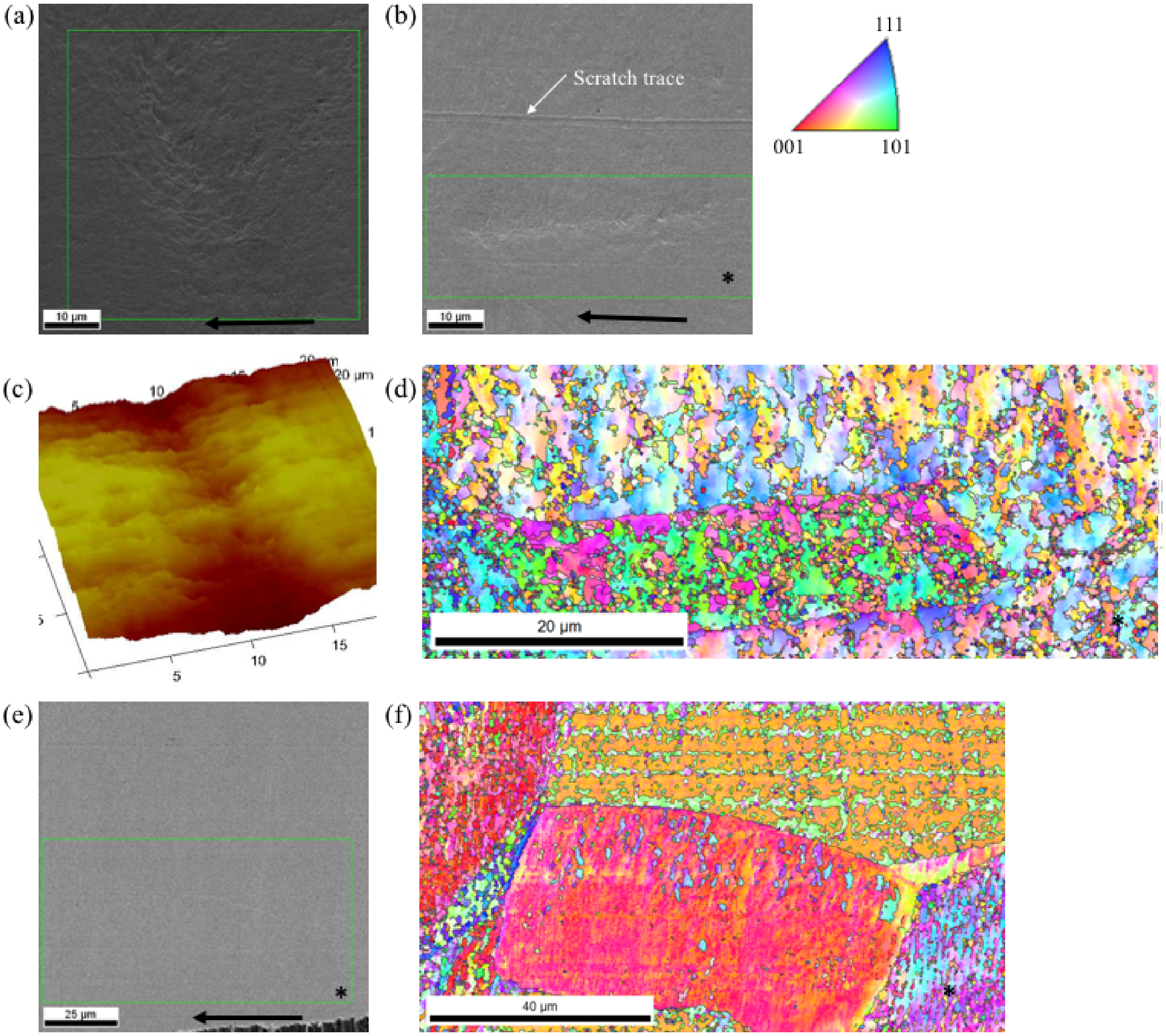

Figure 34: Secondary electron images of machined surface with grain boundary defects (outlined by green-line rectangles) under preset depth of cut (a) $a_0 = 5\mu$m, (b) $a_0 = 3\mu$m and (e) $a_0 = 1\mu$m with constant cutting velocity $V = 150\mu$m/s. The black arrows indicate the machining direction. (c) AFM measurement of the defect, (d) crystal orientation map from EBSD corresponding to the rectangular area in (a). (f) Crystal orientation map obtained by EBSD corresponding to the area in (e).

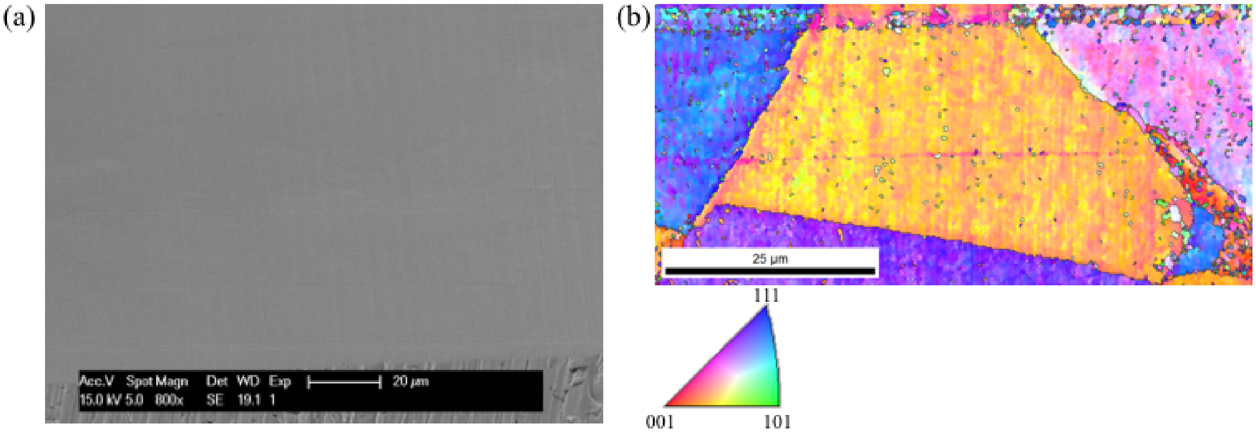

Figure 35: (a)) SE micrograph of a flat featureless area and (b) corresponding orientation map from EBSD with machining condition $a_0 = 1\mu$m and $V = 150\mu$m/s. Here, the surface is tilted slightly for better visualization of potential defects.

misorientation of grain boundaries corresponding to defects falls in the range between 30° and 55°. But this is only a rough characterization considering that the freshly generated surface also undergone deformation to some extent despite of small preset depth of cut a_0. However, we also find evidence of inherent stochasticity to the defect nucleation. Figure 35 shows the creation of flat, featureless topographies across multiple grain boundaries which also fall in the same range of misorientation. Meanwhile, step motors are used to construct the micromachining stage, and the trace of step-wise motion can still be spotted on the surface as shown in Figure 35b. This observation (along with many others not shown here) also lifts our concern that the step-wise motion doesn't trigger or assist in the formation of grain boundary defects as shown in Figure 34. Thus, it can be concluded that the modification of the deformation zone and its interaction with the crystal structure and subsequent evolution manifests the surface defects, which invariably nucleate at the interfaces between specific grain orientations.

The formation of grain boundary defect has its own inherent stochasticity given that not every single grain boundary will give rise to the defect during micromachining. Luckily, one unique case was captured and shown in Figure 36. A single high angle grain boundary was identified on the micromachined surface (as shown in Figure 36b), and only the middle part coincided with a defect but not the two ends as in Figure 36a. Figure 36c revealed the variation in the misorientation of this boundary where the defected segments featured a relatively lower value compared to that of the two ends. In this middle region, dislocation cell block boundaries were readily visible when recognizing the lamellar features (also crossing) with alternating colors near the grain boundary on both sides. When away from the grain boundaries, such dislocation cells were not observed. Noell[49] pointed out that such deformation-induced boundaries were perfect sites for voids generation. Although vacancies formation increases with increasing dislocation density, but the formation of voids via vacancy coalescence would be more like a stochastic process, which also explains the stochasticity observed in the generation of grain boundary defects on machining surface.

It would be expected that when intensifying the observations of Figures 32 and 36 the surface after micromachining features massive defects following topology of underlying grain structures. Thus, we created bulk workpiece with a microstructure featuring small grain size and also grain boundaries with large portion in the range of $30^\circ - 55^\circ$ using conventional machining process as shown in Figure 37. From Figure 37c and d, it can be seen that the grain size concentrates around 0.5μm and there is a high fraction in the "dangerous range". Here we choose the preset depth of cut to be $a_0 = 0.5\mu$m close to the average grain size. The characterization of corresponding machining surface via optical profilometer is shown in Figure 37e and f. The micromachining surface features vast amount of defects corresponding to most grain boundaries when referring back to Figure 37a and b, which is a result from our choice of bulk microstructure to deliberately promote formation of grain boundary defects in machining.

4.5 Summary

The effect of bulk grain orientation on severe plastic deformation imposed by machining annealed OFHC Cu with preset depth of cut $a_0 \leq 5\mu$m was studied. With aid of *in situ* experiments, the deformation mechanics was revealed via DIC, which highly depends on

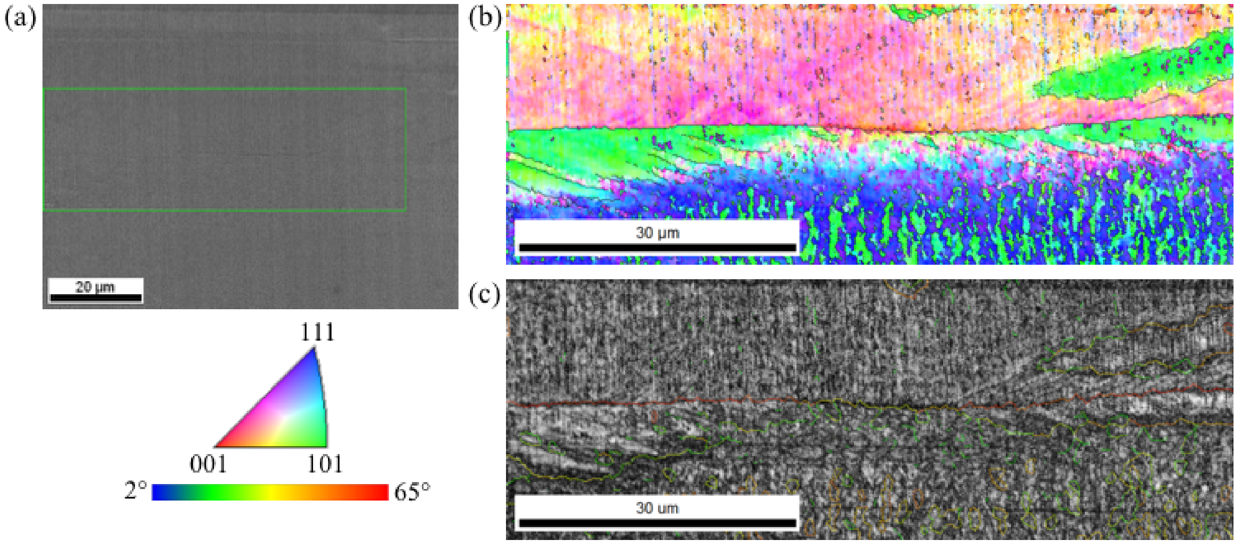

Figure 36: (a) SE image of surface with a defect in the middle area machined with $a_0 = 1\mu$m and $V = 150\mu$m/s. (b) Crystal orientation map from EBSD corresponding to the rectangular area in (a). (c) Grain boundary misorientation plot overlaid with image quality corresponding to (b).

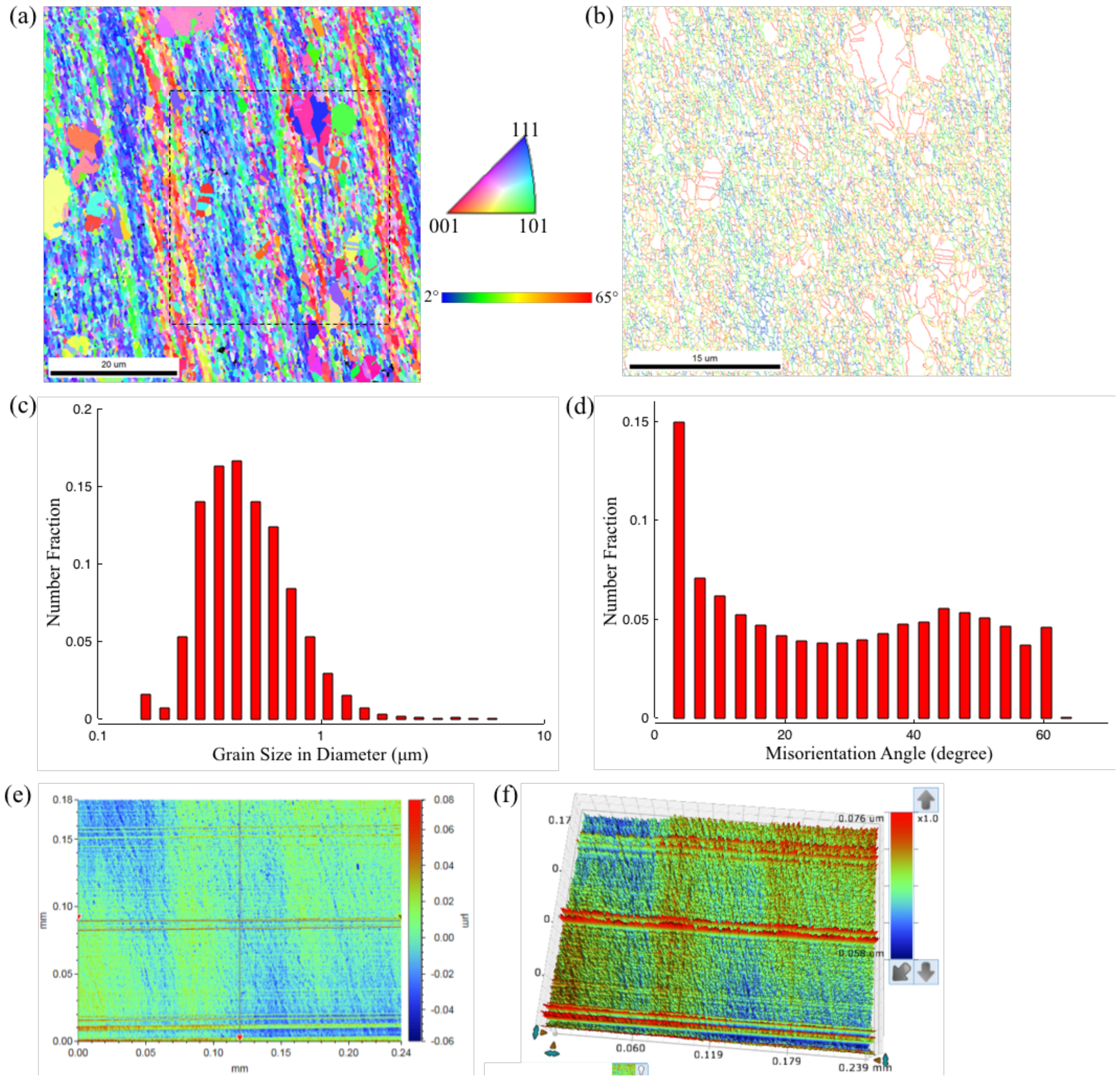

Figure 37: Engineering microstructure to tune surface integrity from micromachining. (a) Orientation map of bulk microstructure creating from conventional machining with preset depth of cut $a_0 = 200\mu$m and velocity $V = 500$mm/s. (b) Grain boundary misorientation plot corresponding to the rectangular area in (a). (c) Grain size distribution and (d) grain boundary misorientation distribution corresponding to (a). (e) 2D and (f) 3D surface topography from optical profilometer when machining the Cu workpiece with microstructure in (a) with reset depth of cut $a_0 = 0.5\mu$m and velocity $V = 150\mu$m/s.

the bulk orientation. The microstructure evolution during severe plastic deformation was characterized by performing EBSD, which is also a function of the bulk orientation spanning the gamut from ultra-fine grained structure to complete lack of refinement. This variation in microstructural response is attributed to the anisotropic accumulations of dislocations in different grains due to different alignment of grain orientation with respect to diamond tool. Due to spatial confinement at small length scales, both the strain gradients parallel and perpendicular to the shear plane contribute strongly to microstructure evolution responsible for the microstructural heterogeneity within single deformed chip and among different chips from various bulk grains. As a companion of chip formation, the integrity of surface from machining polycrystalline Cu is also related to the orientation-dependent deformation anisotropy. Observation of material flow via *in situ* experiments reveals that grain boundary defects originate from rampant ductile tearing. Examining the nucleation of grain boundary defects in conjunction with these details reveals the interplay of the crystallographic structure with the deformation mechanics, and subsequently shed lights in engineering of microstructure with textures and grain structures to tune its performance in the diamond turning process.

5.0 Length-scale Dependent Deformation Behavior of Magnesium

(*Contents form this chapter were used in other publications, proceedings and project reports.*)

Low-density Mg (density $\sim 1.74\text{g/cm}^3$) can offer expanded design opportunities for light-weighting of structural components in the automotive and aerospace sectors[36, 56], but for their poor formability and room-temperature ductility. The uniaxial symmetry of Mg, which has a hexagonal close-packed crystal structure, results in large anisotropy for the critical resolved shear stress (τ_{CRSS}) of the basal slip systems (easy, with low τ_{CRSS}) and non-basal slip systems (hard, with high τ_{CRSS}). Basal slip involves dislocations with Burgers vectors along the close-packed ($\vec{a}$) directions only. It cannot accommodate strains with components along the unique ($\vec{c}$) direction. For general plasticity of arbitrary and multi-axial strains the activation of non-basal slip, i.e. prismatic and/or pyramidal slip, is required. However, this is stymied by the high τ_{CRSS} for non-basal slip[34, 70]. Deformation twinning offers an additional pathway, which results in contraction (compression twinning) or extension (tension twinning) along ($\vec{c}$) direction. However, twinning is a polar mechanism, which is highly orientation specific, where the magnitude of accommodated plastic strain is limited [35, 79]. These inherent constraints in Mg have motivated efforts aimed at alloy design to encourage non-basal slip and/or weakening basal texture formation [69, 77, 84], microstructure engineering to augment the role of grain boundary mediated plasticity [14, 23, 83] and nanoparticle-reinforced composite designs to optimize the balance of strength and ductility [15, 68].

In this chapter, we examined the size-related deformation behavior of Mg AZ31 and pure magnesium. Here, we show that Mg can deform to large shear strains > 2 without onset of shear localization or fracture under ambient temperature conditions, when just one characteristic dimension of the deformation geometry is reduced to be in the sub-micron- or nano-scale (~ 100nm). The other dimensions can be orders-of-magnitude larger, or even macroscopic. By purposing plane-strain machining at micro/nanometer-scales as a test of material response, we demonstrate quasistatic accommodation of large (simple) shear strains in Mg. Plastic deformation-driven multiplication and reorganization of dislocation structures results in characteristic microstructure refinement, which is normally associated with nominally ductile, highly formable metals, which typically have isometric (cubic) crystal structures. Furthermore, this phenomenon is shown to be agnostic to the crystal orientation with respect to the applied deformation, which points to a broader motif for triggering a switch-over in the underlying mechanisms of plastic strain accommodation. The realization that the switch-over from brittle-to-ductile behavior in Mg is controlled by scale refinement of a single dimension of the deformation material volume implies that optimizing bulk material property combinations can be accomplished by designing composite topologies in fewer than three dimensions.

5.1 Severe plastic deformation of Mg AZ31

5.1.1 Experiments

Plane-strain machining was utilized to impose severe shear deformation as illustrated in Figure 38a. The material examined here is commercially available Mg AZ31 alloy, with composition shown in Table 2. Bulk Mg AZ31 sheet was annealed using vacuum furnace at 450°C for 3hours and then cut by diamond saw into thin pieces with approximately 10mm × 10mm and $\sim 300\mu$m wide (w in Figure 38a). To examine the underlying microstructure, the workpiece was mounted using epoxy and mechanically polished down to final step with 0.04μm colloidal silica suspension on Struers Tegramin 25. Note here, except for initial mechanical grinding, ethanol was used for lubrication and cleaning all the time instead of water. Subsequently, the sample was further cleaned via ion milling (3.5kV at 5° with 360° continuous rotation for 30min) using 1060 SEM Mill from Fischione Instruments. Orientation imaging mapping was preformed using EBSD to reveal the microstructure, as shown in Figure 38b. Here, the orientation map is overlaid with crystal lattice to illustrate the orientation of randomly selected individual grains. Despite Figure 38b shows a characteristic basal texture, the orientations of the individual grains and the direction of the nominal shear (white arrows in Figure 38a) are typically not aligned for basal slip. Thus, the observations in this work are therefore not an artifact of any preferential alignment, which can potentially enable accommodation of large strains[46]. In this work, the machining velocity V was kept at constant of 150μm/s and the preset depth of cut a_0 was varied from $\sim$ 100nm to $\sim$ 10μm. Again, the edge radius of diamond tool ($\leq$ 25nm) is much smaller than the scale of deformation volume studied in our experiments. The plane-strain deformation condition is ensured also by the fact that $a_0 \ll w$. The length of the sample over which the wedge is advanced is at the mm-scale $\gg a_0$ and the width of the sample (w) in the third dimension is $\geq$ 100μm (also $\gg a_0$), i.e., macroscopic. The choice of this deformation platform allows for selectively refining only one characteristic length-scale of the deformation geometry: preset depth of cut a_0, while simultaneously allowing for the imposition of large simple shear strains within a configuration (Figure 38a), where the material flow can be observed via *in situ* experiments.

From Figure 38b, we can see that the average grain size of bulk Mg AZ31 is around $\sim$ 30μm. When compared with preset depth of cut a_0 probed here, the chosen experiments impose plane-strain deformation only in one grain in a given increment of time, equivalent to deformation of single crystal. However, the width of the workpiece w is normally composed of multiple grains; but the strain in this direction is negligible (due to plane-strain in $x-y$). Thus, the deformation in such configuration can be abstracted in the following manner: an undeformed bulk material undergoes simple shear with a characteristic length scale defined by preset depth of cut a_0, which we choose to refine at will to examine the size-related behavior in the regime of severe plastic deformation. Subsequently, we will demonstrate that the length-scale dependent switch-over in the deformation behavior is not only agnostic to the orientation of shear with respect to the crystal axis (when essentially sampling one grain at a time), but also constraints imposed by the requirements of compatibility between neighboring grains.

5.1.2 Change of chip morphology with depth of cut

Chip morphology is resulted from combined effects of crystallographic structure and machining condition, which can be treated as a direct representation of deformation behavior

Table 2: Chemical composition of Mg AZ31 alloy (wt.%)

Al	Zn	Mn	Si	Fe	Ca	Mg
3.1	0.73	0.25	0.02	0.005	0.0014	Balanced

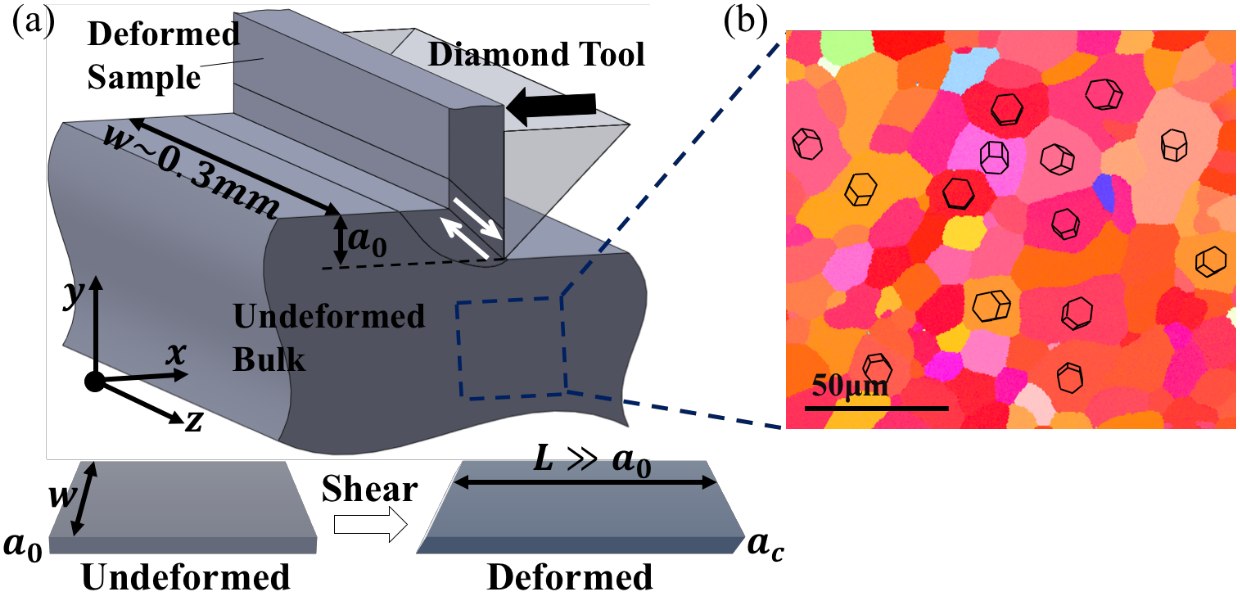

Figure 38: (a) Illustration of the plane-strain machining process. z direction corresponds to the normal direction of the bulk microcrystalline sheet, which is used in the experiments. *(Inset)* Geometry change from undeformed to deformed state is illustrated. (b) Orientation map (overlaid with mini crystal lattice to illustrate the orientation of individual grains) of bulk Mg AZ31 from electron backscatter diffraction, which illustrates a characteristic basal texture. Note that the shear deformation is imposed in a manner, which is not aligned with the basal slip in the majority of the grains.

in bulk material. In current work, the morphology change is mainly caused by size of deformation volume which is determined by machining condition given the prior microstructure of bulk material. The *in situ* experiments were performed for a range of a_0 values, while simultaneously imaging the material flow during deformation using the secondary imaging mode in the SEM. Figure 39 illustrates the change in morphologies of the deformed chips with different preset depth of cut a_0.

When $a_0 \sim 10\mu\text{m} \gg 100\text{nm}$, advancing the diamond cutting tool into the bulk Mg AZ31 attempts to impose shear deformation in an element of the material as illustrated in Figure 40. However, this element fails to accommodate large strains, in stead fractures, and plastic deformation plays only a small role in creating the segmented, serrated deformed material[5, 63]. This is a manifestation of the characteristic shear banding in Mg alloys, which is operative at the macro and micrometer length-scales. The intermittency in the deformation can be understood in the following manner (Figure 40a): an element of material is advanced into the deformation zone, where the strains are accumulated progressively. While, some plastic deformation can be accommodated, the progressive imposition of strains leads to fracture within shear bands at the nominal shear deformation zone. The fractured material displaces further along the surface of the diamond cutting tool and a new element of material is advanced into the deformation zone to continue this cycle (Figure 40c). This is a characteristic feature in My AZ31 alloy when the deformation geometry involves supercritical (micro/meso-macroscopic) length scales.

However, reducing $a_0 \sim 100\text{nm}$ regime indicates a switchover in the deformation response as seen in the morphology of the deformed material, which is illustrated in Figure 39b. In this situation, the material can accommodate the imposed strains fully via plastic deformation ahead of the diamond cutting tool, and the corresponding shear strain can be calculated as[65]:

$$\varepsilon = \cot\phi + \tan\phi > 2 \tag{5.1}$$

where ϕ is calculated from $\tan\phi = a_0/a_c$. a_c is again the thickness of the material which was plastically deformed to create chip from a prior undeformed depth a_0. Usually, $a_c > a_0$.

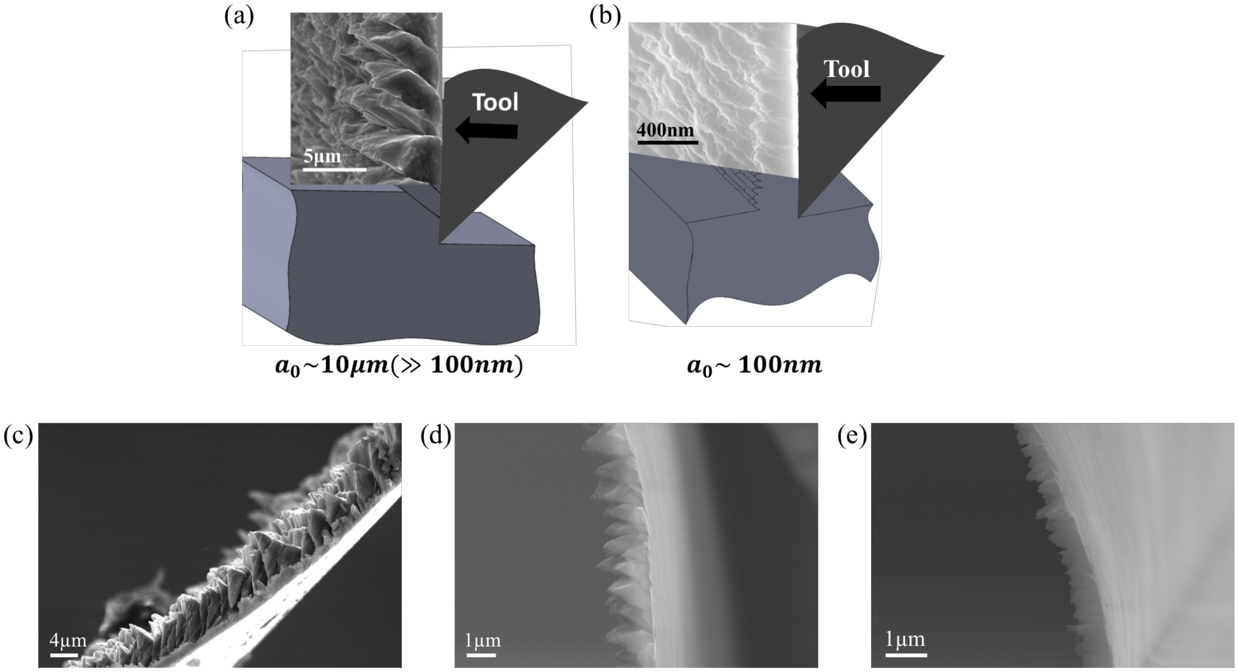

Figure 39: Schematic representation of distinct deformation regimes at two different length-scales, which are overlaid with SEM micrographs of the deformed material: (a) $a_0 = 10\mu\text{m} \gg 100\text{nm}$, and (b) $a_0 = 150\text{nm} \sim 100\text{nm}$. SEM micrographs of chips corresponding to different preset depth of cut (c) $a_0 = 5\mu\text{m}$, (d) $a_0 = 1\mu\text{m}$, (e) $a_0 = 0.3\mu\text{m}$. The machining velocity is kept at constant of $150\mu\text{m/s}$.

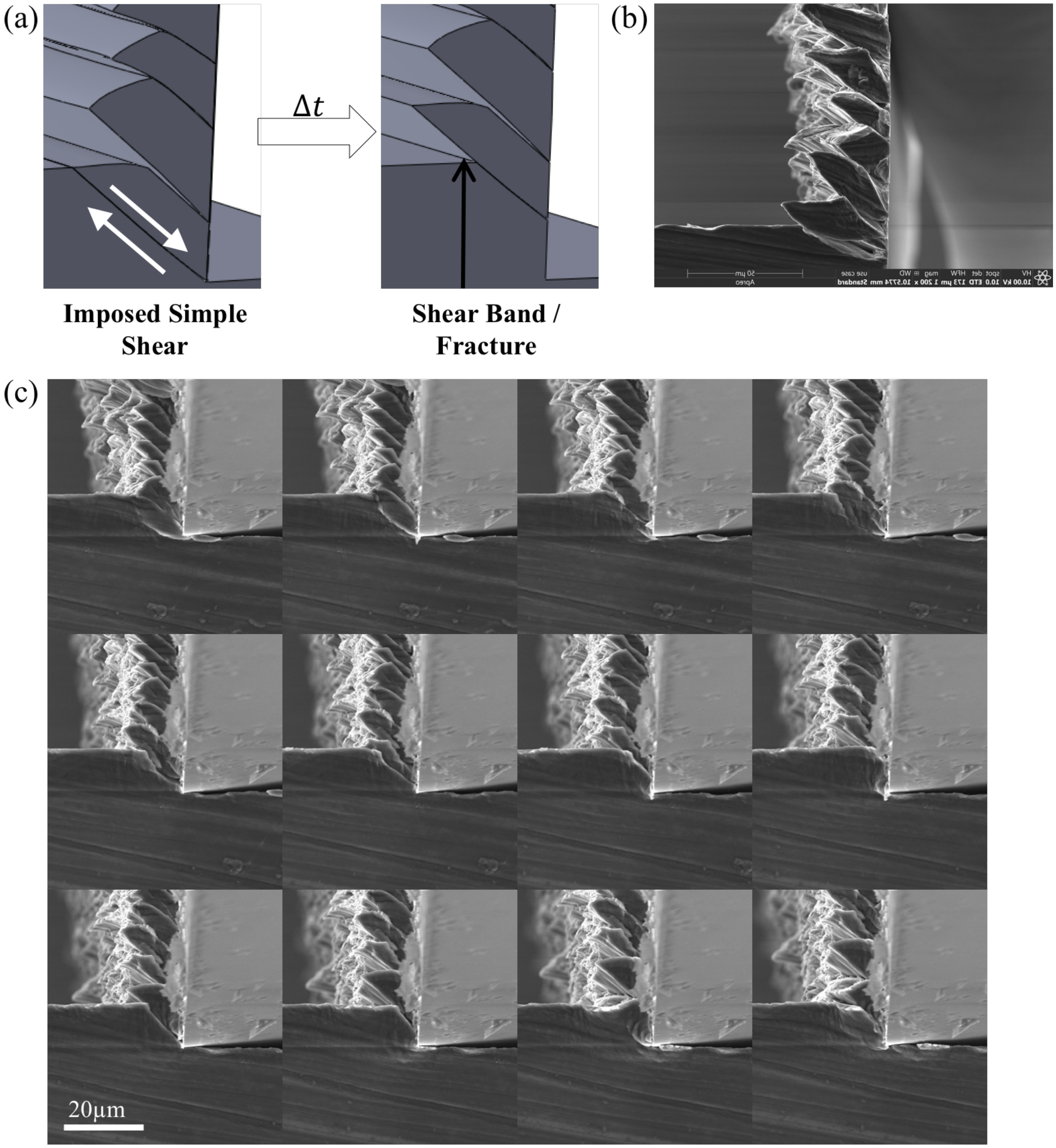

Figure 40: (a) Illustration of intermittent fracture leading to the serrated geometry of the deformed material, where segments of modestly deformed material are bound by shear bands. (b) SEM micrograph of intermittent fracture. (c) Sequential SE images showing the formation of serrated chips. Machining condition: $a_0 = 10\mu\text{m}$ and $V = 150\mu\text{m/s}$.

The strains are imposed in a shear deformation zone ahead of the diamond tool tip, which transforms the undeformed bulk into the severe plastically deformed material. Note that this calculation for large strain deformation via simple shear is not applicable in the case of fracture (as shown in Figure 40) if the material fails to accommodate the strains exclusively via plastic deformation.

To further examine the morphology change with respect to preset depth of cut a_0, a series of cross sections have been extracted from the machined chip under different preset depth of cut from $\sim 2\mu$m to $\sim 0.15\mu$m using FIB-based technique as shown in Figure 15. Figure 41a shows the assembled TEM micrographs. Here, the saw-tooth deformation is replaced with the characteristically "sinuous flow", typically associated with highly ductile and formable materials[78], as shown in Figure 41a with $a_0 = 0.15\mu$m. The intermittency of deformation is replaced by what appears to be continuous imposition of plastic deformation. Measuring the average thickness of the deformed material a_c and using equation 5.1 reveals an imposition of a shear strain of $\sim$ 2.6. To provide a frame of reference, Figure 41b illustrates the morphology of severely plastically deformed Cu sample, which deforms in a ductile manner under conditions similar to that used in Mg AZ31. The phenomenon of sinuous flow during otherwise large strain plastic deformation is a characteristic feature of machining-based deformation configurations, where a geometric boundary condition is not explicitly enforced on the free surface of the deformed material.

As shown earlier in Figure 38a, the bulk Mg AZ31 used here provides a variety of potential crystal orientations to be deformed. Thus, it is possible that some underlying grains are properly aligned for the shear deformation applied by machining process. Consequently, the deformed chips can also demonstrate characteristics from "sinuous flow" as shown in Figure 41 with $a_0 = 1\mu$m and $a_0 = 0.3\mu$m, which are also mixed with saw-tooth features. The switch-over from fracture-punctuated plastic deformation to "sinuous flow" of deformation behavior (which is agnostic to bulk grain orientation) is observed here when reducing $a_0 \sim$ 150nm.

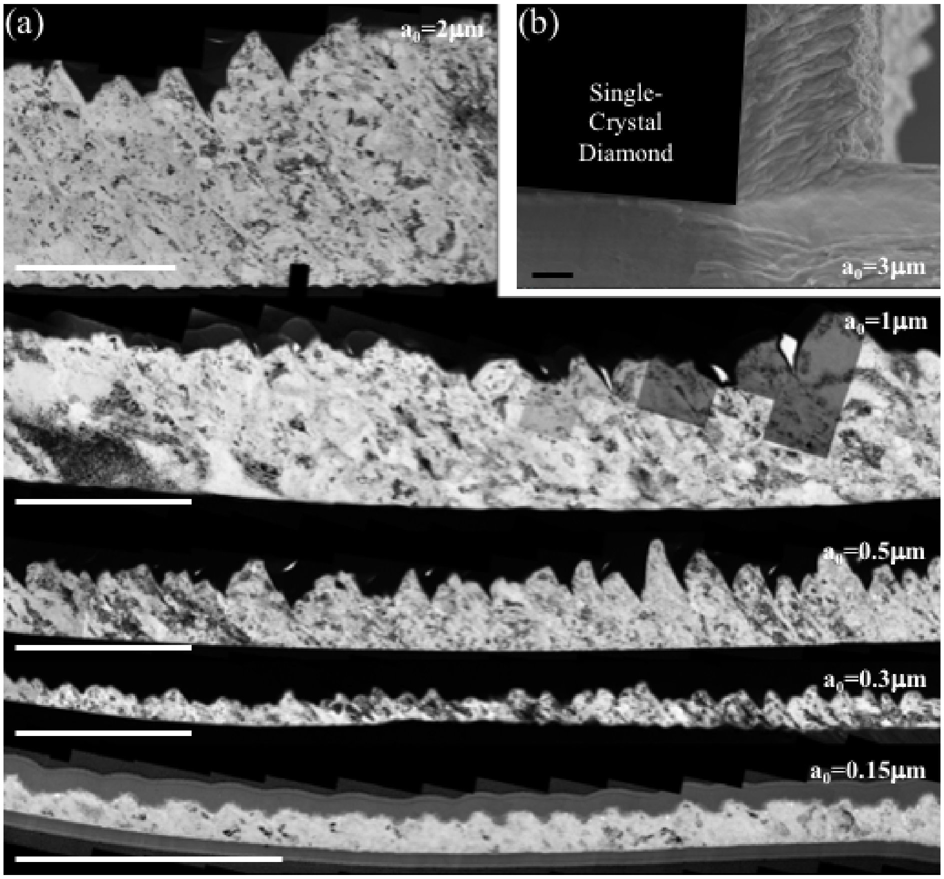

Figure 41: (a) Wide-area TEM micrographs of the deformed chips under different depth of cut a_0 (inserted on the topright corner). (b) A secondary electron micrograph captured during in-situ indentation of copper inside SEM with $a_0 = 3\mu$m. The severe plastic deformation concentrates along a confined deformation zone. As indentation proceeds, bulk copper flows through shear plane sequentially, forming waves with limited width on the backside. The sinuous flow in the deformed material is characteristic of severe shear in this deformation configuration. Machining velocity $V = 150\mu$m/s. Scale bar: 2μm.

5.1.3 Microstructure of deformed chips

While the aforementioned switch-over observed for the morphology of the deformed material yields circumstantial evidence, it is not sufficient to argue incontrovertibly whether severe plastic deformation actually occurred or not. Conclusion can only be made after examination of the resultant microstructures in deformed chips. While performing micromachining inside the SEM chamber, the diamond tool is stopped at a fixed distance from its last stopping position, leaving a series of deformed chips attached to the bulk material as shown in Figure 42a. Furthermore, the deformed chips (with preset depth of cut $a_0 = 0.15\mu$m) here are sufficiently thin and reasonably transparent to the electron beam of an SEM (with accelerating voltage of 10kV). This observation provides the base for direct imaging of a freshly generated chip using TEM without any thinning process. The following method was proposed to extract pieces of deformed chips as shown in Figure 42a: a sharp tweezer was used to pull chips off the bulk and the damaged area caused by the tweezer can be avoided considering the size of tweezer tip; these chips were subsequently emerged in a droplet of ethanol on the top of a TEM grid (with Formvar film); the deformed chips would lie down on the grid after complete evaporation of ethanol; the specimen was then put in plasma cleaner (Model 1070 NanoClean from Fischione Instruments) to remove the supporting film with only Ar gas supply; finally deformed chip piece lying down on the Cu grid can be achieved ready for TEM characterization, i.e., plane-view.

Direct observation from TEM did not reveal an intermittently cracked or an inhomogeneously deformed material. Recall that while $a_0 \ll$ grain size in the bulk material, the deformed chip is essentially macroscopic along the $z-$axis and also the $y-$axis, where the deformation samples multiple grains (albeit individually deformed in plane-strain condition). Note that there is transformation of coordinate systems when transferring deformed chips: while a_0 is set along the $y-$axis, in the deformed material it is along x-axis because simple shear deformation involves a rigid rotation by 90°.

Both bright field images and corresponding selected area diffraction (SAD) patterns in Figure 42b reveal nanocrystalline deformed structure with a grain size < 100nm. Such microstructure refinement from an otherwise microcrystalline bulk is commonly observed when

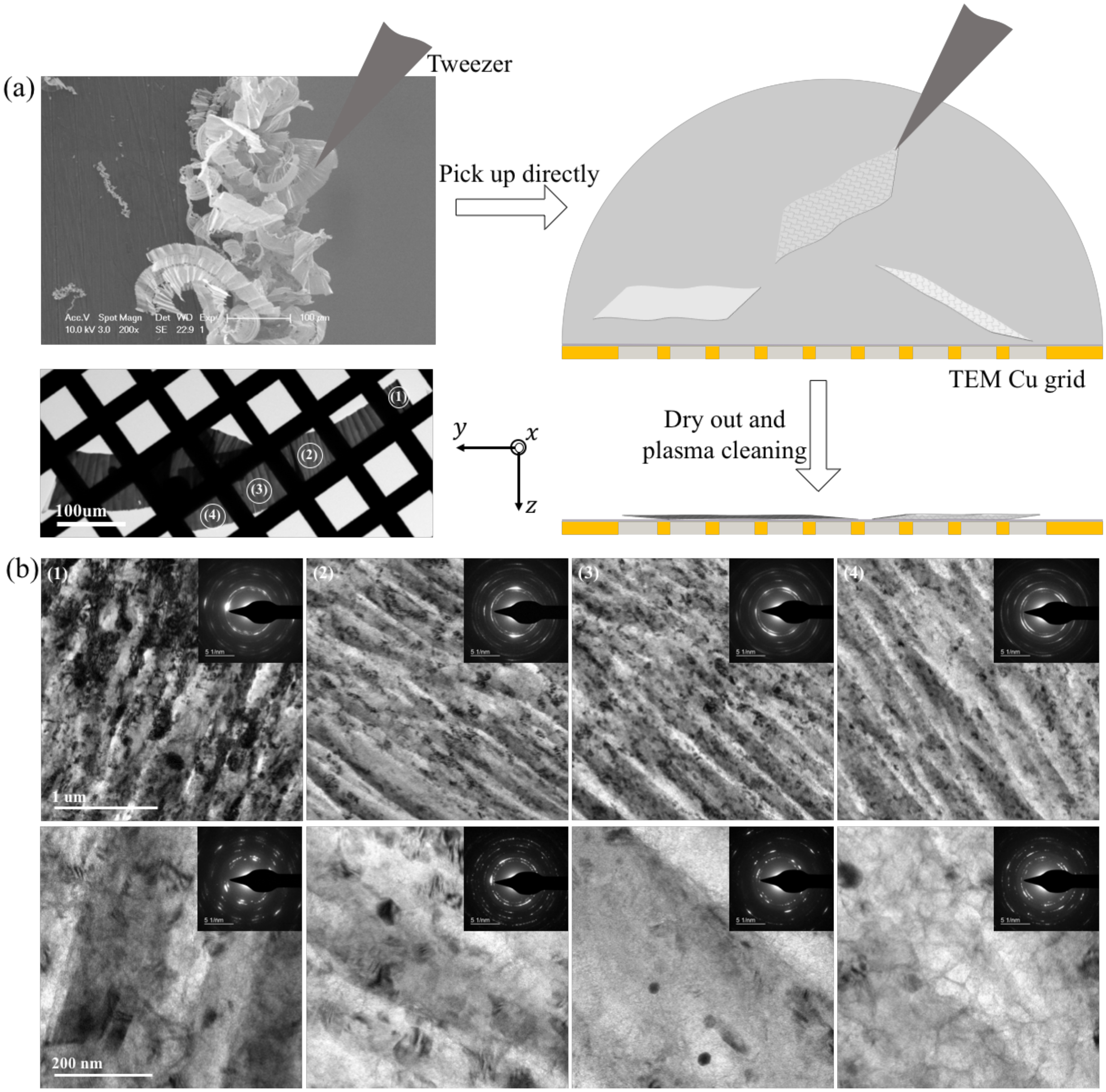

Figure 42: (a) Illustration of transferring machined Mg AZ31 chips onto TEM Cu grid with machining conditions $a_0 = 150\text{nm}$ and $V = 150\mu\text{m/s}$. Note that the sample is macroscopic along y and z axes. (b) Bright field transmission electron micrographs of the plastically deformed chips for four randomly selected areas, which are labeled in (a). *(Inset)* Selected area electron diffraction pattern.

a ductile material is subjected to severe plastic deformation (recall the deformed material of Cu as shown in Figure 23). But, Mg AZ31 is not known to undergo such plastic deformation at ambient temperature. It is also noteworthy that the dimension of the deformed sample shown in Figure 42a is at the 100nm−scale only through its thickness; the length and width are macroscopic and the deformed nanocrystalline deformed structure originates from a multitude of parent grains which are randomly sampled from bulk material. Thus, refinement of just one characteristic length of the deformation (preset depth of cut a_0 here), results in dramatic switch-over in the characteristic deformation behavior. Therefore, the underlying switch-over in the deformation mechanism is likely agnostic to the underlying orientations of the individual grains of the undeformed parent material. Indeed, $a_0 = 150$nm is is much smaller than the typical grain size of the parent material, Mg AZ31 $\sim 30\mu$m. However, the large lateral width and length dimensions of the deformed material volumes reveal that irrespective of the parent grain orientations, Mg AZ31 can undergo both intra- and inter-granularly-compatible plastic deformation to large shear strains under ambient conditions to create an integral deformed sample akin to that in Figure 42a.

To characterize the deformation behavior switch-over and associated morphology change observed here consistently when the magnitude of preset depth of cut a_0 is reduced to 150nm (Figure 39a and b), focused ion beam milling was used to lift out cross-sections of the deformed materials parallel to $x - y$ plane in Figure 38a following procedures shown in Figure 15. Subsequently, low energy Ar$^+$ milling was applied to reduce FIB-induced damage.

The bright field images of a cross-section of the deformed samples are shown for $a_0 = 2\mu$m in Figure 43a and $a_0 = 150$nm in Figure 44a, which mirror the morphologies illustrated in Figures 39a and b, respectively. Even though a smaller a_0 value was chosen in Figure 43a to enable FIB milling than that illustrated in Figure 39a (where $a_0 = 10\mu$m), the segmented, deformed geometry is very similar–Mg AZ31 undergoes its characteristic shear banding at length-scales $\gtrapprox 2\mu$m. TEM based orientation imaging microscopy (OIM) micrographs corresponding to Figures 43a and 44a are shown in Figure 43b and 44b, respectively.

Figure 43a illustrates an intermittently plastically deformed material, where discrete segments of the material are separated by shear bands. Fracture typically occurs in the shear bands to create the saw-toothed morphology in Figure 39a. A shear band is illustrated using a dashed white line as a guide for the eye in Figure 43a. Due to insufficient number of available slip systems, the deformation of each discrete segment is mainly accommodated via basal slip and/or twinning (if possible)[62]. Only a limited accommodation of plastic strain occurs, which results in a coarse sub-grain structure in segments of Figure 43a. The segments are bounded by shear bands. The orientation map in Figure 43b illustrates the inhomogeneous deformed microstructure, which corresponds to a region indicated in Figure 43a. While, basal slip can be extensive in Mg AZ31, the ability to accommodate large strains is usually limited. Strain localization and shear banding in Mg AZ31 are linked to the interplay of basal slip and twinning, which becomes operative at increasing strain levels[63, 62]. Typically, shear banding is associated with dynamic recrystallization and microstructural inhomogeneity, which manifests during the characterization of the deformed specimens[46]. Figure 43b illustrates a segment of a moderately deformed material, which is bounded by dynamically recrystallized shear bands. This is also illustrated via the schematic in the lower part of Figure 43b. The shear bands also coincide with the locations of the saw-tooth features, where fracture leads to segmentation of the deformed material.

In contrast, the deformed material with $a_0 = 150$nm features a uniformly nanocrystalline structure as illustrated in Figure 44a. The microstructure does not show the inhomogeneity observed at the larger length-scale as illustrated in Figure 44b. The TEM micrographs in Figures 44a and 42b reveal an integral sample with no evidence of fracture or cracking, which reinforces the idea that the material accommodates the severe plastic strains. Also, see Figure 41 for a larger micrograph of the deformed material produced with $a_0 = 150$nm, which illustrates a sample devoid of the characteristic microstructural inhomogeneity observed at the larger length-scale (e.g. Figure 43a). The kernel average misorientation map in Figure 44c illustrates a defect-ridden material, which is consistent with accommodation of large plastic strains when one length-scale of the deformation is refined sufficiently. Figure 44d confirms a significant portion of the grain boundaries in the deformed material being of a large misorientation, with the grains size skewed to the sub-100nm scale as shown in Figure 44e. We do not find any signs of deformation twinning, which is consistent with the expectation that dislocation plasticity plays a major role in accommodating large plastic strains in Mg AZ31 at refined length-scales[82].

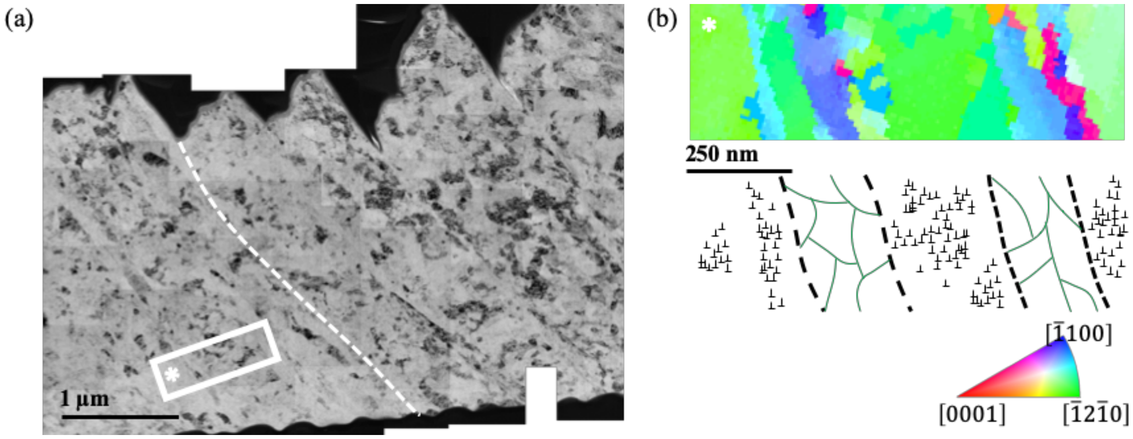

Figure 43: (a) Bright field image of cross section of deformed material from Mg AZ31 produced with $a_0 = 2\mu$m. The dashed white line is a guide for the eye showing the location of a shear band. (b) Orientation map of a selected area in (a) (indicated with a white rectangle) and a schematized illustration of shear banded microstructure. Refer to the color triangle below (b) for orientation encoding in (b). Velocity of diamond cutting tool $V = 150\mu$m/s.

5.1.4 Microstructure evolution

A partially detached specimen (schematized in Figure 38a) will contain the full trajectory of the microstructure evolution from the pristine bulk to the severely deformed material with mature strains, across the deformation zone. An FIB-based method (refer to Figure 16) was used to extract such a sample. Figure 45a shows a sample surrounded by a Pt protection layer and Figure 45b illustrates its orientation map. Given the grain size of bulk Mg AZ31, the deformation configuration essentially samples a small volume within a single grain in a given increment of time. In Figure 45a, the orientation of the undeformed material is not favorable for basal slip to accommodate the imposed shear (see *inset* in Figure 45b). Still, the deformation results in a homogeneously nanocrystalline structure in the deformed material. The dislocation sub-structures including incidental dislocation boundaries (IDBs, owing to statistical storage of dislocations) [51] and geometrically necessary boundaries (GNBs, accommodating crystal lattice bending caused by strain gradient in plastic deformation) [32],

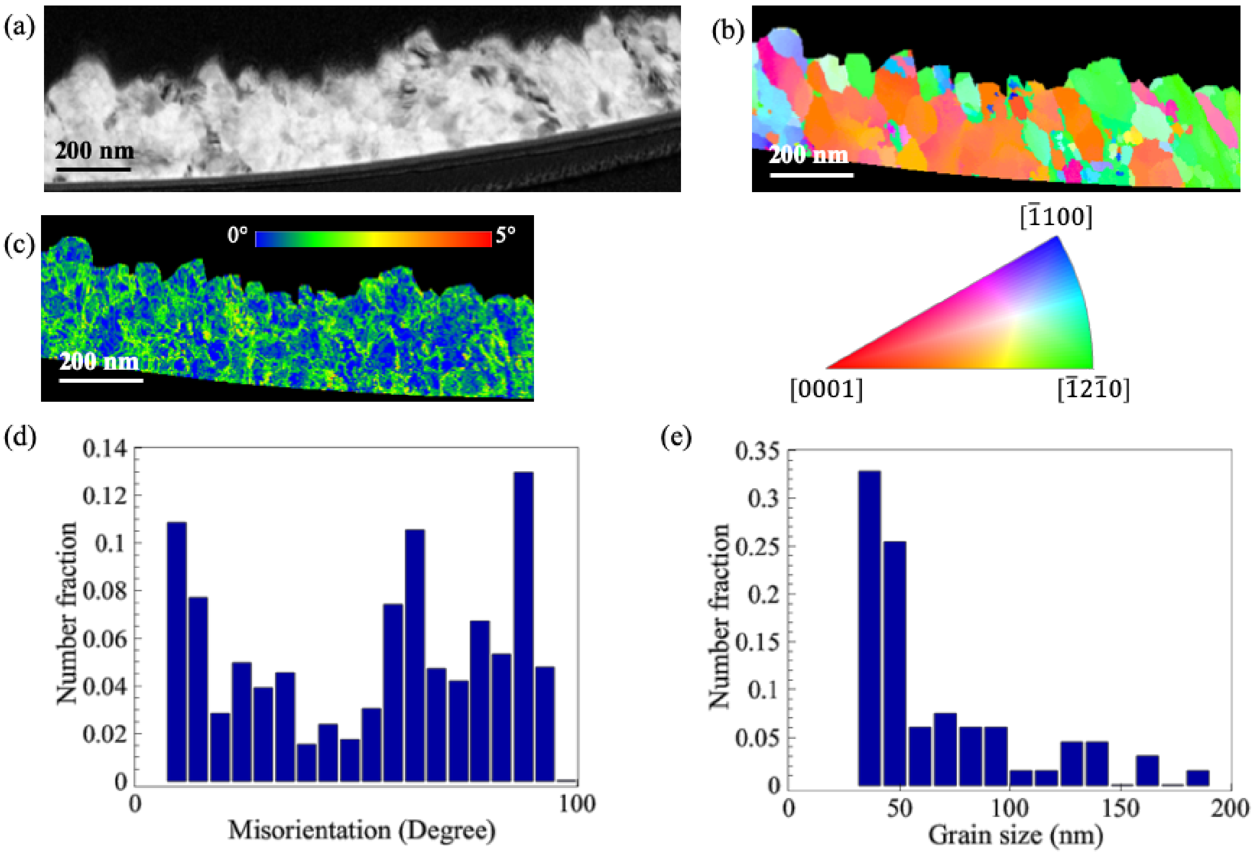

Figure 44: (a) Bright field image of cross section of deformed material with $a_0 = 150$nm. (b) Orientation map of selected area in (a) obtained vis TEM OIM. (c) Kernel average misorientation map corresponding to (b). (d) Crystallographic misorientation distribution ($\geq 5°$) and (e) grain size distribution (for crystallites separated by boundaries with misorientation $\geq 15°$) corresponding to conditions in (b). Refer to the color triangle below (b) for orientation encoding in (b). Velocity of diamond cutting tool $V = 150\mu$m/s.

increase their mean misorientations gradually with progressive shear deformation, developing high angle boundaries. This is illustrated in the plot, which tracks the evolution of the misorientations from the parent undeformed grain in the bulk to deformed material (Figure 45c). The trajectory of the evolution of these misorientations is measured along the arrow in Figure 45b. Figure 45d illustrates an experiment where the deformation traverses a grain boundary. Two grains, whose orientations are schematized in insets are shown to deform plastically to large strains, while also retaining compatibility between them. This provides direct evidence for the switch-over in the deformation behavior of Mg alloys being essentially agnostic to the grain structure. The continuity of shear is maintained across the boundary, presumably by activating additional slip systems for maintaining compatibility of the large shear strains [57]. In the deformed material, it is possible to trace back the location of the grain boundary in the undeformed state. This is illustrated using two white arrows in the deformed material, which mark the putative location of the boundary in the undeformed state.

5.1.5 Switch-over in deformation mechanics

The well-known poor formability of Mg alloys at room temperatures has been attributed to the preponderance of basal slip vs. non-basal systems, with twinning offering a modest supplementary route for strain accommodation. Notable exceptions arise only in specially oriented magnesium single crystals, where twinning and subsequent dynamic recrystallization can aid accommodation of large strains [46]. In general, however, when external loading directions are agnostic to underlying crystal orientations, twinning is not only an intermediary step, but is often a precursor to rapid shear localization, poor formability and fracture. It has been argued that the formation of so-called "shear cracks" result from strain localization in shear bands in bulk Mg AZ31 when twinning and basal slip are both depleted as strain accommodation mechanisms [5]. Here, we find that refining a_0 only (as shown in Figure 38a) appears to generate a deformed behavior that is dominated by multi-slip and engenders microstructure refinement, which is otherwise associated nominally with highly-formable metals. The diminution of the role of twinning and dominance of dislocation multi-slip has

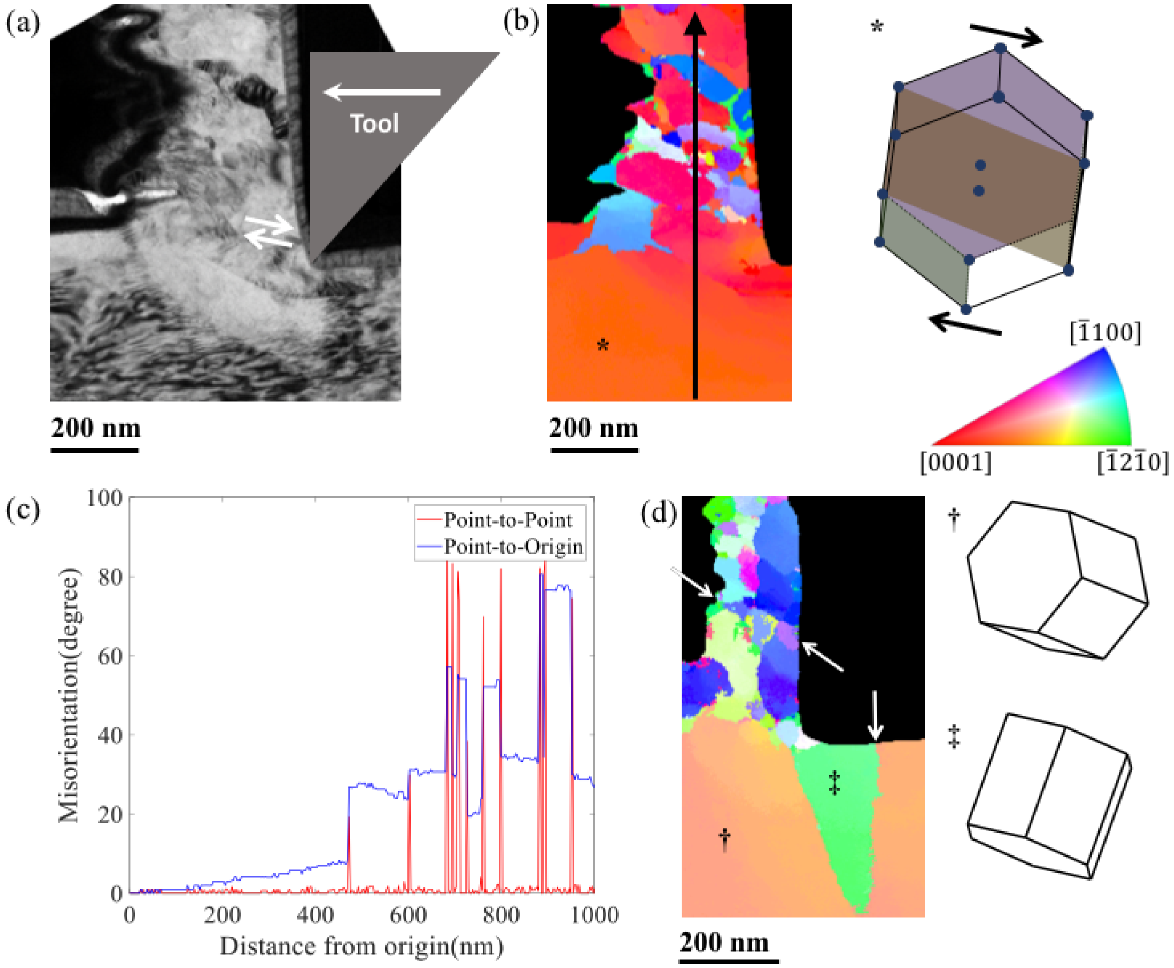

Figure 45: (a) Bright field image of partially detached specimen from Mg AZ31. The nominal shear direction is illustrated by two white arrows. (b) Orientation map corresponding to the deformation zone in (a). Crystal orientation and the shear direction are shown in *inset*. (c) Point-to-point and point-to-origin misorientation along the arrow in (b) illustrates the progressive evolution of a nanocrystalline grain structure via the imposition of severe shear deformation. (d) Orientation map of a partially detached specimen when deforming across to a grain boundary is shown. The pair of white arrows in the deformed material indicate the location of the boundary, which is indicated on the undeformed bulk. Orientation of the neighboring undeformed grains is shown in inset. Machining condition: $a_0 = 150$nm and $V = 150\mu$m/s.

been recognized at small length-scales [82], though our experiments reveal that the dimensionality dictating that switch-over is 1 (characteristic length-scale of deformation geometry) and not 3 (the entire sample volume).

Deformation twinning, as a highly coherent inelastic shearing process, typically requires high local stress concentration. Nucleation of twinning at grain boundaries in suitably oriented grains is known to be active in macro-scale deformation volumes [46]. However, the role of twinning has been found to diminish with decreasing sample volumes [82], where activation of slip becomes more favorable [13, 34, 81]. This is compounded by the high interfacial energies of twin boundaries in Mg $\sim 80 - 120\text{mJ/m}^2$ [75].

In prior work on an analogous deformation experiments, albeit at macroscopic length-scales, it has been shown that Mg AZ31 demonstrates prolific twinning and the deformed material is characteristically shear localized [8]. In Figures 43, 44 and 45, we find no evidence of twinning in the deformation zone. Thus, with shrinking characteristic length-scale of the deformation geometry when $a_0 \sim 100\text{nm}$, twinning—which is a critical precursor for shear banding, is suppressed. But, while localization is inhibited, the question then remains—how are multiple slip systems being activated to accommodate the severe shear strains imposed by machining?

The ratio of critical shear stress for activating basal ($\tau_{\text{CRSS}}^{\text{basal}}$) vs. say, prismatic ($\tau_{\text{CRSS}}^{\text{prismatic}}$) slip systems in Mg AZ31: $M_0 = \tau_{\text{CRSS}}^{\text{basal}}/\tau_{\text{CRSS}}^{\text{prismatic}}$ is typically in the range $\sim 10^{-1}$ to 10^{-2} [34]. This mismatch M_0 is at the root of the poor formability.

However, confining a_0 also leads to a magnification of the strain gradients in the deformation zone. It is clear from Figure 45c that the microstructure evolution is progressive through the deformation zone, where severe shear strains are imposed. The extent of the deformation zone (δ) is essentially proportional to a_0 (Figure 46a) and as such, the geometrically necessary dislocation density due to strain gradients (ρ_{g}) scales as $\rho_{\text{g}} \sim 1/(ba_0)$ [24]. b is the Burgers vector $= 0.32\text{nm}$. The geometrically necessary dislocation density leads to strain-gradient induced hardening of slip, which modifies the critical threshold for inducing slip on both basal and non-basal slip systems. Thus, the mismatch (M) for activating basal vs. say, prismatic slip is:

$$M = \frac{\tau_{\text{CRSS}}^{\text{basal}} + \alpha b \mu \sqrt{\rho_{\text{g}}}}{\tau_{\text{CRSS}}^{\text{prismatic}} + \alpha b \mu \sqrt{\rho_{\text{g}}}} \tag{5.2}$$

where $\mu = 17\text{GPa}$, $\alpha \sim 1$. For AZ31, $\tau_{\text{CRSS}}^{\text{basal}} \sim 10\text{MPa}$ and $\tau_{\text{CRSS}}^{\text{prismatic}} \sim 100\text{MPa}$. For the scaling arguments we employ there, this is roughly the order-of-magnitude observed in prior experiments [4]. Figure 46b illustrates M as a function of a_0, which illustrates how strain gradient effects can reduce the mismatch when a_0 decreases. In particular, we find that when $a_0 \sim 150\text{nm}$, the mismatch $M \sim 0.9$. Thus, refining a_0 enables accommodation of large plastic strains via multi-slip, while engendering the characteristically dramatic microstructure refinement. This underpins a switch-over from shear-banding/fracture behavior to one characterized by homogeneous deformation.

5.2 Deformation of Pure Mg

Here, we also examined the deformation behavior of pure Mg as a function of preset depth of cut a_0. The microstructure of bulk pure Mg is shown in Figure 47. The average grain size of bulk pure Mg is around $\sim 65\mu\text{m}$, which is again much larger than the preset depth of cut a_0 ($\leq 5\mu\text{m}$).

As pointed in Chapter 2, the solute elements in Mg AZ31 significantly hinders the growth of recrystallized grains due to the drag effect on grain boundary mobility.It would not be surprising to see relatively larger grains in the deformed chips when compared with that corresponding to Mg AZ31. Figure 48 shows the orientation map and reconstructed virtual bright field image by TEM/OIM in plane view (refer to $y-z$ plane in Figure 38) and confirms a coarser deformed microstructure.

Figure 49 shows that corresponding distributions of grain boundary misorientation (with over 90% being HABs and mea value $\sim 56°$) and size (with mean size being $\sim 920\text{nm}$) of the machined chips. It shows that this deformed chip has undergone rampant dynamic recrystallization leading to coarsened grain structure and almost complete loss of fine grains. This case has been seen in high-speed machining of Cu[66]. As shown earlier, the temperature

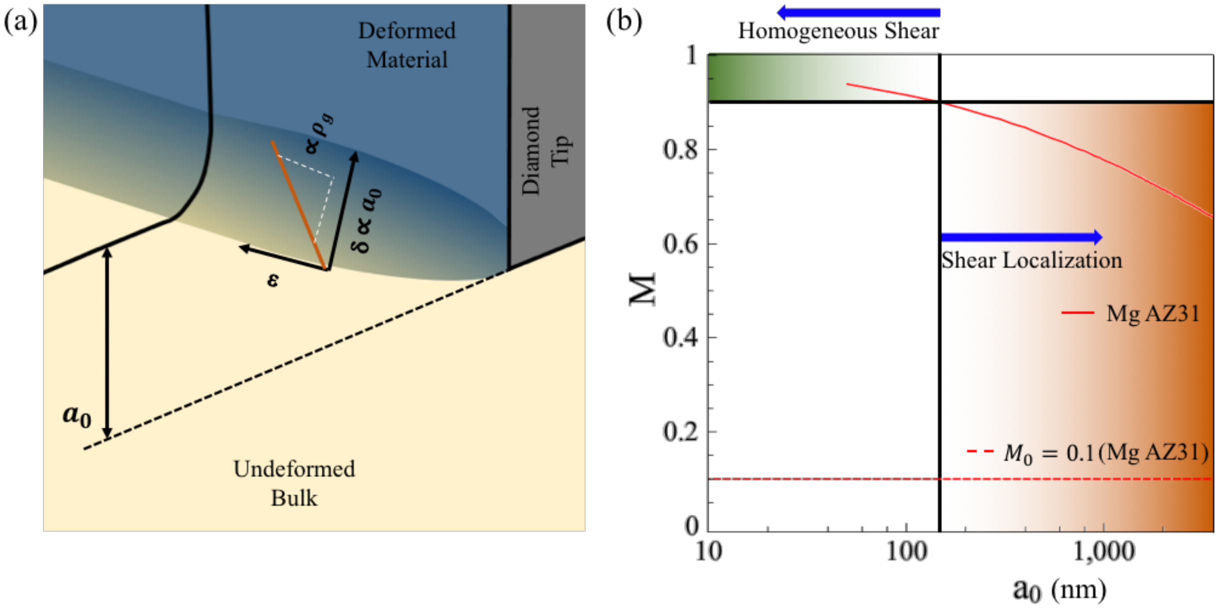

Figure 46: (a) Schematic of strain gradients in the deformation zone of asymmetric wedge-indentation. (b) Mismatch factor (M) as a function of a_0. When a_0 reaches below $\sim$ 150nm, $M > 0.9$. Thus, activation of multiple slip systems becomes easier and homogeneous accommodation of severe shear strains becomes feasible. When $a_0 \gg 100$nm, intermittent plastic deformation involving shear localization and fracture is the characteristic feature.

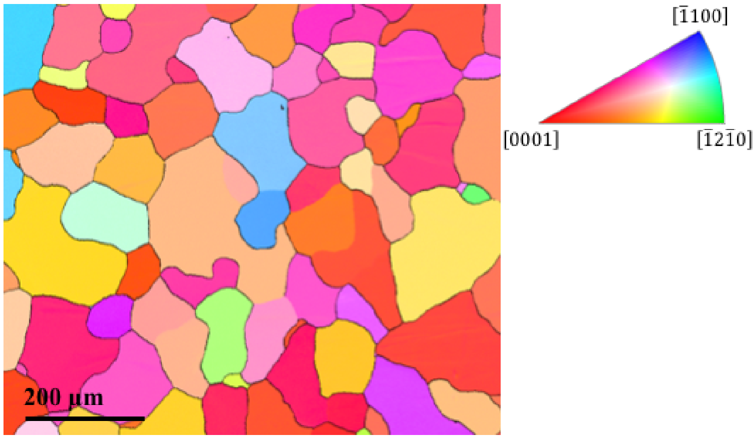

Figure 47: Orientation map of bulk pure Mg from electron backscatter diffraction. Refer to the inserted triangle (right) for color code. Note here, the imposed shear deformation is again not aligned with basal slip in the majority of the grains.

associated with this deformation process is negligible (below 10K). This dynamic recrystallization can only be driven by the crystallographic curvature from high strain gradients due to spatial confinement but only one dimension is sufficient.

Figure 50 shows a wide-area TEM micrographs of a cross section extracted from deformed chips with preset depth of cut $a_0 = 150$nm. This $\sim 5\mu$m-long chip contains only 5 grains, and each of them is much larger than the thickness of deformation zone (the characteristic length scale of deformation). This fact essentially excludes the role of DDRX since the stochastic nucleation of new grains and subsequent growth make it extremely difficult to form a single crystal over multiple consecutive simple shear deformation process as material passes through the deformation zone.

5.3 Potential topology design for improved formability

Refining one characteristic length-scale of the deformation geometry to the $\sim$ 100nm scale in a plane-strain machining configuration leads to a switch-over in the deformation

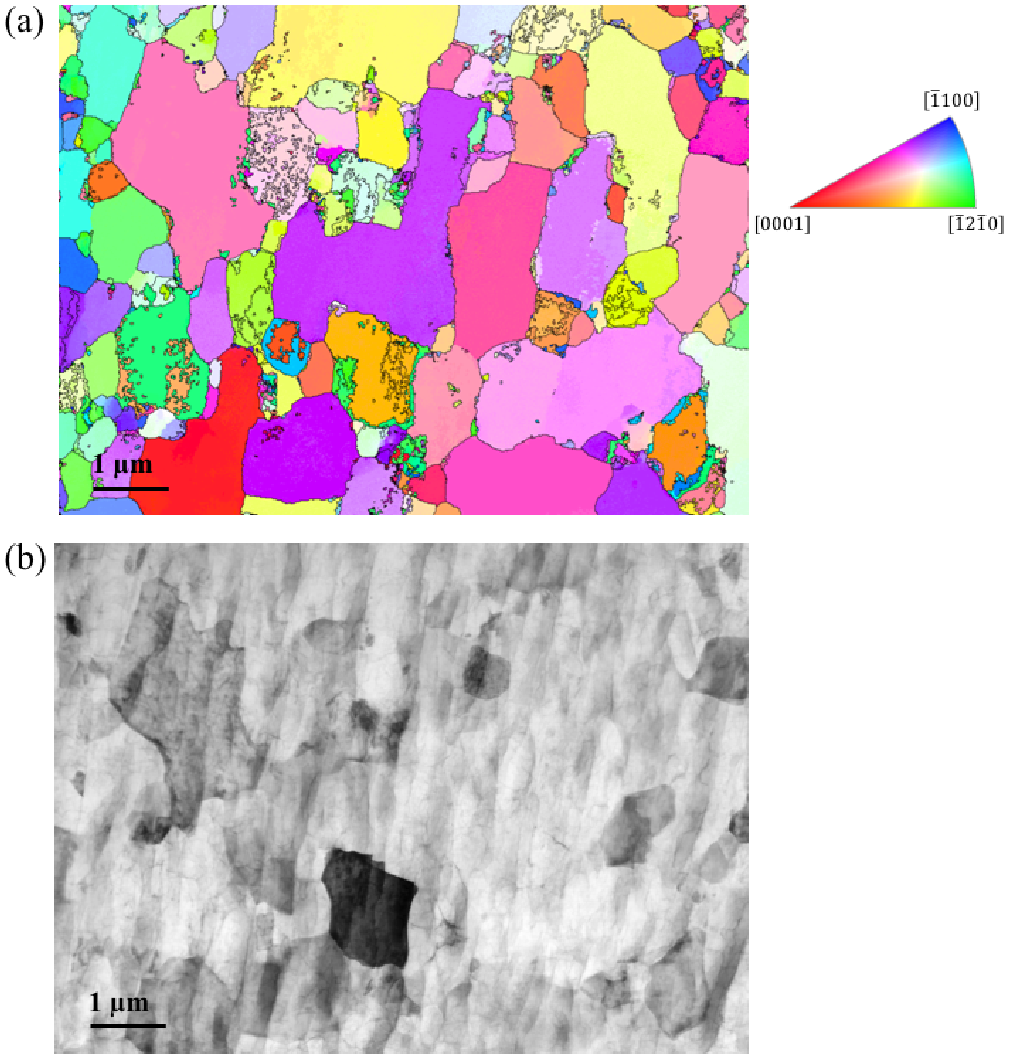

Figure 48: (a) Orientation map obtained via by ASTAR system. Refer to the inserted triangle (below) for color code. (b) Virtual bright field image generated from the corresponding scanning process. Machining condition: $a_0 = 150$nm and $V = 150\mu$m/s.

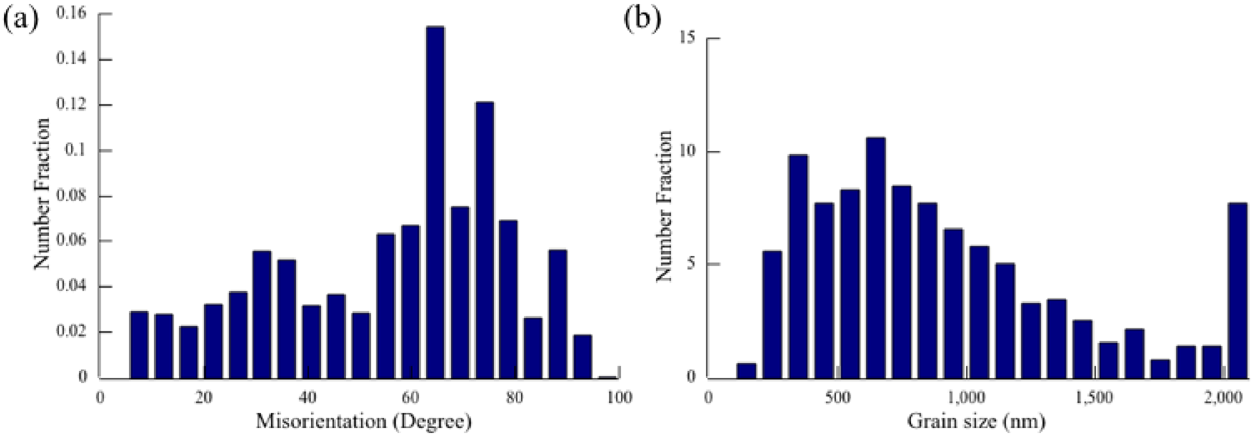

Figure 49: (a) Crystallographic misorientation distribution ($\geq 5°$) and (b)Grain size distribution (for crystallite separated by boundaries with misorientation $\geq 15°$) of machined chips from pure Mg with $a_0 = 150$nm and $V = 150\mu$m/s. Here the grain size is calculated via line intercept method.

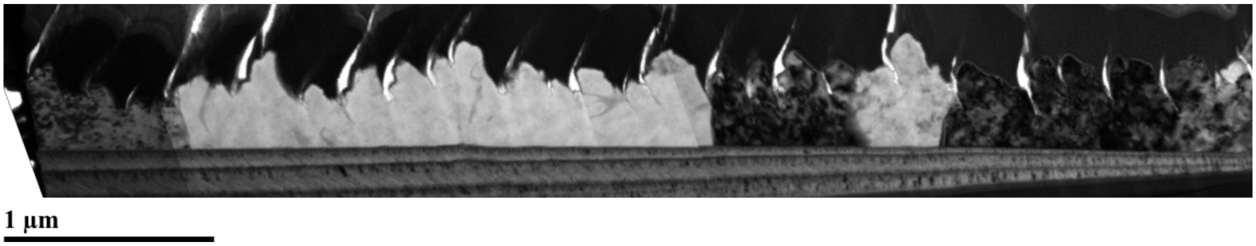

Figure 50: Bright filed image of cross section of machined chips with $a_0 = 150$nm and $V = 150\mu$m.

mechanics of Mg under ambient temperature conditions, even when the other dimensions are essentially macroscopic. The characteristic shear banding and fracture is suppressed and severe plastic deformation to strains > 2 ensues, which leads to microstructural refinement in a manner that is otherwise observed in nominally formable metals. While, the suppression of twinning under these conditions eliminates a critical precursor to the localization of strains in shear bands, the magnified strain gradients offer a pathway for reducing the mismatch in the critical shear stresses required for activating basal and non-basal slip systems.

The realization that strain gradients in the principal shear direction along with the spatial confinement hold the key to improving the ductility can lead to a framework for designing microstructures in Mg with improved mechanical property combinations. Consider a Mg matrix illustrated in Figure 51a, which is intercalated with an ultra-thin corrugated structure (X). The microstructure of Mg can be arbitrary and the role of the X-phase is to generate strain gradients in a manner that mimics the indenter in Figure 38a. This can be accomplished using materials such as Mo or Nb for X, which are expected to possess very small solubility in Mg. Consider the thickness of X$\sim 1 - 10$nm, while $t \sim 100 - 200$nm. When this structure is subjected to shear, a zone of plasticity will be induced at the apex of the intercalated phase (X), which mimics the role of the machining tool. The inset in Figure 51a can be thought of as two "machining tools", which apply large shear deformation to accommodate the applied shear strains. The strain gradients and the spatial confinement enable multi-slip and large strain plasticity, irrespective of the grain structure/orientation of the parent Mg phase. If the periodicity of the features λ is also comparable to t, the zones of plasticity at each of these "machining tools (X)", characterized by the large strain gradients and ductility can overlap. Large strain plasticity is accommodated homogeneously throughout the structure and the observations outlined in this work can be translated to design highly formable bulk Mg composites.

Note that this idea is distinct from the pursuit of nanolaminates to achieve high strength [29]. This can be ancillary benefit, although we have not explored the effect of spatial confinement on the flow strength during the nanomachining process. Figure 38b illustrates how such composite topologies can be exploited to engineer highly formable sheet metal forms in Mg. The idea is to enable large shear plasticity at $\sim 45°$ to the principal tensile

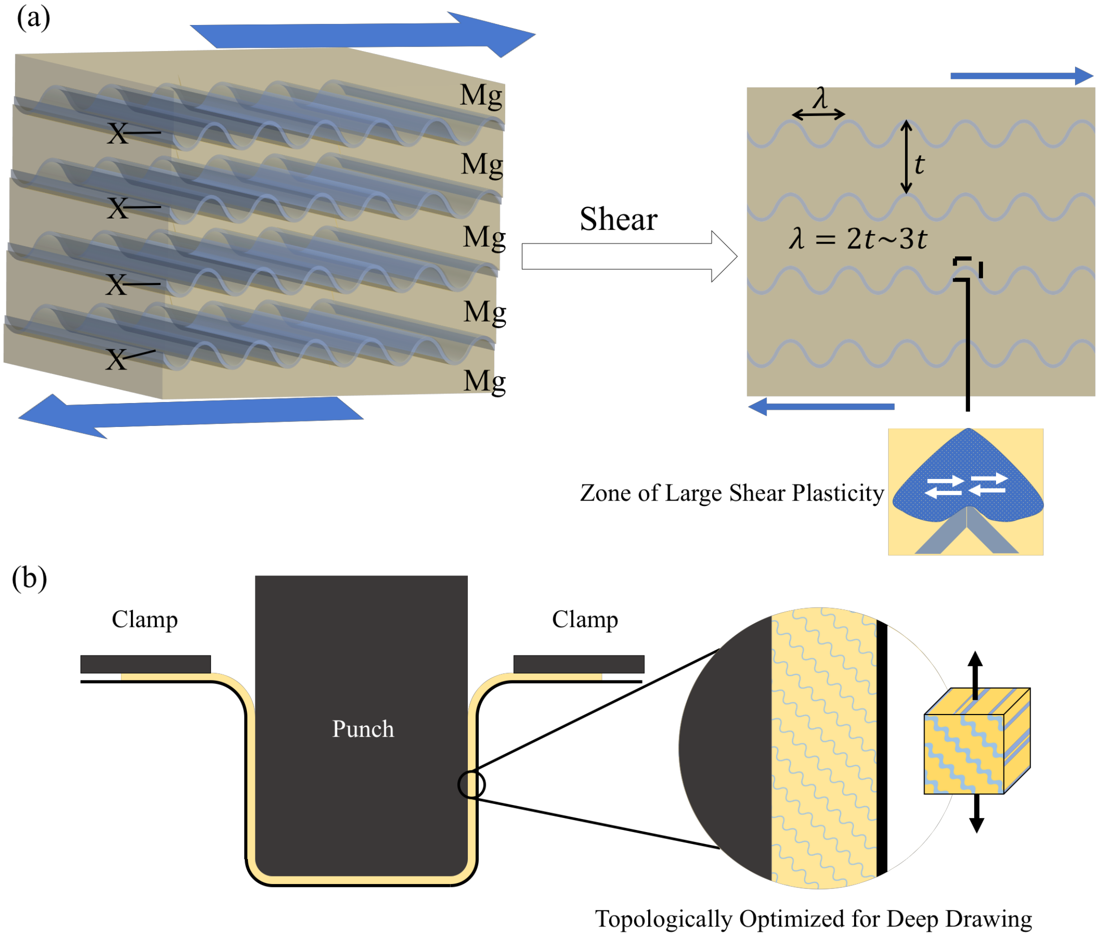

Figure 51: (a) Exploiting the reduced dimensionality of the switch-over to large strain plasticity in a laminate structure, where an intercalated phase is used to mimic the effect of the indenter in Figure 38. (B) The ability to sustain severe deformation can be exploited by designing structural topologies optimized for improved formability. The example here illustrates a laminate structure, which can enable deep drawing of sheet metal forms without resorting to microstructure engineering or alloy design.

strain direction. This points to a pathway, where optimizing the topology of the structure, instead of optimizing the texture, composition or microstructure offers a route for achieving improved formability.

5.4 Summary

Magnesium alloys have long been a fascinating material platform for achieving step-changes in light-weighting of structural components in the aerospace, defense and transportation sectors. Unfortunately, Mg's crystal structure endows with highly anisotropic response to plastic deformation. Poor formability results from a characteristic tendency to shear localize and fracture. While this is characteristic at the macro-scale, a switch-over to a more ductile response has been observed when the sample volume is reduced (typical $< \mu\text{m}^3$). Here, we demonstrate that dimensionality of the deformation geometry, which controls the switch-over in deformation mechanics is in fact, fewer than three dimensions. By utilizing asymmetric wedge indentation/plane strain machining as a test of material response, it is shown that Mg alloys can accommodate shear strains of over 200% when just one characteristic length-scale of the deformation geometry is reduced to the 100nm-scale. The other dimensions can be orders-of-magnitude larger and even macroscopic. The switch-over occurs at ambient temperatures and the deformed material illustrates microstructure transformations, which are characteristic of one resulting from severe plastic deformation. Intriguingly, this deformability to large plastic strains occurs irrespective of the prior orientation of the undeformed crystals and is agnostic to the presence of grain boundaries. By tracking the progression of the microstructure evolution across the deformation zone from the undeformed 10's of μm-scale crystals to $\sim$ 100nm-scale deformed structure, we note the evolution of large strains in a spatially-confined deformation zone. We show that shrinking one dimension of the deformation volume is sufficient to suppress the characteristic strain localization, shear banding and fracture in Mg alloys, while simultaneously enabling the accommodation of large plastic deformation via rampant multi-slip dislocation activity. This observation motivates the realization that achieving an optimized balance of mechanical properties in bulk Mg alloys is possible by engineering topologically optimized structures in fewer than 3-dimensions and without requiring precise microstructural engineering. This offers a pathway, which is distinct from prior approaches aimed at improving the ductility of Mg–ranging from alloy design, microstructure design, nanocomposites etc.

6.0 Conclusion and Future Work

In this thesis, we examined the mechanics of deformation and corresponding microstructure evolution during imposing severe plastic deformation at the micro/nano-meter length-scales on two different material systems face-centered cubic Oxygen Free High Conductivity Cu and hexagonal close-packed pure Magnesium and Mg AZ31.

The response of OFHC Cu to severe plastic deformation imposed by machining at the micrometer length-scale demonstrates a strong dependence on the bulk grain orientation. With aid of *in situ* experiments inside SEM, the deformation mechanics was revealed via digital image correlation. Subsequently, microstructure evolution during severe plastic deformation was characterized by performing EBSD, which spans the gamut from ultra-fine grained structure to complete lack of refinement. As a companion of chip formation, the integrity of surface from machining polycrystalline Cu is also related to the orientation-dependent deformation anisotropy. Grain boundary defects fundamentally originate from rampant ductile tearing in the vicinity of grain boundary.

The response of the hexagonal crystal lattice in Mg to plastic deformation is highly anisotropic, which results in the localization of plastic strains and an inability to achieve homogeneous shape change. Here, we demonstrate that refining one characteristic dimension of the deformation geometry down to the 100nm-scale triggers a brittle-to-ductile transition in Mg and AZ31 at ambient temperatures. The other two dimensions can be substantially larger or even macroscopic. The ability of Mg to accommodate shear strains greater than 200% in this configuration is independent of the orientation of underlying crystals with respect to the loading direction. This implies that achieving the combination of low-density, high strength and formability in Mg can be accomplished by designing microstructure and composites in fewer than 3D without requiring precise control over the crystal structure or orientation.

With the aim of making this study more practically relevant, the following future directions are proposed:

- Through *in situ* experiments, it is shown that certain grain boundaries evolve into defects after micromachining due to ductile tearing in the vicinity of transition between two neighboring grains. However, not all grain boundaries will result in topographical defects. The polycrystalline nature of bulk material urges the development of a statistical model which can evaluate the probability distribution of defects nucleation. This development needs acquiring large data sets from systematic characterization of defect nucleation at surfaces created via micro-scale material removal as a function of bulk microstructure characteristics. Furthermore, the experimental observations could be nested with machine learning, which will give a probabilistic evaluation of material performance in manufacturing for given microstructural attributes and deformation conditions. It is envisioned that insights gained form this research direction would provide direct guidance on microstructure engineering for machining which can potentially increase the production yield of mirror-like surface from diamond-turning process.
- The machining configuration offers a simple way to impose severe plastic deformation on the bulk material, of which characteristic length-scale of deformation can be tuned through a change of only one parameter (preset depth of cut a_0). Furthermore, this parameter could be potentially reduced down below 100nm-scale. Thus, it would be possible if designing new platform to perform severe plastic deformation inside transmission electron microscopy for *in situ* observations, where the microstructural consequences including dislocation dynamics, formation and evolution of dislocation substructures and interaction with presence of interfaces (e.g., grain boundaries, second phase particles) could be delineated.
- Despite of wide application of diamond turning to create components with ultra-high precision, our trials with zirconium, titanium, and niobium (d-shell rich transition metals) actually revealed the formation of an intimately bonded “built up edge” on the single-crystal diamond tool surface (in contact with deformed chip) and rapid degradation of the cutting edge even at really low machining speed ($V = 150\mu$m) which results from chemo-mechanical diffusion interaction. One potential research direction could focus on investigation of diffusional mass transport across interfaces, which would provide: a) a framework for controlling/mitigating tool wear in technologically-critical diamond

turning process by identifying the aspects that suppress diffusion and b) offer a new platform technology for magnifying the C transport on-demand with spatial selectivity to achieve controlled micro/nanostructuring of diamond surfaces using the d-shell rich transition metals as solid-state etchants.

Bibliography

[1] S Abolghasem, Saurabh Basu, S Shekhar, J Cai, and MR Shankar. Mapping subgrain sizes resulting from severe simple shear deformation. *Acta Materialia*, 60(1):376–386, 2012.

[2] Sepideh Abolghasem, Saurabh Basu, and M Ravi Shankar. Quantifying the progression of dynamic recrystallization in severe shear deformation at high strain rates. *Journal of Materials Research*, 28(15):2056–2069, 2013.

[3] Amir H Adibi-Sedeh, Vis Madhavan, and Behnam Bahr. Extension of oxley's analysis of machining to use different material models. *Journal of manufacturing science and engineering*, 125(4):656–666, 2003.

[4] Zachary H Aitken, Haidong Fan, Jaafar A El-Awady, and Julia R Greer. The effect of size, orientation and alloying on the deformation of az31 nanopillars. *Journal of the Mechanics and Physics of Solids*, 76:208–223, 2015.

[5] T Al-Samman and G Gottstein. Room temperature formability of a magnesium az31 alloy: Examining the role of texture on the deformation mechanisms. *Materials Science and Engineering: A*, 488(1-2):406–414, 2008.

[6] A Arsenlis and DM Parks. Crystallographic aspects of geometrically-necessary and statistically-stored dislocation density. *Acta materialia*, 47(5):1597–1611, 1999.

[7] MF Ashby. The deformation of plastically non-homogeneous materials. *The Philosophical Magazine: A Journal of Theoretical Experimental and Applied Physics*, 21(170):399–424, 1970.

[8] Saurabh Basu, Sepideh Abolghasem, and M Ravi Shankar. Mechanics of intermittent plasticity punctuated by fracture during shear deformation of mg alloys at near-ambient temperatures. *Metallurgical and Materials Transactions A*, 44(10):4558–4566, 2013.

[9] Saurabh Basu and M Ravi Shankar. Microstructure evolution during severe shear deformation at small length-scales. *Scripta Materialia*, 72:51–54, 2014.

[10] Saurabh Basu and M Ravi Shankar. Spatial confinement-induced switchover in microstructure evolution during severe plastic deformation at micrometer length scales. *Acta Materialia*, 79:146–158, 2014.

[11] Bruce Alexander Bilby and AG Crocker. The theory of the crystallography of deformation twinning. *Proceedings of the Royal Society of London. Series A. Mathematical and Physical Sciences*, 288(1413):240–255, 1965.

[12] Abhijit Brahme, Joseph Fridy, Hasso Weiland, and Anthony D Rollett. Modeling texture evolution during recrystallization in aluminum. *Modelling and Simulation in Materials Science and Engineering*, 17(1):015005, 2008.

[13] Cynthia M Byer, Bin Li, Buyang Cao, and KT Ramesh. Microcompression of single-crystal magnesium. *Scripta Materialia*, 62(8):536–539, 2010.

[14] CM Cepeda-Jiménez, JM Molina-Aldareguia, and MT Pérez-Prado. Effect of grain size on slip activity in pure magnesium polycrystals. *Acta Materialia*, 84:443–456, 2015.

[15] Lian-Yi Chen, Jia-Quan Xu, Hongseok Choi, Marta Pozuelo, Xiaolong Ma, Sanjit Bhowmick, Jenn-Ming Yang, Suveen Mathaudhu, and Xiao-Chun Li. Processing and properties of magnesium containing a dense uniform dispersion of nanoparticles. *Nature*, 528(7583):539, 2015.

[16] John Wyrill Christian and Subhash Mahajan. Deformation twinning. *Progress in materials science*, 39(1-2):1–157, 1995.

[17] Thomas H Courtney. *Mechanical behavior of materials*. Waveland Press, 2005.

[18] Ferenc F Csikor, Christian Motz, Daniel Weygand, Michael Zaiser, and Stefano Zapperi. Dislocation avalanches, strain bursts, and the problem of plastic forming at the micrometer scale. *Science*, 318(5848):251–254, 2007.

[19] AM Cuitino and M Ortiz. Ductile fracture by vacancy condensation in fcc single crystals. *Acta materialia*, 44(2):427–436, 1996.

[20] Calvin Robert Cupp and B Chalmers. A study of the plastic deformation of copper single crystals. *Acta Metallurgica*, 2(6):803–809, 1954.

[21] Neha Dixit, Kelvin Y Xie, Kevin J Hemker, and KT Ramesh. Microstructural evolution of pure magnesium under high strain rate loading. *Acta materialia*, 87:56–67, 2015.

[22] RD Doherty, DA Hughes, FJ Humphreys, J Juul Jonas, D Juul Jensen, ME Kassner, WE King, TR McNelley, HJ McQueen, and AD Rollett. Current issues in recrystallization: a review. *Materials Science and Engineering: A*, 238(2):219–274, 1997.

[23] Roberto B Figueiredo, Shima Sabbaghianrad, Adenike Giwa, Julia R Greer, and Terence G Langdon. Evidence for exceptional low temperature ductility in polycrystalline magnesium processed by severe plastic deformation. *Acta Materialia*, 122:322–331, 2017.

[24] NA Fleck, GM Muller, MF Ashby, and JW Hutchinson. Strain gradient plasticity: theory and experiment. *Acta Metallurgica et materialia*, 42(2):475–487, 1994.

[25] FC Frank and WT Read Jr. Multiplication processes for slow moving dislocations. *Physical Review*, 79(4):722, 1950.

[26] Huajian Gao and Yonggang Huang. Geometrically necessary dislocation and size-dependent plasticity. *Scripta Materialia*, 48(2):113–118, 2003.

[27] Julia R Greer and Jeff Th M De Hosson. Plasticity in small-sized metallic systems: Intrinsic versus extrinsic size effect. *Progress in Materials Science*, 56(6):654–724, 2011.

[28] Morton E Gurtin. On the plasticity of single crystals: free energy, microforces, plastic-strain gradients. *Journal of the Mechanics and Physics of Solids*, 48(5):989–1036, 2000.

[29] B Ham and X Zhang. High strength mg/nb nanolayer composites. *Materials Science and Engineering: A*, 528(4-5):2028–2033, 2011.

[30] Niels Hansen. Hall–petch relation and boundary strengthening. *Scripta Materialia*, 51(8):801–806, 2004.

[31] PB Hirsch and JS Lally. The deformation of magnesium single crystals. *Philosophical Magazine*, 12(117):595–648, 1965.

[32] Do A Hughes and N Hansen. Microstructure and strength of nickel at large strains. *Acta Materialia*, 48(11):2985–3004, 2000.

[33] PJ Hurley and FJ Humphreys. The application of ebsd to the study of substructural development in a cold rolled single-phase aluminium alloy. *Acta Materialia*, 51(4):1087–1102, 2003.

[34] WB Hutchinson and MR Barnett. Effective values of critical resolved shear stress for slip in polycrystalline magnesium and other hcp metals. *Scripta Materialia*, 63(7):737–740, 2010.

[35] John J Jonas, Sijia Mu, Talal Al-Samman, Günter Gottstein, Lan Jiang, and Ėtienne Martin. The role of strain accommodation during the variant selection of primary twins in magnesium. *Acta Materialia*, 59(5):2046–2056, 2011.

[36] William J Joost and Paul E Krajewski. Towards magnesium alloys for high-volume automotive applications. *Scripta Materialia*, 128:107–112, 2017.

[37] Marina Viktorovna Klassen-Neklyudova. *Mechanical twinning of crystals*. Springer Science & Business Media, 2012.

[38] UF Kocks and H Mecking. Physics and phenomenology of strain hardening: the fcc case. *Progress in materials science*, 48(3):171–273, 2003.

[39] J Koike, T Kobayashi, T Mukai, H Watanabe, M Suzuki, K Maruyama, and K Higashi. The activity of non-basal slip systems and dynamic recovery at room temperature in fine-grained az31b magnesium alloys. *Acta materialia*, 51(7):2055–2065, 2003.

[40] L Kubin, B Devincre, and T Hoc. Modeling dislocation storage rates and mean free paths in face-centered cubic crystals. *Acta materialia*, 56(20):6040–6049, 2008.

[41] L Kubin, T Hoc, and B Devincre. Dynamic recovery and its orientation dependence in face-centered cubic crystals. *Acta Materialia*, 57(8):2567–2575, 2009.

[42] NV Ravi Kumar, JJ Blandin, C Desrayaud, F Montheillet, and M Suéry. Grain refinement in az91 magnesium alloy during thermomechanical processing. *Materials Science and Engineering: A*, 359(1-2):150–157, 2003.

[43] R Le Gall and JJ Jonas. Solute drag effects during the dynamic recrystallization of nickel. *Acta materialia*, 47(17):4365–4374, 1999.

[44] Seongeyl Lee, Jihong Hwang, M Ravi Shankar, Srinivasan Chandrasekar, and W Dale Compton. Large strain deformation field in machining. *Metallurgical and Materials Transactions A*, 37(5):1633–1643, 2006.

[45] TE Mitchell. Dislocations and plasticity in single crystals of face-centred cubic metals and alloys. *Progress in Applied Materials Research*, 6:117–237, 1964.

[46] Konstantin D Molodov, Talal Al-Samman, Dmitri A Molodov, and Günter Gottstein. Mechanisms of exceptional ductility of magnesium single crystal during deformation at room temperature: Multiple twinning and dynamic recrystallization. *Acta Materialia*, 76:314–330, 2014.

[47] F R N Nabarro. Dislocations in a simple cubic lattice. *Proceedings of the Physical Society*, 59(2):256, 1947.

[48] Erik Nes. Modelling of work hardening and stress saturation in fcc metals. *Progress in Materials Science*, 41(3):129–193, 1997.

[49] Philip Noell, Jay Carroll, Khalid Hattar, Blythe Clark, and Brad Boyce. Do voids nucleate at grain boundaries during ductile rupture? *Acta Materialia*, 137:103–114, 2017.

[50] PLB Oxley and WF Hastings. Predicting the strain rate in the zone of intense shear in which the chip is formed in machining from the dynamic flow stress properties of the work material and the cutting conditions. *Proceedings of the Royal Society of London. A. Mathematical and Physical Sciences*, 356(1686):395–410, 1977.

[51] Wolfgang Pantleon. Formation of disorientations in dislocation structures during plastic deformation. In *Solid State Phenomena*, volume 87, pages 73–92. Trans Tech Publ, 2002.

[52] Triplicane A Parthasarathy, Satish I Rao, Dennis M Dimiduk, Michael D Uchic, and Dallas R Trinkle. Contribution to size effect of yield strength from the stochastics of dislocation source lengths in finite samples. *Scripta Materialia*, 56(4):313–316, 2007.

[53] PG Partridge. The crystallography and deformation modes of hexagonal close-packed metals. *Metallurgical reviews*, 12(1):169–194, 1967.

[54] R Peierls. The size of a dislocation. *Proceedings of the Physical Society*, 52(1):34, 1940.

[55] A Petri, G Paparo, A Vespignani, A Alippi, and M Costantini. Experimental evidence for critical dynamics in microfracturing processes. *Physical review letters*, 73(25):3423–3426, 1994.

[56] Tresa M Pollock. Weight loss with magnesium alloys. *Science*, 328(5981):986–987, 2010.

[57] RC Pond, WAT Clark, and RH Wagoner. On the crystallography of slip transmision in hexagonal metals. *Scripta metallurgica*, 20(9):1291–1295, 1986.

[58] Robert E Reed-Hill, Reza Abbaschian, and Reza Abbaschian. *Physical metallurgy principles*. Van Nostrand New York, 1973.

[59] Anthony Rollett, Gregory S Rohrer, and John Humphreys. *Recrystallization and Related Annealing Phenomena*. Newnes, 2017.

[60] G Saada. Sur la nature des défauts ponctuels crées par le croisement des dislocations. *Acta Metallurgica*, 9(10):965–966, 1961.

[61] Taku Sakai, Andrey Belyakov, Rustam Kaibyshev, Hiromi Miura, and John J Jonas. Dynamic and post-dynamic recrystallization under hot, cold and severe plastic deformation conditions. *Progress in materials science*, 60:130–207, 2014.

[62] S Sandlöbes, S Zaefferer, I Schestakow, S Yi, and R Gonzalez-Martinez. On the role of non-basal deformation mechanisms for the ductility of mg and mg–y alloys. *Acta Materialia*, 59(2):429–439, 2011.

[63] Stefanie Sandlöbes, Igor Schestakow, Sang Bong Yi, Stefan Zaefferer, Jing Qui Chen, Martin Friák, Jörg Neugebauer, and Dierk Raabe. The relation between shear banding, microstructure and mechanical properties in mg and mg-y alloys. In *Materials Science Forum*, volume 690, pages 202–205. Trans Tech Publ, 2011.

[64] Zhiwei Shan, EA Stach, JMK Wiezorek, JA Knapp, DM Follstaedt, and SX Mao. Grain boundary-mediated plasticity in nanocrystalline nickel. *Science*, 305(5684):654–657, 2004.

[65] Milton Clayton Shaw and JO Cookson. *Metal cutting principles*. Oxford university press New York, 2005.

[66] S Shekhar, S Abolghasem, Saurabh Basu, J Cai, and MR Shankar. Effect of severe plastic deformation in machining elucidated via rate-strain-microstructure mappings. *Journal of Manufacturing Science and Engineering*, 134(3), 2012.

[67] S Spigarelli, Oscar Antonio Ruano, M El Mehtedi, and JA Del Valle. High temperature deformation and microstructural instability in az31 magnesium alloy. *Materials Science and Engineering: A*, 570:135–148, 2013.

[68] N Stanford and MR Barnett. Effect of particles on the formation of deformation twins in a magnesium-based alloy. *Materials Science and Engineering: A*, 516(1-2):226–234, 2009.

[69] Byeong-Chan Suh, Myeong-Shik Shim, KS Shin, and Nack J Kim. Current issues in magnesium sheet alloys: where do we go from here? *Scripta Materialia*, 84:1–6, 2014.

[70] DY Sun, MI Mendelev, CA Becker, K Kudin, Tomorr Haxhimali, M Asta, JJ Hoyt, A Karma, and DJ Srolovitz. Crystal-melt interfacial free energies in hcp metals: A molecular dynamics study of mg. *Physical Review B*, 73(2):024116, 2006.

[71] A.P. Sutton and R.W. Balluffi. *Interfaces in crystalline materials*. Monographs on the physics and chemistry of materials. Clarendon Press, 1995.

[72] Geoffrey Ingram Taylor. Plastic strain in metals. *J. Inst. Metals*, 62:307–324, 1938.

[73] Michael D Uchic, Dennis M Dimiduk, Jeffrey N Florando, and William D Nix. Sample dimensions influence strength and crystal plasticity. *Science*, 305(5686):986–989, 2004.

[74] YB Wang, BQ Li, ML Sui, and SX Mao. Deformation-induced grain rotation and growth in nanocrystalline ni. *Applied Physics Letters*, 92(1):011903, 2008.

[75] Yi Wang, L-Q Chen, Z-K Liu, and SN Mathaudhu. First-principles calculations of twin-boundary and stacking-fault energies in magnesium. *Scripta Materialia*, 62(9):646–649, 2010.

[76] Grethe Winther and Xiaoxu Huang. Dislocation structures. part ii. slip system dependence. *Philosophical Magazine*, 87(33):5215–5235, 2007.

[77] D Wu, RS Chen, and EH Han. Excellent room-temperature ductility and formability of rolled mg–gd–zn alloy sheets. *Journal of Alloys and Compounds*, 509(6):2856–2863, 2011.

[78] Ho Yeung, Koushik Viswanathan, Walter Dale Compton, and Srinivasan Chandrasekar. Sinuous flow in metals. *Proceedings of the National Academy of Sciences*, 112(32):9828–9832, 2015.

[79] MH Yoo. Slip, twinning, and fracture in hexagonal close-packed metals. *Metallurgical Transactions A*, 12(3):409–418, 1981.

[80] MH Yoo and CT Wei. Slip modes of hexagonal-close-packed metals. *Journal of Applied Physics*, 38(11):4317–4322, 1967.

[81] Qian Yu, Liang Qi, Kai Chen, Raja K Mishra, Ju Li, and Andrew M Minor. The nanostructured origin of deformation twinning. *Nano letters*, 12(2):887–892, 2012.

[82] Qian Yu, Zhi-Wei Shan, Ju Li, Xiaoxu Huang, Lin Xiao, Jun Sun, and Evan Ma. Strong crystal size effect on deformation twinning. *Nature*, 463(7279):335, 2010.

[83] Zhuoran Zeng, Jian-Feng Nie, Shi-Wei Xu, Chris HJ Davies, and Nick Birbilis. Super-formable pure magnesium at room temperature. *Nature communications*, 8(1):972, 2017.

[84] BP Zhang, L Geng, LJ Huang, XX Zhang, and CC Dong. Enhanced mechanical properties in fine-grained mg–1.0 zn–0.5 ca alloys prepared by extrusion at different temperatures. *Scripta Materialia*, 63(10):1024–1027, 2010.